UNIVERSIDAD COMPLUTENSE DE MADRID
FACULTAD DE CIENCIAS FÍSICAS

TESIS DOCTORAL

Tropical ocean-atmosphere interactions in coupled models. The case of of the Equatorial thermocline and the northwest African upwelling
Interacciones tropicales océano-atmósfera en modelos acolpados. El caso de la termoclina ecuatorial y el afloramiento del noroeste de África

MEMORIA PARA OPTAR AL GRADO DE DOCTOR

PRESENTADA POR

Antonio Castaño Tierno

Directores

Elsa Mohino Harris
Teresa Losada Doval
Belén Rodríguez de Fonseca

Madrid

UNIVERSIDAD COMPLUTENSE DE MADRID

FACULTAD DE CIENCIAS FÍSICAS

DEPARTAMENTO DE FÍSICA DE LA TIERRA Y ASTROFÍSICA

TROPICAL OCEAN-ATMOSPHERE INTERACTIONS IN COUPLED MODELS. THE CASE OF THE EQUATORIAL THERMOCLINE AND THE NORTHWEST AFRICAN UPWELLING

INTERACCIONES TROPICALES OCÉANO-ATMÓSFERA EN MODELOS ACOPLADOS. EL CASO DE LA TERMOCLINA ECUATORIAL Y EL AFLORAMIENTO DEL NOROESTE DE ÁFRICA

Dirigida por:

Dra. Elsa Mohino Harris

Dra. Teresa Losada Doval

Dra. Belén Rodríguez de Fonseca

Memoria presentada por:

Antonio Castaño Tierno

Para optar al grado de Doctor en Física

2019

UNIVERSIDAD COMPLUTENSE MADRID

DECLARACIÓN DE AUTORÍA Y ORIGINALIDAD DE LA TESIS PRESENTADA PARA OBTENER EL TÍTULO DE DOCTOR

D./Dña. Antonio Castaño Tierno,
estudiante en el Programa de Doctorado en Físicas,
de la Facultad de Ciencias Físicas de la Universidad Complutense de Madrid, como autor/a de la tesis presentada para la obtención del título de Doctor y titulada:

Interacciones tropicales océano-atmósfera en modelos acoplados.
El caso de la termoclina ecuatorial y el afloramiento del noroeste de África.

y dirigida por: Elsa Mohino Harris, Teresa Losada Doval y Belén Rodríguez de Fonseca.

DECLARO QUE:

La tesis es una obra original que no infringe los derechos de propiedad intelectual ni los derechos de propiedad industrial u otros, de acuerdo con el ordenamiento jurídico vigente, en particular, la Ley de Propiedad Intelectual (R.D. legislativo 1/1996, de 12 de abril, por el que se aprueba el texto refundido de la Ley de Propiedad Intelectual, modificado por la Ley 2/2019, de 1 de marzo, regularizando, aclarando y armonizando las disposiciones legales vigentes sobre la materia), en particular, las disposiciones referidas al derecho de cita.

Del mismo modo, asumo frente a la Universidad cualquier responsabilidad que pudiera derivarse de la autoría o falta de originalidad del contenido de la tesis presentada de conformidad con el ordenamiento jurídico vigente.

En Madrid, a 28 de junio de 2019

Fdo.: Antonio Castaño Tierno

Esta DECLARACIÓN DE AUTORÍA Y ORIGINALIDAD debe ser insertada en la primera página de la tesis presentada para la obtención del título de Doctor.

Desde el nacimiento hasta la muerte las
personas dependemos materialmente del
tiempo que otras personas nos dedican.
Yayo Herrero

Science was many things, Nadia thought, including
a weapon with which to hit other scientists.
Kim Stanley Robinson, Red Mars

Agradecimientos

Los tópicos lo son por algo: sin Elsa, Teresa y Belén esta tesis no existiría. William Morris distinguía entre trabajo útil y esfuerzo inútil; sin vuestra ayuda y guía estos cuatro años habrían sido mucho de lo segundo y bien poco de lo primero. Si me llevo algún remordimiento de esta etapa es el no haber sabido aprovechar más la oportunidad de tener juntas a estas tres directoras. Muchísimas gracias por todo vuestro tiempo, saber y paciencia.

Tampoco habría seguido el camino de la tesis si Roberto Mechoso no me hubiera dado la oportunidad de pasar tres meses con él en Los Ángeles. Yo no lo olvidaré, y las amistades a las que he puesto (y pondré) la cabeza loca con las mismas cuatro historias californianas, tampoco.

Este casi lustro es inseparable de la gente que me ha acogido, primero, y luego acompañado en el Elvira Zurita y alrededores. Gracias a Julián y Rober, y también a Irene, Jorge y Marta. Gracias a Ade y Jesús, a Víctor y Verónica. ¡Gracias a Adama! Y a Moussa. Gracias a Luis, Javi y Ana, y a Jon, Cahlo y Mariano. Gracias a Jose, Antonio y Alberto, compañeros en la perenne duda burocrática

¡Gracias a Froila, fundamental (no solo) para los cafés! Y eterno agradecimiento a Carlos, presencia tranquilizadora y financiador de tortillas.

Gracias a mis compañeros de Contra el diluvio, que hacen más difícil creer en el desastre. A Clara, con la que se puede contar cualquier cosa, y a Fran, Alberto, Merche. Reservad todas las tardes de aquí a mayo. David y Leti: nos vemos el próximo fin de semana.

Acabo: gracias a mis padres y mi hermano, a los que debo más de un paseo; y a Ana, que vio el principio y ha visto el final. Te debo postales. A Clara: que estés en una isla ya no es excusa, con lo que me gustan a mí los barcos.

Maddalen, tenemos unos pocos de desayunos pendientes, eta asko ibili hondartzan.

Table of contents

Abstract

INTRODUCTION:

The tropics show great climate variability at different timescales. Part of this variability is related to the processes that couple the ocean and the atmosphere. Surface winds drive ocean currents, while the combination of wind stress and solar heating leads to the development of the mixed layer, the topmost layer of the ocean, which is the most affected by the ocean-atmosphere coupling. This layer rests on the thermocline, an oceanic region in which the vertical temperature gradient is maximum, forming a physical barrier between the colder water of the deep ocean and the mixed layer. Understanding the dynamics of that layer and in particular its relation to wind forcings is fundamental for studying coupled atmosphere-ocean phenomena.

Historically, locating the thermocline in the ocean has been a difficult task, due to the lack of specialized equipment (Sverdrup, 1942). This led to the use of representative isotherms as a measure of the thermocline (Fiedler, 2010). The chosen isotherm depends on the latitude and the ocean studied in each case (Kessler, 1990; Yang and Wang, 2009). In the equatorial Pacific Ocean the isotherm usually selected to represent the thermocline is 20°C (Lengaigne et al., 2012; Li and Xie, 2014; Xiang et al., 2017; Lübbecke and McPhaden, 2017; Martín-Rey et al., 2014). For the tropical Atlantic, the depth of the 22°C isotherm (Deppenmeier et al., 2016) or 23°C isotherm (Cabos et al., 2017) has been used as representative of the thermocline. With the development and general adoption of General Circulation Models (GCMs), the depth of a representative isotherm (generally the 20°C one, hereafter, z20) as an estimate of the thermocline depth was kept to compare model and observations, given the relatively poor vertical resolution of ocean models. The adequacy of this choice has rarely been put into question for present climate, although there have been attempts to evaluate the validity of z20 in future climate (Yang and Wang, 2009).

The tropical band is also where the four main upwelling regions of the world are located. These areas are among the most abundant in marine life in the whole world due to the nutrient-richer water driven to the surface by coastal upwelling (Sydeman et al. 2014; Bakun, 1990). The North West Africa upwelling region, located on the West African shore between 10°N and 25°N (Bakun, 1990; Wang et al., 2015), is studied in Chapters 4 and 5 of this thesis. The importance of correctly assessing model representation of wind-driven upwelling is highlighted by the high uncertainty about how these regions will behave in a climate change scenario (Wang et al., 2014; Sylla et al., 2019).
However, coupled general circulation models, which are very useful tools for the study of climate, are known to have biases such as a too warm Southern Ocean and South Eastern Atlantic (Wang et al., 2014) and a double Pacific ITCZ which leads to excessive precipitation south of the Equator (Li and Xie, 2014). These biases pose some limits to the usefulness of GCMs as research tools and condition the simulation of delicate features such as coastal upwelling. Knowing and understanding these biases is fundamental for their correction and the improvement of models performance.

OBJECTIVES:

The main objective of this thesis is to improve the understanding of the way the tropical ocean dynamically reacts to wind forcing. It is focused is on the equatorial and coastal upwelling regions. For the former, the Pacific and Atlantic thermocline is studied; for the latter, the North West African (NWA) upwelling is analysed. The goals of the thesis are:

1) to study whether the use of a particular isotherm as an estimate of the thermocline is a good option in the Tropics in models.

2) to explore the representation of NWA upwelling in reanalysis and models, and study how large-scale model biases affect its representation.

3) to assess the role that ocean vertical thermal stratification plays in the correct representation of upwelling dynamics.

DATA AND METHODOLOGY:

Two different set of coupled model outputs have been used along this thesis. On the one hand, the pre-industrial control simulations of 24 atmosphere-ocean coupled models participating in the Coupled Model Intercomparison Project, phase 5 (CMIP5). On the other hand, the UCLA general circulation model has been used, both for a control run and for conducting an idealized sensitivity experiment. From reanalysis, potential temperature from SODA (Carton et al., 2005) has been used. Sea surface temperature from ERSSTv3b (Smith et al., 2008), sea level pressure from HadSLP2r (Basnett and Parker, 1997; Allan and Ansel, 2006), wind stress from WASWind, (Tokinaga and Xie, 2011) and daily precipitation from GPCP (Adler et al., 2003) have been used as observational reconstructions. 30 years have been chosen for all variables (1979-2008 period).

Regarding the treatment of data, in Chapter 2 two different algorithms are used to locate the physical thermocline and z20.

Discriminant analysis techniques as EOFs, together with correlation analysis have been the main statistical tools used to analyse the data. Also, the significance of the results has been analysed using Student t-test.

RESULTS AND CONCLUSIONS:

The results in this thesis are divided in three chapters:

1) In Chapter 3 the implications of the use of two different estimates for the physical thermocline, both in the tropical Pacific and Atlantic Oceans, is assessed. The main results from this chapter are:
    a. The commonly used 20°C isotherm (z20) is systematically deeper than the physical thermocline both in SODA reanalysis and in CMIP5 models.
    b. z20 shows a less marked seasonal cycle than the thermocline, both in the Pacific and in the Atlantic Oceans.
    c. For the Eastern Pacific, z20 is strongly related to SSTs (not true for the physical thermocline) while for the Western

Pacific and the Atlantic it does not react to zonal Equatorial winds as much as the physical thermocline.

d. Overall, z20 is more related to surface sea temperature forcings and less to dynamical forcings than the physical thermocline. The role of extratropical winds (and therefore of Sverdrup transport) is also different for z20 than for the thermocline depth.

2) Chapter 4 focuses on the representation of the NWA upwelling in reanalysis and CMIP5 models. The main results are:

   a. CMIP5 models capture the general seasonal cycle of wind-dependent NWA upwelling, but exaggerate its intensity due to excessive meridional winds.

   b. This excessive upwelling does not translate into cooler surface temperatures. It is posited that the too strong thermal stratification in CMIP5 models is responsible for this because it inhibits cold waters from the bottom to reach the surface. Most of the main wind-related coastal upwelling intermodel variability is explained by two modes (68% of variability in total). the first one is dominated by latitudinal changes in the upwelling and it is associated to models with different land-sea pressure gradients, which seems to be related to changes in the radiation over land. The second mode is characterized by changes in the seasonal cycle. This mode separates models that present different land-sea pressure gradient, but dominated by intermodel variations in the ITCZ position and West African monsoon representation.

3) In Chapter 5 the UCLA general circulation model is used to explore the dependence of the wind-induced upwelling representation on remote model biases through the use of an idealized sensitivity experiment in which incoming solar radiation onto the Southern Ocean is reduced. The results are:

a. UCLA control run shows very strong warm biases and a southward-shifted ITCZ. The upwelling is overestimated, though the bias is smaller than that of CMIP5 models.
b. Unlike CMIP5 models, the UCLA model shows a correspondence between the seasonal cycles of upwelling and SSTs. Such correspondence is posited to being due to thermocline strength in the UCLA model being more similar to the observed one.
c. Diminished incoming radiation in the Southern Ocean leads to reduced SST bias and northward-shifted ITCZ, which contributes to a reinforcement of northerly winds in the north of the NWA region providing more upwelling. In turn monsoon winds increase in the south of the NWA region, leading to more precipitation.

Resumen

INTRODUCCIÓN:

Los trópicos muestran una gran variabilidad climática en diferentes escalas de tiempo. Parte de esta variabilidad está relacionada con los procesos de acomplamiento entre el océano y la atmósfera. Los vientos superficiales impulsan las corrientes oceánicas, mientras que la combinación de la cizalla del viento y el calentamiento solar conduce al desarrollo de la capa de mezcla, la más somera del océano, que es la más afectada por el acoplamiento océano-atmósfera. Esta capa descansa sobre la termoclina, una región en la que el gradiente vertical de temperatura es máximo, formando una barrera física entre el agua más fría del océano profundo y la capa de mezcla. Comprender la dinámica de esa capa y en particular su relación con los forzamientos del viento es fundamental para estudiar los fenómenos acoplados atmósfera-océano.

Históricamente, localizar la termoclina en el océano ha sido una tarea difícil, debido a la falta de equipo especializado (Sverdrup, 1942). Esto condujo al uso de isotermas representativas como medida de la termoclina (Fiedler, 2010). La isoterma elegida depende de la latitud y del océano estudiado en cada caso (Kessler, 1990; Yang y Wang, 2009). En el Océano Pacífico ecuatorial, la isoterma seleccionada habitualmente para representar la termoclina es de 20°C (Lengaigne et al., 2012; Li y Xie, 2014; Xiang et al., 2017; Lübbecke y McPhaden, 2017; Martín-Rey et al., 2014). Para el Atlántico tropical, la profundidad de la isoterma de 22°C (Deppenmeier et al., 2016) o la isoterma de 23°C (Cabos et al., 2017) se ha utilizado como representativa de la termoclina. Con el desarrollo y la adopción general de los Modelos Acomplados de Circulación General (CGCMs por sus siglas en inglés), se mantuvo la profundidad de una isoterma representativa (generalmente la de 20°C, en adelante, z20) como estimación de la profundidad de la termoclina para poder comparar el modelo y las observaciones, dada la relativamente pobre resolución vertical de los modelos oceánicos. La idoneidad de esta

elección rara vez se ha puesto en duda para el clima actual, aunque ha habido intentos de evaluar la validez de z20 en el clima futuro (Yang y Wang, 2009).

La banda tropical es también donde se encuentran las cuatro principales regiones de afloramiento del mundo. Estas áreas se encuentran entre las más abundantes en vida marina del planeta, debido al agua rica en nutrientes impulsada a la superficie por los afloramientos costeros (Sydeman et al. 2014; Bakun, 1990). En los capítulos 4 y 5 de esta tesis se estudia la región de afloramiento del noroeste de África, situada en la costa de África occidental entre 10°N y 25°N (Bakun, 1990, Wang et al., 2015). La importancia de evaluar correctamente la representación del modelo de afloramiento impulsado por el viento se pone de relieve por la gran incertidumbre sobre cómo se comportarán estas regiones en un escenario de cambio climático (Wang et al., 2014; Sylla et al., 2019).

Sin embargo, se sabe que los modelos de circulación general acoplados, que son herramientas muy útiles para el estudio del clima, tienen sesgos tales como un Océano Austral y un Atlántico Sudeste demasiado cálidos (Wang et al., 2014) y una doble ITCZ en el Pacífico, que conduce a precipitaciones excesivas al sur del Ecuador (Li y Xie, 2014). Estos sesgos plantean algunos límites a la utilidad de los CGCMs como herramientas de investigación y condicionan la simulación de características delicadas como el afloramiento costero. Conocer y comprender estos sesgos es fundamental para su corrección y para la mejora del rendimiento de los modelos.

OBJETIVOS:

El objetivo principal de esta tesis es mejorar la comprensión de la forma en que la dinámica del océano tropical reacciona al viento. Nos centraremos en las regiones de afloramiento ecuatorial y costero. Para el primero se estudia la termoclina del Pacífico y del Atlántico; para el segundo, se analiza el afloramiento del Noroeste de África (NWA). Los objetivos de la tesis son:

1) estudiar si el uso de una determinada isoterma como estimación de la termoclina es una buena opción en los trópicos en los modelos.
2) explorar la representación del afloramiento de NWA en reanálisis y

modelos, y estudiar cómo los sesgos de los modelos a gran escala afectan a su representación.

3) evaluar el papel que juega la estratificación térmica vertical del océano en la correcta representación de la dinámica de afloramiento.

DATOS Y MÉTODOS:

A lo largo de esta tesis se han utilizado dos conjuntos diferentes de simulaciones de modelos acoplados. Por un lado, las simulaciones de control preindustrial de 24 modelos acoplados atmósfera-océano que participan en el Proyecto de Intercomparación de Modelos Acoplados, fase 5 (CMIP5). Por otro lado, se ha utilizado el modelo de circulación general de UCLA, tanto para una simulación de control como para llevar a cabo un experimento idealizado de sensibilidad. Como datos de reanálisis, se ha utilizado la temperatura potencial de SODA (Carton et al., 2005), y como observaciones la temperatura superficial del mar de ERSSTv3b (Smith et al., 2008), la presión sobre el nivel del mar de HadSLP2r (Basnett y Parker, 1997; Allan y Ansel, 2006), el estrés del viento de WASWind (Tokinaga y Xie, 2011) y la precipitación diaria de GPCP (Adler et al., 2003). Se han elegido 30 años para todas las variables (período 1979-2008).

En cuanto al tratamiento de datos, en el capítulo 2 se utilizan dos algoritmos diferentes para localizar la termoclina física y z20.

Las principales herramientas estadísticas utilizadas para analizar los datos han sido técnicas de análisis discriminante como las EOFs, junto con análisis de correlación intra e intermodelos. Además, se ha analizado la significatividad de los resultados mediante la prueba t-test de Student.

RESULTADOS Y CONCLUSIONES:

Los resultados de esta tesis se dividen en tres capítulos::

1) En el Capítulo 3 se evalúan las implicaciones del uso de dos estimaciones diferentes para la termoclina física, tanto en el Pacífico

tropical como en el Atlántico. Los principales resultados de este capítulo son:

a. La comúnmente utilizada isoterma de 20°C (z20) es sistemáticamente más profunda que la termoclina física, tanto en el reanálisis de SODA como en los modelos CMIP5
b. z20 muestra un ciclo estacional menos marcado que la termoclina, tanto en el Pacífico como en el Atlántico.
c. Para el Pacífico Oriental, z20 depende en gran medida de la temperatura de la superficie del mar (lo que no es cierto para la termoclina física), mientras que para el Pacífico Occidental y el Atlántico no reacciona a los vientos ecuatoriales zonales tanto como la termoclina física.
d. En general, z20 está más relacionado con los forzamientos de la temperatura superficial del mar y menos con los forzamientos dinámicos que la termoclina física. El papel de los vientos extratropicales (y por lo tanto del transporte Sverdrup) también es diferente para z20 que para la termoclina.

2) El capítulo 4 se centra en la representación del afloramiento de NWA en los modelos de reanálisis y CMIP5. Los principales resultados son:
   a. Los modelos CMIP5 capturan el ciclo estacional general del afloramiento dirigido por el viento en NWA, pero exageran su intensidad debido a los vientos meridionales excesivos.
   b. Este exceso de afloramiento no se traduce en temperaturas superficiales más frías. Se postula que la estratificación térmica demasiado fuerte en los modelos CMIP5 es responsable de esto porque inhibe las aguas frías desde el fondo para alcanzar la superficie. La mayor parte de la variabilidad de los principales modelos intermodales de afloramiento costero relacionados con el viento se explica por dos modos (68% de la variabilidad total). El primero está dominado por los cambios latitudinales en el afloramiento y se asocia a modelos con diferentes gradientes de presión tierra-mar, lo que parece estar relacionado con los cambios en

la radiación sobre la tierra. El segundo modo se caracteriza por cambios en el ciclo estacional. Este modo separa modelos que presentan diferentes gradientes de presión tierra-mar, pero dominados por variaciones intermodales en la posición de la ITCZ y la representación de los monzones de África.

3) En el Capítulo 5 se utiliza el modelo de circulación general de UCLA para explorar la dependencia de la representación del afloramiento inducido por el viento de los sesgos de modelos remotos mediante el uso de un experimento de sensibilidad idealizada en el que se reduce la radiación solar entrante en el Océano Austral. Los resultados son::
    a. La simulación de control de UCLA muestra sesgos cálidos muy fuertes y una ITCZ desplazada hacia el sur. El afloramiento está sobreestimado, aunque el sesgo es menor que el de los modelos CMIP5.
    b. El afloramiento está sobreestimada, aunque el sesgo es menor que el de los modelos CMIP5.A diferencia de los modelos CMIP5, el modelo UCLA muestra una correspondencia entre los ciclos estacionales de afloramiento y SST. Dicha correspondencia se debe a que la fuerza de la termoclina en el modelo UCLA es más similar a la observada.
    c. La disminución de la radiación entrante en el Océano Austral conduce a una reducción del sesgo de la temperatura de la superficie del mar y a un desplazamiento hacia el norte de la ITCZ, lo que contribuye a reforzar los vientos del norte en el norte de la región del Océano Índico septentrional, proporcionando más afloramiento. A su vez, los vientos monzónicos aumentan en el sur de la región NWA, provocando más precipitaciones.

I Introduction and objectives

1 Introduction and objectives

1.1 General circulation of the atmosphere in the tropics and the role of oceans in climate

General circulation of the atmosphere can be explained, in a simple conceptual framework, by the different radiative budget between the Equator and the poles together with the planet rotation. The distribution of radiation is zonally uniform, but varies from the Equator (maximum) to the poles (minimum). The redistribution of the energy is achieved through atmospheric and ocean currents, although at different time and spatial scales (Vallis, 2012). The meridional circulation is conducted through six cells (three in each hemisphere, Fig. 1.1b). These are the polar cells (located from 60° to 90°), the Ferrel cells (30° to 60°) and the Hadley cells (0° to 30°).

The tropical region is under the influence of the Hadley cell, as a result of the atmosphere adjustment to equilibrate imposed imbalances (Hadley, 1735). The air flows towards higher latitudes and sinks over subtropical high-pressure areas (descending branch of the Hadley cell). As a consequence of the rotation of earth, at the surface, the flow moves from the subtropics towards the Equator along the trade winds belt. The effect of rotation causes the wind to be deflected perpendicularly to is direction. The air is deflected to the right in the Northern Hemisphere and to the left in the Southern Hemisphere (Holton, 2004). This is the reason why the trade winds, which flow from the extratropics towards the Equator become eastward-flowing when they reach the Equator. These winds transport moist and warm air, contributing to the presence of the Intertropical Convergence Zone (ITCZ, Fig. 1.1a). The ITCZ is a region located close to the geographic Equator, where the northeasterly and southeasterly wind from each hemisphere flow. This convergence and the warming in the tropics force air to ascend towards the upper troposphere, with moisture condensing into clouds. The rainbelt thus formed moves meridionally following the seasonal cycle (Fig. 1.1). Its mean position is around 6° north of the Equator (Schneider et al., 2014), and its latitudinal movement is determined by a combination of factors, including the interhemispheric temperature gradient (Hwang and Frierson, 2013; Kang

et al., 2008).

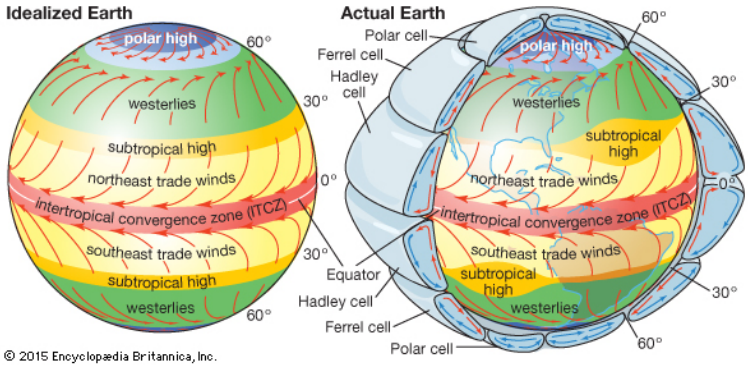

Figure 1.1: *Schematic representation of the main large scale structures that characterize the general circulation of the atmosphere. Source: britannica.com*

Regarding the ocean, the specific heat of the seawater is four times that of air, which, jointly with its enormous mass, makes oceans capable of storing much more heat for longer periods of time that the atmosphere (Vallis, 2012). This makes the ocean responsible for a moderating effect on climate which translates, for instance, on milder winters and cooler summers in coastal regions. Changes in oceans' temperature are gradually transferred to the atmosphere, therefore making them drivers of global atmospheric variability. The oceans have a role in the redistribution of the incoming solar energy through the global ocean circulation, which can be divided in two types, the Meridional Overturning Circulations (MOCS) and the wind-driven currents. Both of them transport heat from the equatorial region toward higher latitudes, making the latter warmer than they would be without the existence of oceans. Oceans also act as a carbon dioxide sink, slowing global warming, although this leads to the progressive acidification of ocean water (Orr et al., 2005).

1.1.1 Ocean stratification, thermocline and mixed layer

The ocean is vertically stratified, being characterized by a temperature profile that decreases with depth. The top layer of the ocean is called the mixed layer, and it is where most of the air-sea interaction processes take place. It is also the region of more fishing and economic importance and, more generally, the part of the ocean which has immediate influence on human lives (Gu and Philander, 1997). The mixed layer, as its name indicates, is well mixed so there are no strong thermal and salinity gradients on it. The lower boundary of the mixed layer is the thermocline (Fig. 1.2), the layer in which the vertical temperature gradient is maximum (Sverdrup, 1942; Breugem et al., 2008). In this thesis "thermocline" always refers to the seasonal thermocline, which in the tropics does not disappear during winter (Tomczak and Godfrey, 2013). The thermocline separates the subsurface from the deep ocean, isolating the latter from the atmospheric influence (Pedlosky, 1987; Stewart, 2008). In the subsurface, the interaction between the ocean and the atmosphere occurs mainly through heat and momentum fluxes (Fig. 1.2), being the Sea Surface Temperature the variable that better describes the heat content of the ocean.

Globally, SST is higher in the tropics, and diminishes toward the poles, due to the differences in incoming solar radiation (Fig. 1.3); however, there is a zonal temperature gradient in the oceans (mainly in the Atlantic and Pacific oceans), which makes the western side of the oceans warmer than the eastern side (Levitus, 1982). This is due to the aforementioned trade winds, which contribute to the piling of warm water towards the western boundaries of the oceans and the upwelling of cold water in the eastern boundaries. These two features are very conditioned by the behaviour of the mixed layer and the thermocline, as they are basic for the interchange and storage of heat between the atmosphere and the ocean. The SST can be considered as the mean temperature of the mixed layer, as the vertical temperature changes in that layer of the ocean are small. Its variations over time, therefore, are indicative of the heat interchanges between the ocean and the atmosphere. The evolution of the temperature in the mixed layer over time is a balance of several terms (Peter et al. 2006; Polo et al. 2015) and can be summarized in the next budget equation:

Equation 1.1: $\frac{\partial \bar{T}}{dt} \approx \frac{Q}{\rho_0 C_p h} + \frac{H_-(w_{-h}+w_e)(T(-h)-\bar{T})}{h} + \frac{1}{h}\left(-\bar{u}\frac{\partial \bar{T}}{\partial x} - \bar{v}\frac{\partial \bar{T}}{\partial y}\right)$,

where Q is the heat flux with the atmosphere, ρ_0 the density of seawater, C_p the thermal capacity of seawater, h the mixed layer depth (which is equal to the depth of the top of the thermocline), w_e the entrainment velocity, w_{-h} the vertical current at the base of the mixed layer, u and v the horizontal current components. $H_-(z) = 0$ for z < 0 and $H_-(z) = z$ for z ≥ 0. The second and third terms represent the vertical heat exchange with the interior of the ocean and the lateral transport of heat within the mixed layer respectively. They depend on the depth h of the mixed layer, that is, on the position of the thermocline, which highlights the importance of correctly assessing this variable for studies on atmosphere-ocean coupling.

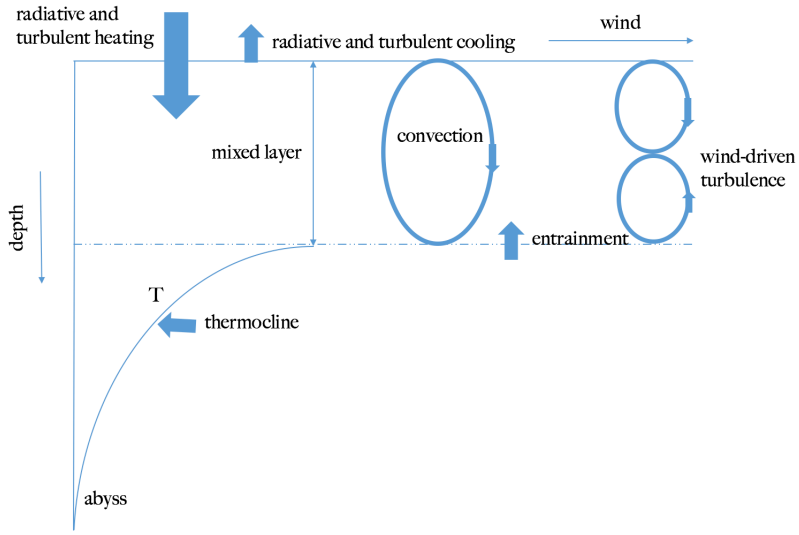

Figure 1.2: *Schematic of the heat interchanges in the mixed layer.*

The importance of the equatorial thermocline in tropical climate (and its implications for global climate) cannot be overstated, as it is fundamental for understanding ocean-atmosphere interaction processes (Zelle et al., 2004; McPhaden et al., 2006; Li and Xie, 2012). On the interannual time scale, the

thermocline in the equatorial Pacific is crucial for understanding the mechanisms associated with El Niño–Southern Oscillation (ENSO, Fig. 1.4), which develops from the ocean–atmosphere coupling in the tropical Pacific (McPhaden et al., 2006). El Niño constitutes the principal mode of interannual variability in the global SST (Trenberth, 1997) and has impacts throughout the globe (Trenberth et al. 1998; Alexander et al., 2002). The recharged oscillator mechanism proposed by Jin (1997) shows two feedbacks: the zonal advective feedback and thermocline feedback, which depends on the the mixed layer heat content. Recent work by Xu et al. (2017) posits that the apparition of one or the other of the two flavours of El Niño (Central Pacific El Niño or CP and Eastern Pacific El Niño or EP), as has been shown in recent years (Kao and Yu, 2007; Kug et al., 2009; Ren and Jin, 2011; Wang and Wang, 2013)_depends on the shape of the thermocline (fully tilted throughout the basin with a deepening in the western Pacific in the case of the EP or V shaped in the case of the CP). Their results point to the importance of the thermocline for the establishment of the CP El Niño, which adds to the already existent consensus about the relevance of the thermocline in the formation of the EP El Niño (McPhaden et al., 2006, Xu et al. 2017). A similar case can be made for the Atlantic Niño, which has also been shown to depend on thermocline reaction to wind forcings (Zebiak, 1993; Dippe et al., 2018; Lübbecke and McPhaden, 2017; Polo et al. 2015). Therefore, a well located thermocline that responds adequately to atmosphere forcings is fundamental for interpreting correctly the mean state and variability of tropical Pacific and Atlantic SSTs and their global impacts.

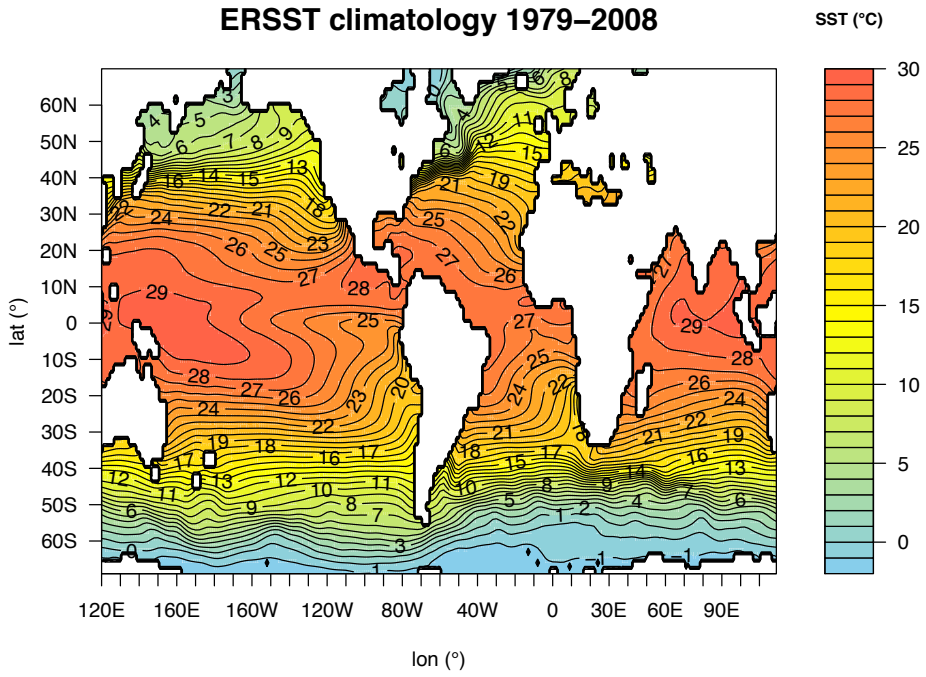

Figure 1.3: *Sea surface temperature annual climatology from reanalysis ERSST v3 (1979-2008).*

Historically, locating the thermocline in the ocean has been a difficult task, due to the lack of specialized equipment (Sverdrup, 1942). This fact led to an array of techniques of which the depth of different representative isotherms, as an estimate for the depth of the thermocline, was the most usual (Fiedler, 2010). The chosen isotherm depends on the latitude and the ocean studied in each case (Kessler, 1990; Yang and Wang, 2009). There are other methods which present advantages and disadvantages depending on the region studied (Fiedler, 2010). However, the representative isotherm is almost unanimously used in model studies is (e.g. Cai et al., 2004; Song et al., 2014; Li et al., 2015; Deppenmeier et al., 2016; Li et al., 2016). The isotherm usually selected to represent the thermocline in equatorial Pacific Ocean is 20°C (Lengaigne et al., 2012; Li and Xie, 2014; Xiang et al., 2017; Lübbecke and McPhaden, 2017; Martín-Rey et al., 2014). For the tropical Atlantic, the depth of the 22°C

isotherm (Deppenmeier et al., 2016) or 23°C isotherm (Cabos et al., 2017) has been used as representative of the thermocline.

With the development and general adoption of General Circulation Models (GCMs), the depth of a representative isotherm (generally the 20°C one, hereafter, z20) as an estimate of the thermocline depth was kept to compare model and observations, given the relatively poor vertical resolution of ocean models (Yang and Wang, 2009). *Coupled climate models are fundamental tools in the study of tropical variability. Thus the assessment of the reliability of the z20 estimate in these models is of great importance for the correct understanding of ocean-atmosphere coupling at the different scales in which thermocline varies.* Part of this variability can be attributed to wind-driven ocean circulation, which is described in the next section.

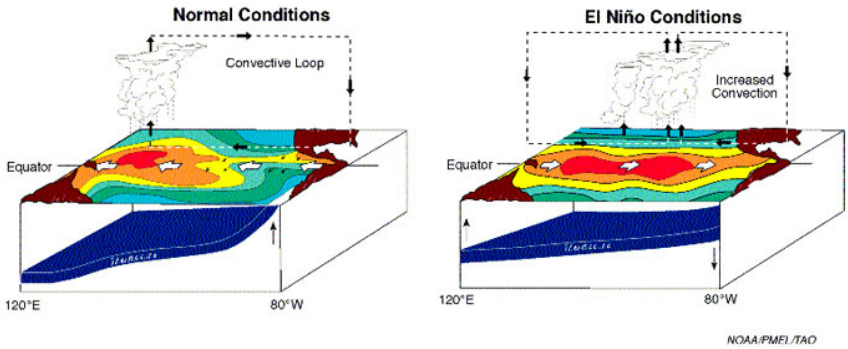

Figure 1.4: *Thermocline and Walker circulation climatological (left) and El Niño (right) conditions in the equatorial Pacific basin. Source: NOAA.gov.*

1.1.2 Wind driven circulation

Wind driven circulation is responsible for most of the global ocean upper-layer currents, being almost horizontal for the whole planet from a geostrophic

approximation[1]. The large-scale global wind field is dominated by westerly winds between 30° and 60° of latitude in the northern and southern hemispheres, and by easterly winds in the tropical/subtropical zone (the trade winds). The main ocean current system consists of large anticyclonic geostrophic gyres. They rotate clockwise in the Northern Hemisphere and anticlockwise in the Southern Hemisphere. There are five major geostrophic gyres: North Atlantic, South Atlantic, North Pacific, South Pacific and Indian Ocean Gyre (Fig. 1.5). In addition, the Antarctic Circumpolar Current is situated in the Southern Ocean, uninterrupted by any land masses. It is an eastward-flowing current driven by dominant westerly winds.

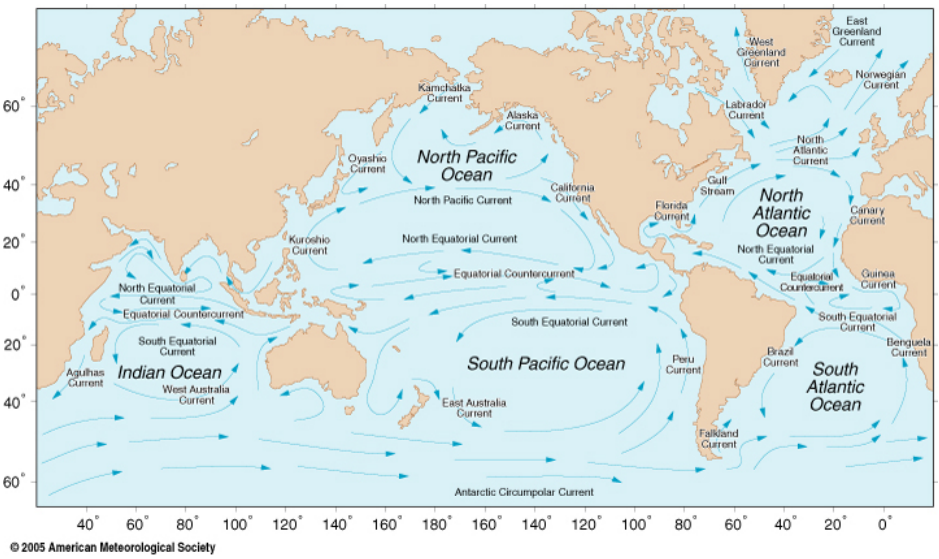

Figure 1.5: *Main features of the wind-driven surface ocean circulation. Source: oceanmotion.org*

However, the impact of winds on ocean currents is not as straightforward as might seem when looking at, for example, the equatorial trade winds. Ocean

1 The geostrophic approximation balances the pressure gradient force with the Coriolis Force. In this approximation, regions with strong pressure gradients are characterized by winds flowing parallel to the isobars, with the higher pressures on the right (left) in the northern (southern) hemisphere.

water displacement does not always follow the wind direction, because of friction with the boundaries.

Ekman spiral and Ekman pumping

The momentum equations in the ocean layer affected by the wind, considered as a homogeneous, steady state layer limited by a horizontal surface are:

Equation 1.2: $$\rho_0 f v E - \frac{\partial \tau_x}{\partial z} = 0, -\rho_0 f u E - \frac{\partial \tau_y}{\partial z} = 0,$$

Where ρ_0 is the density of seawater, f the Coriolis parameter, τ_x and τ_y the zonal and meridional components of wind stress on the surface and v and u the zonal and meridional velocities of the fluid. Trying to understand wind-driven currents has been the focus of research of several scientists for the best part of the 20th century. The first formal proofs of this effect were provided by Fridtjof Nansen's trip in 1893 after observing how his research vessel *Fram*, which he had let become locked in the Arctic ice pack, consistently displaced 20° to 40° to the right of the prevailing wind direction. The mathematical model for this phenomenon (Fig. 1.6) is known as the Ekman spiral (Ekman, 1905). The Ekman spiral describes how the velocity of each layer of fluid is deviated and braked (because of friction) from that of the layer above, forming a downward spiral. The layer from the surface to the region in which the currents have fully turned is called the Ekman layer (Ekman, 1905). Ekman proposed a depth for this layer given by formula $D_E = \frac{7.12}{\sqrt{\sin |\varphi|}} U_{10}$, where U_{10} is the wind velocity at 10 meters and φ is the latitude. This gives a depth of up to 200 meters in the subtropical latitudes. The integration of all the velocities along the Ekman layer is a measure of the total transport within the layer.

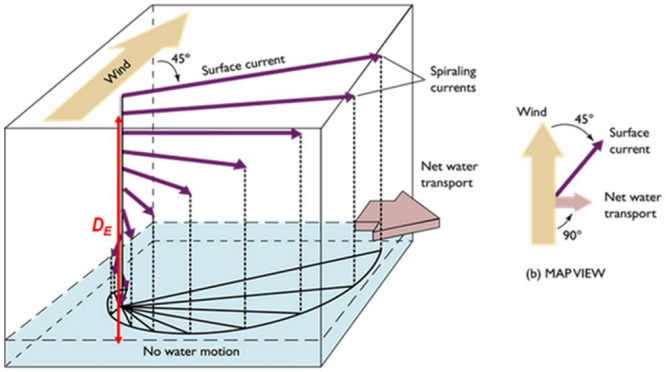

Figure 1.6: *Schematic of Ekman spiral in the Northern Hemisphere. Purple lines indicate the velocity of current at each level in the Ekman layer (velocity decomposed as u_E in the zonal direction, v_E in the meridional direction). The big pink arrow shows the integrated net water transport M_E (to the right of the wind).*

Mass transport is of special interest for us, because its calculation is much more straightforward and depends on less assumptions than velocity calculation, thus being more robust. Horizontal mass transport (Eq. 1.3) due to wind stress occurs 90° to the right of the wind direction (left in the Southern Hemisphere).

Equation 1.3: $$M_{E_x} = \int_{-d}^{0} \rho_0 u_E dz, M_{E_y} = \int_{-d}^{0} \rho_0 v_E dz,$$

where u_E and v_E are the components of velocity in the Ekman layer. This, together with the momentum equations (Eq. 1.2) get us Eq. 1.3.1:

Equation 1.3.1: $$fM_{E_x} = -\tau_x \text{ and } fM_{E_y} = \tau_y$$

Where τ_x and τ_y are the zonal and meridional components of the wind stress at the surface. Mass transport leads, due to the continuity of the fluid, to upwelling (meaning the surging of water from deeper layers of the ocean due to the displacement of the surface water via Ekman pumping), which is one of the points of interest of this thesis. The upwelling term is obtained (Eq. 1.5) by

integrating the divergence of mass transport in the Ekman layer, taking as boundary condition in the bottom $w_E = 0$:

Equation 1.4: $$\frac{\partial M_{E_x}}{\partial x} + \frac{\partial M_{E_y}}{\partial y} = -\rho_0 w_E(0),$$

where ρ is the water density and w_E is the vertical velocity in the upper layer of the ocean.

Equation 1.5: $$w_E(0) = \left[\frac{\partial}{\partial y}\left(\frac{\tau_x}{f}\right) - \frac{\partial}{\partial x}\left(\frac{\tau_y}{f}\right)\right] = curl\left(\frac{\tau}{\rho_0 f}\right)_k,$$

where τ is the vector wind stress and f is the Coriolis parameter.

Sverdrup transport

Over larger areas, such as a single oceanic gyre, quasi-geostrophic balance must be taken into account. Sverdrup (1942) obtained that the horizontal transport of mass due to surface winds in the tropics (where the wind is zonal) is Eq. 1.6:

Equation 1.6: $$\vec{V} = \frac{\mathrm{k} \times (\nabla \times \tau)}{ß}$$

where $(k \times \nabla \times \tau)$ is the horizontal wind stress curl (τ being the wind stress and k the unit vector in the vertical direction) and ß the rate of change of the Coriolis parameter with latitude. Since the winds along the Equator are mainly zonal, the Sverdrup transport in and out of the equatorial region occurs in the meridional direction. This makes the meridional transport (Eq. 1.7):

Equation 1.7: $$V_y \approx -\frac{1}{ß}\frac{\partial \tau_x}{\partial y}$$

with ß $= \frac{2\Omega cos\varphi}{R}$, being R the Earth's radius, φ the latitude and Ω the rotation rate of the Earth (Ω = 7.2921 × 10^{-5} rad/s).

One of the prime examples of the effects of wind stress on the surface of the ocean is the coastal upwelling. The importance of coastal upwelling is multiple: it enhances primary production, which increases fish abundance (Dugdale, 1972; Bakun, 1990; Field et al., 1980); it cools local weather via the surge of colder water from the deep ocean (Xiu, 2018). Coastal upwelling areas make up only 2% of ocean surface, but they account for more than 20% of the global fish captures (Sydeman et al., 2014). This makes them of a great ecologic and economic interest.

Coastal upwelling occurs in regions where there are strong and sustained surface winds parallel to the coast (Bakun, 1990). These winds blow over the ocean and affect surface water through frictional drag. The velocity of the water current is generally around 2% of the wind speed. However, as explained in the previous section, due to the rotation of the Earth, the water dragged by the winds is not displaced parallel to the wind, but 90° to the right (left) in the NH (SH). The effect of this net transport is to displace surface water, generally warmer than that in deeper layers of the ocean, away from the coast, driving cold and nutrient-rich water from deeper layers of the ocean up to the surface (Fig. 1.7).

The four great eastern boundary systems or upwelling areas (California, Peru, Canary and Benguela) are all located in tropical or subtropical latitudes in the western coast of the continents (Wang et al. 2015). This location is due to the existence of the subtropical anticyclones, that make winds flow along the western coasts from the North in the Northern Hemisphere and from the South in the Southern Hemisphere, producing Ekman transport and therefore creating the conditions for the appearance of the coastal upwelling regions. It is important to note that the effects of coastal upwelling are felt up to about 100 kilometres from the coast, albeit they are much stronger closer to the coast (Estrade et al., 2008).

In order to study upwelling intensity and behaviour, an upwelling index is defined. This index is a simplification of Eq. 1.5, in which we introduce.: $\frac{\partial}{\partial y}\left(\frac{\tau_x}{f}\right) = 0$ in our region of interest, where the wind is almost exclusively northerly. In addition, in a very narrow region along the coast, $\frac{\partial}{\partial x}\left(\frac{\tau_y}{f}\right)$ is proportional to $\frac{\tau_y}{f}$. The result is Eq. 1.8 (González-Nuevo et al., 2014). The resulting index takes explicitely into account the effect of the wind stress, but not the intensity of the thermocline and the entrainment velocity.

Equation 1.8: $$upw.ind. = \frac{\tau_y}{2\Omega sen(\varphi)}$$

However, the effects of wind-driven coastal upwelling on surface temperature depend not only on the strength of the wind, but also on its ability to upwell cold water to the surface. This, in turn, depends on the location and strength of the thermocline: a deep thermocline, or a shallower but too stable one, will be less affected by the wind stress. Conversely, a shallow and weak thermocline will make it easier for cold water to reach the surface, thus impacting SST (Richter 2015). This is reflected on the second term of Eq. 1.1. The variations in temperature in the mixed layer due to vertical movements depend on the depth of the thermocline, and also on the vertical velocity (entrainment), which is conditioned by the strength of the thermocline (Li et al., 2002; Xu et al., 2017).

The cool waters arising at the surface produce a strong zonal gradient of SST close to the coast line. For this reason, there are works that use a SST-based upwelling index as the difference between SST in the coast and the SST of a gridpoint located 5º out of the coast (Santos et al., 2005, Benazzouz et al., 2014). This index has the advantage of being useful in regions where the prevailing winds are not meridional. However, for the the Northwest African coast, the two indices have been compared and the results were similar (Sylla et al., 2019). Additionally, the use of a wind-based coastal upwelling index allows to evaluate the effect of the wind on the ocean, which will be one of the focal points of this thesis. From now on, *upwelling* will be used as a shorthand for wind-driven coastal upwelling.

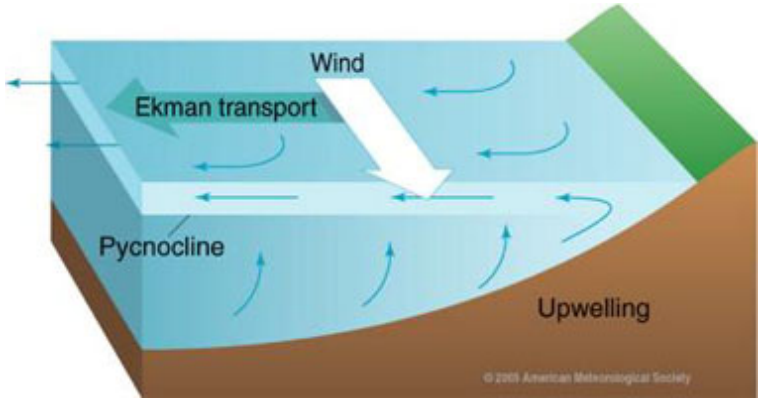

Figure 1.7: *Ekman transport perpendicular to the coast. With a latitudinal coastline (in green) and northerly winds (white arrow), the superficial transport (above the pycnocline, which is generally coincident with the thermocline) occurs to the west. Colder water from below the thermocline substitutes the displaced surface warmer water. Source: oceanmotion.org*

1.1.2.2 Northwest Africa upwelling

The Northwest African (NWA) upwelling system is located between 13° North and 35° North (Fig. 1.8), in front of the North African coast (Wang et al., 2015; Pauly and Christiansen 1995). It is part of the greater Canary Eastern Boundary Upwelling System (sometimes referred to as the North Atlantic Eastern Upwelling System), which extends from Cape Blanche to the northern tip of the Iberian Peninsula (Wang et al., 2015; Barton et al., 2013). The exact zone we will study stretches from 10°N to 25°N and from 20°W to 15°W.

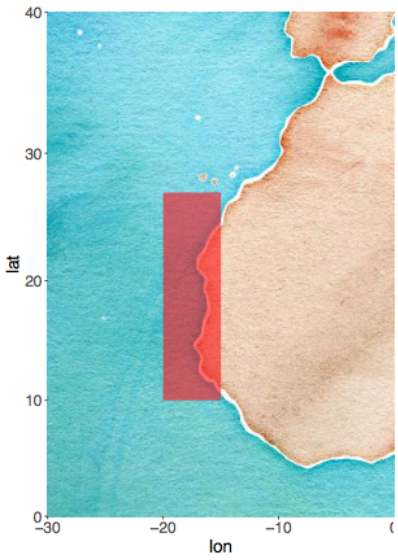

Figure 1.8: *Region of study (Chapter 4 and 5).*

Climate change is predicted to have an impact on the intensity and position of the NWA upwelling, although there is no consensus on which changes are to be expected. The seminal work on this matter (Bakun, 1990) posited that there would be an increase in alongshore winds under global warming due to: a) the intensification of subtropical anticyclones, and b) the increased land-sea surface temperature contrast (land is warming faster than oceans), which contributes to channel winds along the coast. Further studies have coincided on asserting that trend (Narayan et al., 2010, Wang et al., 2015). However, Barton et al., (2013) assert that it is risky to establish a trend on wind intensification for the last decades (in which the effects of global warming are already felt), since there are important discrepancies among databases. In their work, this is consistent with the increasing sea surface temperature.

However, a good understanding on how coupled models reproduce the present and past of the NWA upwelling is fundamental for any analysis of future scenarios. Although it is known that CMIP5 models show very little SST bias in that region (Wang et al., 2014), the fine scale of coastal upwelling

has led most authors to use regional models (Soares et al., 2018) or satellite observations (Benazzouz et al. 2014) in their studies of the NWA upwelling. Recent works however, have assessed the behaviour of the upwelling in CMIP5 historical simulations (Sylla et al., 2019). *In this case, the assessment of present upwelling has been performed through wind-based and also through SST-based indices, which might be subjected to biases of ocean origin. Furthermore, the question of how do large scale model features affect NWA upwelling remains open.* These studies have also shown that a slight weakening of the southern part of the upwelling region is predicted under CMIP5 future scenario RCP8.5 (high atmospheric carbon dioxide concentration), which is linked to large-scale circulation features such as the northward migration of the Azores Anticyclone, as well as regional SLP variations over West Africa. *One of the main goals of this thesis will be to assess CMIP5 model behaviour in the simulation of NWA upwelling, as well as studying how large-scale biases affect that representation.*

1.2 Coupled global circulation models and their biases

Coupled global climate models (CGCMs) are one of the most useful tools for studying present, past and future climate. They are computational tools that solve the fundamental equations of physics governing global climate (Hartmann, 1994). They generally consist of an atmosphere model and an ocean model (together with different specific moduli regarding chemistry, biogeochemistry, land or sea ice), which are coupled in order to represent the most comprehensive possible picture of the global climate system.

The 5th phase of the coupled model intercomparison project (CMIP5) provides an advantageous platform to inter-compare GCMs (Taylor, 2012). CMIP5 is the more recent phase of the CMIP project, which calls for multimodel sets of experiments on climate variability and climate change. CMIP5 is designed so that it offers both projections of future climate (from 2035 onwards) and historical simulations (from 1850 to the present). Control runs, which use preindustrial radiative forcing conditions (and are therefore known as preindustrialControl or piControl) are also run to serve as a baseline

for each model. They enable researchers to study the unforced internal variability of models. All the CMIP5 simulations used in this thesis belong to this group. It is important to note that these simulations are in average colder than the historical simulations used in other studies (e.g. Wang et al. 2015), due to they not being subjected to the historical radiative forcing (which integrates the effect of global warming in the models).

Even though they represent the state of the art of modelling, CMIP5 models suffer from important biases (Fig. 1.9). Some of these biases are those found in the tropical Pacific, producing an excessively strong and narrow cold tongue and a double intertropical convergence zone (Bellucci et al., 2010; Li and Xie, 2014; Oueslati and Bellon, 2015; Xiang et al., 2017). Many works have tried to ascertain the origin of these errors and most trace them to a deficient dynamic feedback mechanism between the atmosphere and the ocean in coupled models (Bjerknes, 1969; Li et al., 2015; Li et al., 2016; Richter, 2015; Li and Xie, 2014). The appearance of the southern branch of the ITCZ (and its associated rain excess south of the Equator) has been traced to local problems in the South Eastern Pacific, such as an incorrect representation of the stratocumulus deck, but also to the excessive warming of the Southern Ocean (Mechoso et al., 2016; Kang et al., 2009). This problem can be traced to excessive shortwave input in the Southern Ocean due to the too low cloud optical thickness and/or too small cloud fraction (Stanfield et al., 2015; Kang et al., 2009; Hwang and Frierson, 2013), which affect the position of the ITCZ via alterations in the Hadley circulation and the interhemispheric energy fluxes (Kang et al., 2008).

Regarding the tropical Atlantic Ocean, GCMs are also afflicted by serious biases (Richter, 2015; Zuidema et al., 2016) that affect both SST variability (Richter et al., 2014) and basin feedback processes (Nnamchi et al., 2015.; Ding et al., 2015; Voldoire et al., 2014). Of particular interest to our study is the relationship between a too weak wind and a badly represented thermocline (Richter et al., 2014). This affects the feedback processes, mainly the formation and maintaining of the equatorial cold tongue (Richter et al., 2014; Voldoire et al., 2014), which is one of the main features of the equatorial Atlantic atmosphere-ocean interaction, and the recharged oscillator

mechanism which explains ENSO alternance between positive (Niño) and negative (Niña) phase (McPhaden, 1999; Dommenget, 2019).

It is also known that models show warm biases in the upwelling regions. These biases have been traced back to a series of issues: underrepresentation of the low-level stratocumulus deck over the southeastern tropical Atlantic that leads to an excessive shortwave flux into the ocean and warming (Hwang and Frierson, 2013); overestimation of near-surface humidity by the atmospheric component of GCMs, leading to too low evaporative cooling (Hourdin et al., 2015); advection of equatorial warm bias by Kelvin waves, spurious barrier layers (Breugem et al., 2008) and problems in the representation of ocean currents (for the Benguela and Angola upwelling, Xu et al., 2014).

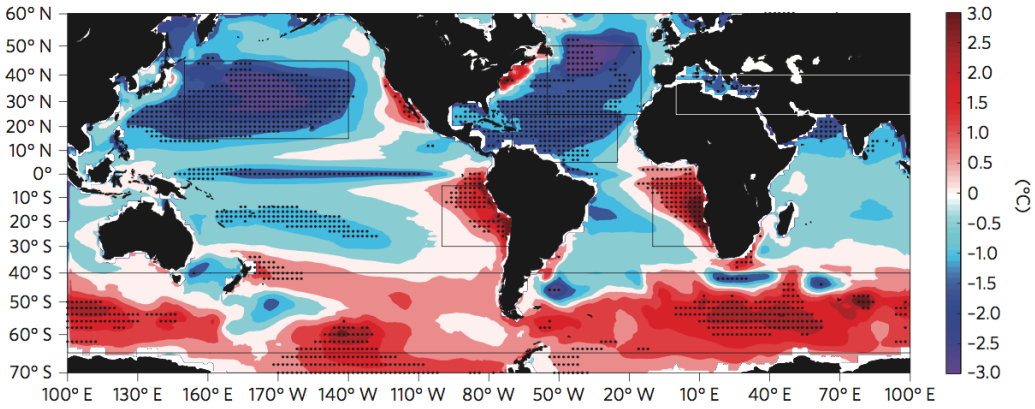

Figure 1.9: *Mean SST bias for CMIP5 historical simulations ensemble. (Wang et al., 2014).*

This thesis looks into the representation of atmosphere-ocean coupling in models, which depends, among other things, on the ocean model properly representing the vertical thermal and density structure of the water column. *An inadequate stratification of the ocean has been shown to lead to poor representation of atmosphere-ocean phenomena such as the ENSO and upwelling (Richter, 2015). CMIP5 models show a not well defined thermocline (Guilyardi et al., 2009), where the stratification is however too*

strong when compared to observations (Chapter 4 of this thesis). This prevents atmospheric forcings (wind stress, heat fluxes) to adequately affect the behaviour of the water column. Moreover, the strong gradient that is present in most models causes important subsurface thermal biases. One of the goals of this thesis is, therefore, to characterise subsurface biases in coupled models in upwelling regions, and explore how ocean model biases affects upwelling representation and response to wind stress.

1.3 Thesis objectives

The main objective of this thesis is to improve the understanding of how the upper tropical ocean reacts to wind forcing in the tropics both in coupled models and observations. The main regions are the equatorial and coastal upwelling regions, focusing, for the former, in the Pacific and Atlantic thermocline and, in for the latter, in the Northwest African upwelling. In particular we try to answer the following research questions:

Chapter 3: Revisiting the CMIP5 thermocline in the Atlantic and Pacific Oceans

The depth of the 20°C representative isotherm is the most widely used estimate of the thermocline depth both in coupled models and in observations. However, its equivalence to the physical thermocline in coupled models has not been thoroughly studied.

RQ3.1: Is the 20°C isotherm a good estimate of the equatorial thermocline?

RQ3.2: What are the consequences of using the physical definition of the thermocline and the 20°C isotherm?

Chapter 4: Representation of Northwest African upwelling in reanalysis and CMIP5 models

CMIP5 is one of the most widely used tools in climate studies. However, coupled models have some known biases that can affect the simulation of regional scale phenomena such as the NWA upwelling.

RQ4.1: How is NWA upwelling seasonal cycle simulated by CMIP5 models?

RQ4.2: Do models reproduce the observed local relation between upwelling, SSTs and thermocline depth and intensity?

RQ4.3: What are the large scale features controlling the different representation of NWA upwelling in climate models?

Chapter 5: Sensitivity of Northwest African upwelling to ITCZ shifts

The position of the ITCZ appears to be a key factor in the model representation of NWA upwelling. Shifts in the ITCZ have been related to extratropical energy perturbations.

RQ5.1: How does ITCZ shifts due to changes in the large-scale extratropical incoming energy affect NWA upwelling representation?

2 Data and methodology

2 Data and Methodology

2.1 Reanalysis and observational data

This thesis uses an array of data both from coupled climate models and from reanalysis and observational sources, which will be grouped together as the benchmark against which model data is compared. The model data is studied in the next section, while this section provides an overview of the observational and reanalysis databases used.

For ocean potential temperature data, the chosen reanalysis has been the Simple Ocean Data Assimilation (SODA) reanalysis v2 (Carton et al., 2005), which covers the period from 1871 to 2008 with a 1° x 1° resolution. TAO buoys have also been used for the equatorial Pacific (10 buoys between 147°E and 95°W at 0°N, with variable vertical resolution and covering the period 1981-2010). The wind stress data has been obtained from the Wave and Anemometer-based Sea Surface Wind (WASwind) database, which spans from 1950 to 2009 with 4°x 4° resolution (Tokinaga and Xie, 2011). The source for sea surface temperature has been the Extended Reconstructed Sea Surface Temperature (ERSST) v3b (Smith et al., 2008), available from 1854 to 2008 at a 2°x2° resolution. Daily precipitation monthly means have been obtained from the Global Precipitation Climatology Project v2.2 (GPCP), available from 1979 to 2015 with a 2.5°x2.5° resolution (Adler et al., 2003), and sea level pressure (SLP) monthly data comes from the Hadley Centre's mean sea level pressure or HadSLP2r, an update of the Global Mean Sea Level Pressure which runs from 1860 to the present with a 5°x5° resolution (Basnett and Parker, 1997; Allan and Ansell, 2006). For all datasets the one chosen has been the 1979-2008 period, for a combination of availability of all variables and reliability of the data due to satellite measurements being incorporated to the datasets. The temporal resolution of all datasets is one month. Most calculations have been performed using monthly data, although seasonal and annual climatology has been computed in some cases.

The main results of this thesis concern the tropical region. For Chapter 3, the areas of study are the Tropical Pacific and the Tropical Atlantic. Three

regions have been selected to study the equatorial thermocline: western Pacific (160°E to 140°W, 5°S to 5°N), eastern Pacific (110°W to 80°W, 5°S to 5°N), and Atlantic (30°W to 10°W, 5°S to 5°N). For chapter s4 and 5, the focus is on the Northwest African upwelling region, located between 15°W and 20°W and 10°N and 25°N (Fig. 2.1).

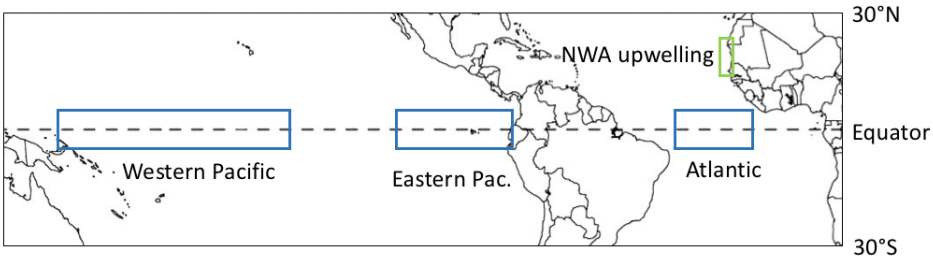

Figure 2.1: *Map of the regions studied in this thesis. The regions of interest in chapter 3 are marked in blue, and the region studied in chapters 4 and 5 is shown in green.*

2.2 Model data

2.2.1 CMIP5

This study uses data from 24 models from the CMIP5 ensemble (Table 2.1; Taylor et al., 2012). These 24 models have been chosen as a compromise between having a diverse enough ensemble of models and data availability at the moment of conducting the studies. Variables used from these 24 models are: ocean potential temperature (thetao), surface wind stress, SST, daily precipitation, net radiation at the surface, cloud fraction and sea level pressure. In Table 2.1 the original resolution of the atmosphere grid is shown. The ocean grid in the tropical regions is, in all cases, finer than the atmospheric one, being in some cases as fine as 0.3° in latitude by 1° in longitude. The CMIP5 models and reanalysis data have been interpolated to the 1° x 1° SODA grid in latitude by longitude. Regarding the ocean temperature, each model has a different vertical resolution. This makes difficult to intercompare

them without regridding to a common vertical dimension, which can be delicate for such a fine-detail study as this. Therefore, no vertical interpolation has been performed for the calculation of the thermocline depth, and only CMIP5 models' ocean temperature has been regridded to the CCSM4 model vertical grid for plotting the ensemble temperature profile.

We have chosen to evaluate the monthly climatology from preindustrial control simulations, which provides very long time series without the influence of varying radiative forcing. The most central 200-year segment for each model has been used to compute our climatologies for 23 of the models as a compromise between having the maximum possible series for each model and giving all of them the same weight in the ensemble. For one of them (MIROC-ESM-CHEM) only 100 years were available, and that has been the length chosen. Many CMIP5 bias studies use historical runs rather than preindustrial control runs (Wang et al., 2014 and Fig. 1.8 of this thesis). However, the SST bias for the preindustrial simulations shows the same general pattern than the historical simulations (Wang et al. 2014).

	Model name	Institution and country	Atmospheric grid (lat x lon)	Ocean model and horizontal resolution (lat x lon)
1	ACCESS1-0	CSIRO (Commonwealth Scientific and Industrial Research Organisation), Australia, and BOM (Bureau of Meteorology), Australia	1.25° x 1.875°	ACCESS-OM (0.3° x 1°)
2	Bcc-csm1-1	Beijing Climate Center (BCC), China Meteorological Administration, China	2.791° x 2.813°	MOM4-L40 (0.3° x 1°)
3	BNU-ESM	GCESS, BNU, Beijing, China	2.791° x 2.813°	MOM4p1 (0.3° x 1°)
4	CanESM2	CCCma (Canadian Centre for Climate Modelling and Analysis), Canada	2.791° x 2.813°	Included (0.35° x 1.875°)
5	CCSM4	NCAR (National Center for Atmospheric Research), USA	0.942° x 1.25°	POP2 (0.3° x 1°)
6	CESM1-CAM5	NSF/DOE NCAR (National Center for Atmospheric Research), USA	0.942° x 1.25°	POP2 (0.3° x 1°)
7	CMCC-CMS	CMCC (Centro Euro-Mediterraneo per i Cambiamenti Climatici), Italy	3.711° x 3.75°	POP2 (0.3° x 1°)
8	CNRM-CM5	CNRM (Centre National de Recherches Meteorologiques, Meteo-France) and CERFACS (Centre Européen de Recherches et de Formation Avancée en Calcul Scientifique), France	1.401° x 1.406°	NEMO-ORCA1 (0.7° x 0.7°)
9	CSIRO-Mk3-6-0	CSIRO (Commonwealth Scientific and Industrial Research Organisation), BOM (Bureau of Meteorology), Marine and Atmospheric Research and QCCCE (Climate Change Centre of Excellence), Australia	1.865° x 1.875°	MOM2.2 (0.9° x 1.875°)
10	FGOALS-g2	IAP (Institute of Atmospheric Physics, Chinese Academy of Sciences) and THU (Tsinghua University), China	1.659° x 2.813°	LICOM2 (0.5° x 1°)
11	GFDL-ESM2G	NOAA GFDL, USA	2.023° x 2°	GOLD (1° x 1°)
12	GFDL-ESM2M		2.023° x 2.5°	MOM4.1 (1° x 1°)
13	GISS-E2-H	NASA/GISS (Goddard Institute for Space Studies), USA	2° x 2.5°	HYCOM (0.3° x 1°)

	Model name	Institution and country	Atmospheric grid (lat x lon)	Ocean model and horizontal resolution (lat x lon)
14	GISS-E2-R	NASA/GISS (Goddard Institute for Space Studies), USA	2° x 2.5°	Russell Ocean (1° x 1.25°)
15	HadGEM2-CC	Met Office Hadley Centre, UK	1.25° x 1.875°	Included (1.25° x 1.875°)
16	HadGEM2-ES		1.25° x 1.875°	Included (1.25° x 1.875°)
17	inmcm4	INM (Institute for Numerical Mathematics), Russia	1.5° x 2°	Included (0.5° x 1°)
18	IPSL-CM5A-LR	IPSL (Institut Pierre Simon Laplace), France	1.895° x 3.75°	NEMO-ORCA2 (2° x 2°)
19	MIROC-ESM-CHEM	JSMSTEC (Japan Agency for Marine-Earth Science and Technology), AORI (Atmosphre and Ocean Research Institute, University of Tokyo) and NIES (National Institute for Environmental Studies), Japan	2.791° x 2.813°	COCO3.4 (0.6° x 1.4°)
20	MIROC4h		0.562° x 0.563°	COCO3.4 (0.2° x 0.2°)
21	MIROC5		1.401° x 1.406°	COCO4.5 (0.6° x 1.4°)
22	MPI-ESM-LR	Max Planck Institute for Meteorology, Germany	1.865° x 1.875°	MPI-OM (1° x 1.4°)
23	MRI-CGCM3	MRI (Meteorological Research Institute), Japan	1.121° x 1.125°	MRI-COM3 (0.5° x 1°)
24	NorESM1	Norwegian Climate Centre, Norway	1.895° x 2.5°	NorESM Ocean (1.125° x 1.125°)

Table 2.1: *List of the models used in the study: number used in the study, model name, institution and country and horizontal resolution of the atmosphere and oceanmodels.*

2.2.2 UCLA CGCM

In this work, two different long simulations have been performed with the UCLA general circulation model at the University Complutense of Madrid. The description of these simulations can be found in section 2.3.2.

The UCLA general circulation model consists of the UCLA atmospheric GCM (AGCM) 7.1 (Mechoso et al., 2000; Ma et al., 2013) coupled to the MIT oceanic GCM (OGCM) (Marshall et al., 1997). The AGCM part is a state-of-the-art model. It was one of the first models to use a finite-difference approach to fluxes, which later became generalized (Mechoso et al., 2000), and it has experienced continuous improvements that make its performance comparable to that of most modern models. In this thesis we use a version with a sigma vertical coordinate up to 1 hPa, with 29 layers, 14 in the stratosphere. In the horizontal, the differentiation of the primitive equations is performed in an Arakawa-C grid with resolution of 2° latitude by 2.5° longitude. In the version of the UCLA AGCM used, the lowest model layer is assigned to the Plantary Boundary Layer (PBL), which is a unique feature of the model. The depth of this layer is predicted through the mass budget equation including the PBL-top entrainment, cumulus mass flux, and horizontal mass convergence within the PBL. When the entrainment and cumulus mass flux become zero, the PBL-top becomes a material surface, keeping the PBL air separated from the free atmosphere air. Processes crucial for a cloud-topped PBL are explicitly formulated. We refer to the clouds that form above the lifting condensation level within the PBL as stratocumulus (SCu). These are assumed to individually or together represent fog if the cloud base extends to the ground, as observed in nature. The radiative cooling at the top of SCu contributes to the generation of turbulence and the mass entrainment from the free atmosphere. This model incorporates the Simplified Simple Biosphere Model (SSIB) (Xue et al., 1991). The MIT OGCM version used has 46 vertical levels to a maximum depth of 5815 m and covers the ocean domain from 80°S to 79°N. In longitude, the resolution is 1°; in latitude the resolution is 0.3° between 10°S-10°N, increasing up to 1° out of the tropics.

2.3 Methodology

In this section we introduce the algorithms and analysis tools developed and used for this thesis. The first two sections are dedicated to the methods and experiments more specific of this work, while the Analysis of data section lists the statistical and graphic tools utilised.

2.3.1 Localization of the thermocline

The main goal of Chapter 3 of this thesis is to improve the determination of thermocline depth. As was mentioned in Chapter 1, there are several methods for estimating the thermocline depth. In this thesis depth of the 20°C isotherm and depth of the maximum thermal vertical gradient will be used. Both the 20°C isotherm depth (z20) and the maximum vertical gradient are estimated from the 3D ocean potential temperature. In order to be faithful to the vertical structure of the data, every operation is made on the original vertical layers for each model and the reanalysis, so no interpolation is performed in that direction.

For z20, the layer with the temperature closest to 20°C among those higher than 20 is selected (z20+), as well as the layer with the temperature closest to 20°C among those cooler than 20 (z20-). Then, z20 is estimated by linear interpolation between those two layers. Vertical temperature inversions, which could lead to the existence of two 20°C isotherms in the ocean, are usually related to seasonal variability (Mignot et al., 2012). A test has been performed for each gridpoint in order to check whether there was any thermal inversion in the first 500 meters, and it was found that these situations were very infrequent, happening in less than 0.5% of the cases. Therefore, the points in which this occurred were taken out of the computations.

Regarding the depth of the maximum vertical temperature gradient, we first compute the vertical gradient for each two consecutive layers (Z_{lev1} and Z_{lev2}) as:

Equation 2.1: $$g_t = \frac{-(T_{lev2} - T_{lev1})}{(Z_{lev2} - Z_{lev1})},$$

where T_{lev1} and T_{lev2} are the temperature of the layers characterised by Z_{lev1} and Z_{lev2} respectively. Second, the maximum value of the vertical gradient is obtained. Since this maximum gradient characterizes a depth between two layers, we assign the depth of the thermocline to the middle point between those two layers. By design, the method cannot be more precise than half the width of the level. For most models, this provides a precision of 5 meters for most models in the layers between the surface and 200 meters deep, which encompass almost all of the results found in our study.

The two methods are applied to compute the thermocline depth for all the points between 5°S and 5°N, then the results are averaged in latitude to find the mean equatorial depth as a function of longitude. Hereafter we will refer to the depth of the maximum vertical temperature gradient as the depth of the thermocline.

2.3.2 UCLA GCM experiments

Along this work, two different simulations with the UCLA CGCM were performed in order to study the impact of changes in the large scale circulation on the NWA coastal upwelling.

UCLA CONTROL

First, a 100-yr control simulation is performed. In order to avoid initial drifts, only the last 85 years are analyzed. The initial conditions of the simulation come from a previous long control run. No external forcings are included other than CO2, which is set to a constant concentration consistent with 1980 levels (Mechoso et al., 2016).

UCLA Sensitivity Experiment: COSZ

Secondly, to evaluate the effect of a shift in the position of the ITCZ on NWA coastal upwelling, a sensitivity experiment is performed, applying a reduction in the incoming solar radiation over the Southern Ocean. This experiment is called COSZ (as an acronym of the modification of the solar angle of incidence for the latitudes in which the perturbation is applied). The aim of such experimental design is to emulate a reduction in the warm bias observed in GCMs over the Southern Ocean (Kang et al., 2009; Wang et al. 2014) and its influence in shifting the ITCZ southwards. The rest of the simulation setting is the same as the Control run (1980-conditions radiative forcing), except for the length, which is 40 years, of which the last 25 are used in order to avoid any possible initial model drift.

To implement the perturbation to the model we multiply the time-varying solar radiation incident normally at each latitude circle by the factor:

Equation 2.2 $$f = 1 + \alpha * \sin(\varphi + 30°) * \sin(\varphi + 60°)$$

where φ is latitude. The value of α is 1.5 for θ between 60°S and 30°S, and zero otherwise. This results in a strong reduction of incoming shortwave radiation at the top of the atmosphere (TOA) over the southern extratropics, with a maximum amplitude at 45°S (Fig. 2.2). The mean reduction in the incoming solar radiation over the southern hemisphere is 8.14 W/m2. From now on we will refer to this experiment as COSZ.

To study the impact of such modifications in the global climate, the results of COSZ are compared to UCLA control by subtracting the value of a particular variable in the control to the value of the same variable in COSZ. The results show that the modification of the incoming radiation in the southern extratropics produces changes at a global scale. Among them, it is specially remarkable the reduction of the net radiation at the top of the atmosphere over the Southern Ocean and the eastern borders of the Southern Atlantic and Pacific oceans, as well as the northward shift of the ITCZ (Mechoso et al., 2016).

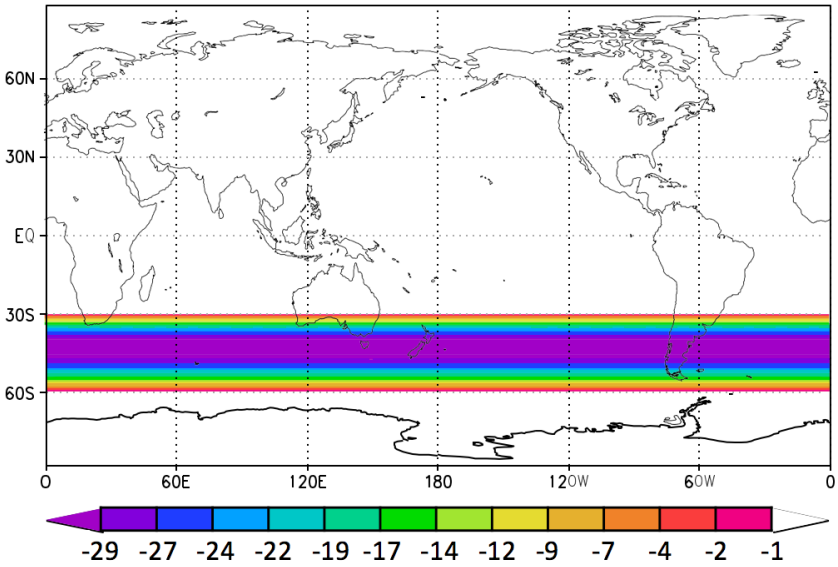

***Figure 2.2**: Change in incoming shortwave radiation at TOA in sensitivity experiment. Difference in incident shortwave solar radiation between sensitivity experiment and control run at the top of the atmosphere (W/m²).*

2.3.3 Analysis of data

2.3.3.1 Empirical Orthogonal Functions (EOFs) analysis

The Empirical Orthogonal Functions (EOFs) analysis was introduced in meteorology by Hotelling (1935), and described by Lorenz (1956) and it is widely used in oceanic and atmospheric sciences.

In this thesis, EOFs have been applied on month-latitude Hovmöller plots. These plots show, in the x-axis, time (12 months, in our case), and a spatial variable in the y-axis (latitude in most of our calculations). They allow us to study how a certain spatial field varies with time. Hovmöller plots have, therefore, time-space dimensions.

Part of the work done in this thesis deals with intermodel variability within the CMIP5 ensemble. For this intermodel study, the EOF technique decomposes the anomalous field into a number of modes which maximize the variance of a two-dimensional matrix Y(ns,nm), being ns a spatio-temporal dimension (given by month-latitude plots) and nm the number of models. The application of the EOF analysis provides a set of spatio-temporal structures (EOFs) and associated model series (Principal Components, PCs), which together describe the modes of variability (Fig. 2.3).

Starting with a given field $Y(ns,nm)$, the anomalies are calculated by subtracting the ensemble mean $\bar{Y}$ to the original field (Y) for each point of the spatio-temporal domain,

Equation 2.3: $$Y'(ns,nm) = Y(ns,nm) - \bar{Y}(ns)$$

The covariance matrix is defined to calculate all possible relations among models between pairs of points in the Hovmöller (Eq. 2.4):

Equation 2.4: $$C(ns,nm) = \frac{1}{n}\sum_{nm} Y'(ns,nm) * Y'(ns,nm)^T$$

In order to have a reduced number of relationships, the covariance matrix is diagonalized, verifying Eq. 2.5:

Equation 2.5: $$C * E = L * E,$$

The columns of the matrix E contain the eigenvectors $e^k(ns)$ (EOFs) of the covariance matrix and the elements of the diagonal of the matrix L constitute the eigenvalues λ_k of C, being k the number of modes. The eigenvalues give a measure of the variance explained by each pattern (North, 1984).

These EOFs represent the directions of maximum variability of the total field. Considering a number of K modes, the original field Y can be reconstructed as a linear combination of the orthogonal spatio-temporal patterns e^K (or EOFS) and their associated coefficients α_k (or PCs).

The principal components α_k (PCs) are obtained by projecting their

associated eigenvectors e^k (EOFs) over the initial anomalous field Y'. For each mode (k):

Equation 2.6: $$\alpha_k(nm) = Y'(ns, nm) * e(ns)^k$$

For Gaussian distributions of Y', the total variance of the field Y' can be decomposed as independent contributions of the EOFs, with each k mode explaining a fraction of the total variance given by the expression,

Equation 2.6: $$fvar_k = [\frac{\lambda_k}{\sum_{k=1}^{K} \lambda_k}] * 100$$

where λ_k is the eigenvalue of each mode.

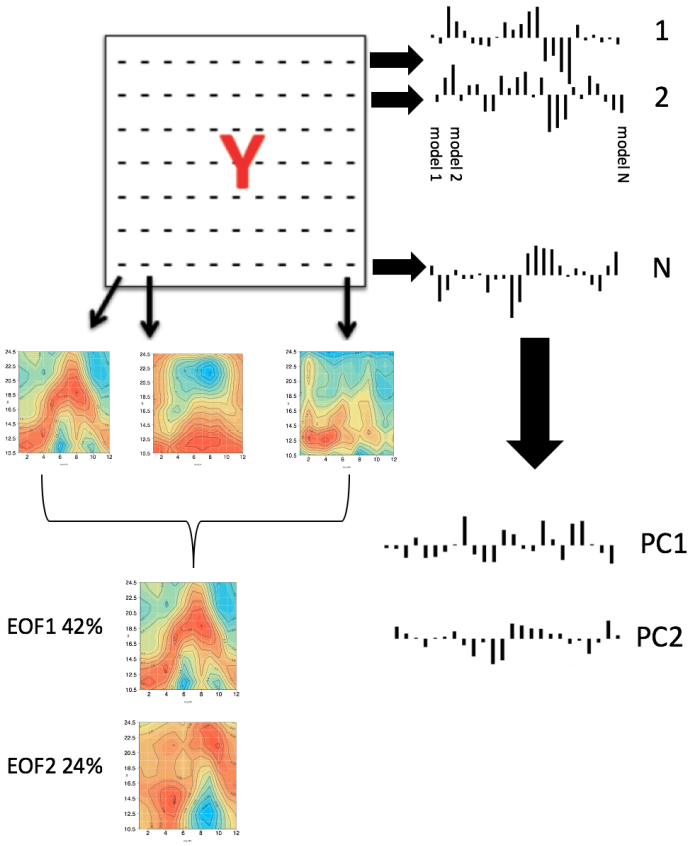

Figure 2.3: *Schematic of the Empirical Orthogonal Function Analysis applying to nm (number of models) Hovmöllers of dimension ns. Adapted from Rodríguez-Fonseca (2001).*

2.3.3.2 Intermodel correlations

Data employed in this thesis is generally in the form of monthly climatologies. They have been used in order to study the seasonal cycle of each model and make intermodel comparisons between variables. To evaluate relationships among variables, intermodel correlations have been performed using the 24 climatological annual values (one per model) as "time" series. Positive correlations mean that models with high values for a variable show high values

in the other variable as well. The use of intermodel correlations follows the methodology used in other intercomparison exercises done with CMIP5 models (Flato et al., 2013; Wang et al., 2014; Li et al., 2015; Deppenmeier et al., 2016; Mohino et al., 2019). In Chapter 3, monthly data are used to perform intramodel correlations between two variables. In this case, two series of monthly values of both variables are correlated with each other.

In this thesis, correlation maps are one of the main ways of visualizing results. They are used to show the abovementioned intermodel correlations, but also to present the relation between intermodel EOFs and the variables in question. In this case, the correlations are computed between the expansion coefficients α_k (being *k* the number of mode of the associated EOF) and the variables of interest (in our case, SST, SLP, precipitation or incoming surface radiation).

Statistical significance

The statistical significance level of the correlation coefficient *r* between any series of X and Y data of N elements each, has been stablished according to the statistical distribution of the *r* parameter. The parameter used depends on the size (N) of X and Y and is:

- For N<100, $t = \frac{r}{\sqrt{1-r^2}}\sqrt{N-2}$
- For N>100, $z = \frac{r}{1-r^2}\sqrt{N}$

The null hypothesis is that X and Y are linearly independent among them, therefore for N<100 t follows a Student distribution of N-2 degrees of freedom. For N>100, z follows a Gaussian distribution with mean = 0 and standard deviation = 1. If the value of the statistic z or t is greater than the corresponding with a significance level α, the correlation will be significant with a confidence level of 100(1-α). In this thesis all significance levels are taken to be 95% except in some cases (which are noted) for which 90% was used.

Results

3 Revisiting the CMIP5 thermocline in the Atlantic and Pacific Oceans

3 Revisiting the CMIP5 Thermocline in the Equatorial Pacific and Atlantic Oceans

The main results shown in this chapter are published in Castaño-Tierno et al., (2018).

The thermocline is defined as the ocean layer for which the vertical thermal gradient is maximum. In the equatorial ocean, observations lead to the use of the 20°C isotherm depth (z20) as an estimate of the thermocline depth. Nevertheless, this use is due to the proximity of z20 to the isotherm where maximum gradient occurs, a feature that does not have to be valid for models. This study compares z20 against the physical thermocline in the Equatorial Atlantic and Pacific Oceans, using SODA reanalysis and CMIP5 Pre-Industrial Control simulations. A summary of the data and methods used in this chapter can be found Schematic 3.1, and a more in-depth explanation is found in Chapter 2. In this chapter it is shown that z20 in models is systematically deeper and flatter than the thermocline and does not respond correctly to surface wind stress variations. It is also shown that the seasonal cycle of z20 shows smaller amplitude than that of the physical thermocline. This happens in both equatorial basins and suggests that z20 does not react to the same mechanisms as the thermocline. This could have important consequences in the assessment of air-sea coupling in current GCMs and bias reduction strategies.

RQ3.1: Is the 20ºC isotherm a good estimate of the equatorial thermocline?

RQ3.2: What are the consequences of using the physical definition of the thermocline and the 20ºC isotherm?

This chapter is structured as follows: first, the mean and seasonal variability of the equatorial Pacific thermocline and of z20 are analyzed both for SODA and CMIP5. Then, the relation between the depth of z20 and the thermocline and SST is explored for the two regions selected in the Pacific Ocean. The atmosphere-ocean coupling is further explored by establishing the

mechanisms by which the wind stress affects the position of the thermocline and of z20. The whole analysis is repeated for the Atlantic Ocean. Another section is devoted to the intramodel relationship between z20 and thermocline depth. Lastly, the results are discussed.

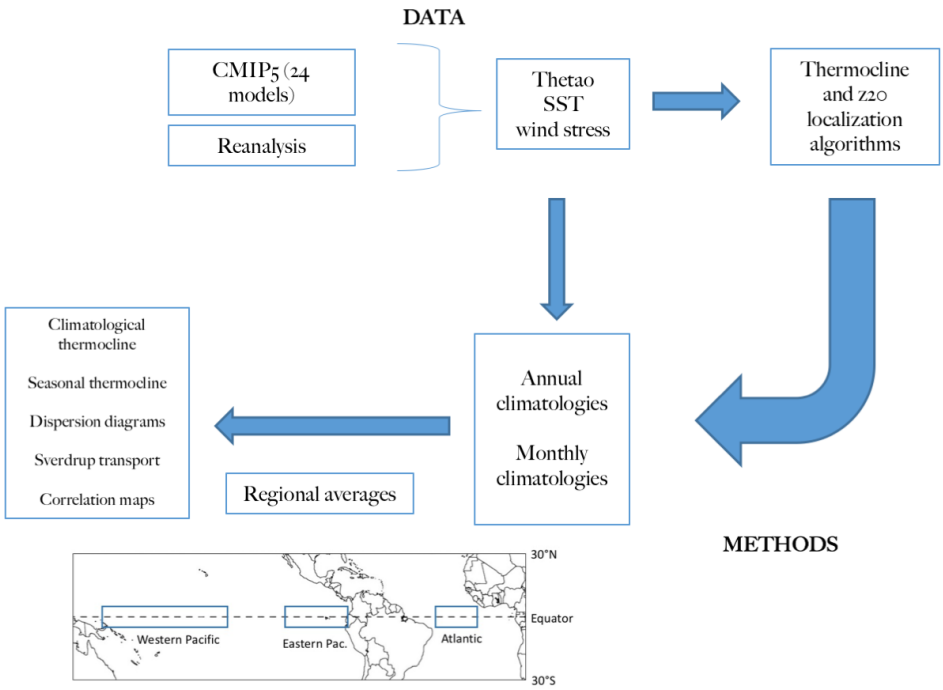

***Figure 3.1**: Summary of the data and methods used in this chapter. Variables of interest (thetao, SST, wind stress) are obtained from CMIP5 and SODA data. The thermocline and z20 are located using the methods described in Chapter 2 and then annual and monthly climatologies computed for all variables. They are then averaged on the three regions of interest. Dispersion diagrams (SST-z20 and SST-thermocline depth) are computed on those regions, and zonal wind stress and Sverdrup transport relation with thermocline depth/z20 is computed in the Atlantic and the Western Pacific boxes. More details on datasets and methods can be found in Chapter 2.*

3.1 Equatorial Pacific thermocline

The physical thermocline (given by the maximum gradient) tends to be shallower than z20, both for SODA and for CMIP5 models in the Pacific basin, especially in the east and west (Figure 3.2). The difference between both methods is bigger for the model mean than for the reanalysis (Fig. 3.2a). The thermocline and z20 values of the locations where there is TAO buoy data are generally shallower than both models and SODA reanalysis, but z20 is still systematically deeper than the thermocline.

Although the absolute differences between z20 and the depth of the thermocline are similar in the eastern and western equatorial Pacific, the relative differences are higher for the east (6.1% and 17% for SODA and CMIP5, respectively) than for west (3.5% and 6% for SODA and CMIP5, respectively). Such differences increase when the seasonal cycle is taken into account: for the eastern region, the relative difference between both measurements reaches 26% in CMIP5 ensemble mean for the March-April-May (MAM) period (Fig. 3.2c).

The seasonal cycle of the thermocline depth in CMIP5 models is similar to the observed one (Fig. 3.2b and 2c). This, however, is not the case for z20 in the eastern Pacific (Fig. 3.2c): z20 in SODA shows much smaller month-to-month variations than in CMIP5. This feature can be explained by the deeper location of z20 and, thus, less interaction with the atmosphere and radiative forcings, which makes the thermocline less reactive to the seasonal variability of the atmosphere. Differences between both methods in some individual models are greater than that of the ensemble mean as will be shown in the following sections.

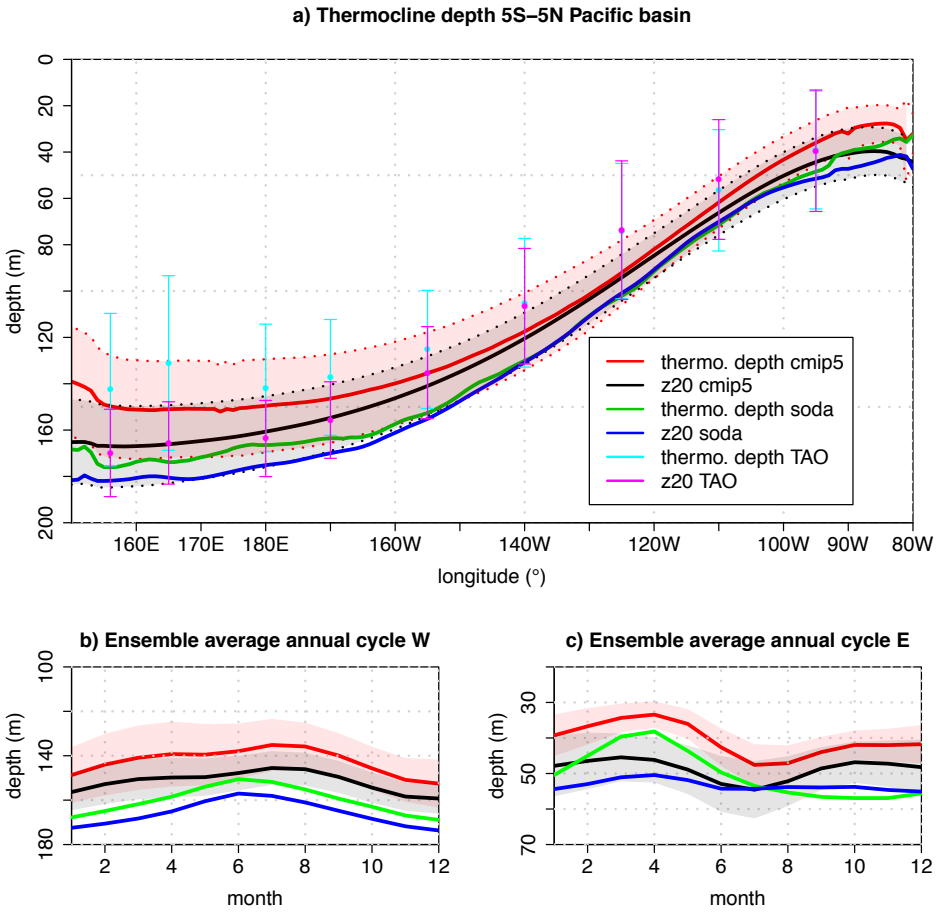

Figure 3.2: *a) Averaged (5°S-5°N) mean depth for the Pacific of SODA thermocline (green), CMIP5-ensemble thermocline (red), SODA z20 (blue) and CMIP5-ensemble z20 (black). Colored area shows model spread (+/-1 SD) for CMIP5 members. Climatological average of equatorial (0°N) thermocline (light blue) and z20 (pink) for TAO buoys is showed in points with uncertainty in bars (+/- 1 SD). b) Averaged (5°S-5°N) monthly-mean depth for the western Pacific of SODA thermocline (green), CMIP5-ensemble thermocline (red), SODA z20 (blue) and CMIP5-ensemble z20 (black). Colored area shows interannual variability for CMIP5 members. c) Same as 1b but for eastern basin.*

3.1.1 Relation between thermocline and SST bias

We further focus on the local relation between the SST and the depth of the thermocline in order to better understand what drives the differences in both methods for the ensemble of models. SSTs characterize the interface between ocean and atmosphere, providing an indication of the heat content of the upper layer of the ocean. Since biases in SST can either have thermodynamic or dynamical origins (Li et al., 2016), understanding the thermocline's relation with SST bias is crucial.

In the eastern Pacific the inter-model local correlation between z20 and SST is statistically significant, while there is no significant correlation between the thermocline depth and SST (Fig. 3.3a). This is clearer in Figures 3. 3c and 3.3e, where the scatter plots of SST biases[2] versus the thermocline depth and z20 in the eastern Pacific are shown. The positive correlation found between z20 and SST biases in the eastern part of the basin can be understood as a local response due to the shallowness of this isotherm in this region: the depth of a given isotherm depends on the number of isotherms above it, and so a model with a warmer SST will have a deeper 20°C isotherm. Moreover, the correlation between z20 and depth of the thermocline in this region is non-significant, reinforcing that z20 is not a good estimate of the thermocline depth for the eastern Pacific. These results suggest that the use of z20 to estimate the thermocline depth should be avoided in the eastern equatorial Pacific and that conclusions drawn when using it should be revised (e. g. Li et al., 2016), because our results suggest there is no link between the SST biases and those of the thermocline depth in this region.

[2] It must be noted that in this chapter "SST" and "SST bias" are used indistinctly when referring to intermodel variability and correlations, since they characterize in the same way each model SSTs in relation with the rest of the models. In the correlations the mean is removed, so the constant term that are the observations disappears.

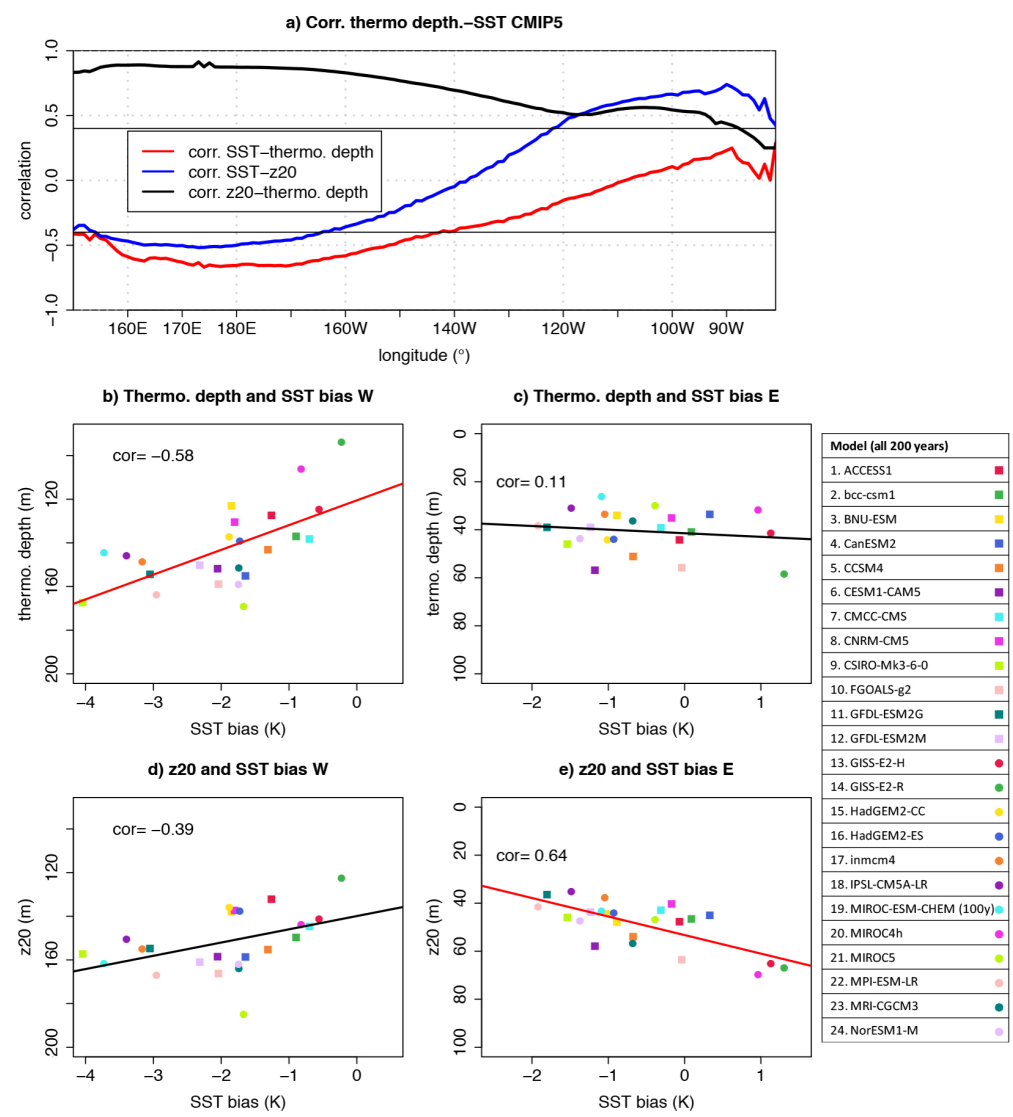

Figure 3.3: *a) Intermodel correlation between thermocline depth and SST bias (red) and z20 and SST (blue) for CMIP5 models in the equatorial (5°S-5°N) Pacific. Black line shows z20-thermocline depth correlation. Black horizontal lines show values over/under which correlation is significant. b) Scatter plot and linear fit between SST bias and thermocline depth in the equatorial western Pacific (averaged between 160°E-140°W) for CMIP5 models. c) Same as Fig. 3.2b but for eastern Pacific (averaged between 100°W-80°W). d) Scatter plot and linear fit between SST bias and*

z20 in the equatorial western Pacific (averaged between 160°E-140°W) for CMIP5 models. e) Same as Fig. 3.2d but for eastern Pacific.

Conversely, both estimates show very strong and significant correlation between them over the western equatorial Pacific (Figure 3.3a, black line). Both also show a local negative correlation with SST, although it is barely significant for z20 (Figure 3.3a, b and d). In this region, where mean model biases are cold (Wang et al., 2014, Fig. 1.8 in Chapter I, Introduction), our results suggest that cooler models have deeper thermoclines, a result that, at first order is not intuitive. In order to further understand this relation, we analyze how the zonal wind stress interacts with the depth of the maximum gradient and z20. This is achieved by assessing the local effects of zonal wind (Fig. 3.5a) and the remote effects of both zonal and meridional winds (Fig. 3.5b and 3.5c). Local correlation between the equatorial zonal wind stress and the thermocline depth (Figure 3.5a, red line) suggests that models with stronger easterly winds at the Equator have deeper thermoclines. Conversely, such link is underestimated when using z20 (Figure 3.5a, blue line). In turn, regarding SSTs in the central and western part of the basin, a positive correlation with the zonal wind stress is found (Figure 3.5a, black line), suggesting that colder SSTs are connected to stronger easterly winds. Three different mechanisms could be involved in the SST-wind-thermocline relationship. First, stronger easterlies would pile the warm water to the west deepening the thermocline there, but producing a local cooling of the SSTs due to thermodynamic processes. Second, such cooling of the ocean's surface would increase its density, which could, in turn, lead to increased vertical instability and mixing and a further deepening of the thermocline. This mechanism could be helped by local stirring, due to the kinetic energy transferred by local wind stress to the underlying sub-surface of the ocean. Third, and focusing on Figures 3.5b and 3.5c, off equatorial winds could also influence the thermocline, through anomalous Sverdrup meridional transport, as shown in Chapter 1. Recovering Eq. 1.7, Sverdrup mass transport V is given by:

$$V_y \approx -\frac{1}{ß}\frac{\partial T_x}{\partial y}$$

with ß = $\frac{2\Omega cos\varphi}{R}$, being R the Earth's radius and Ω the rotation rate of the Earth (Ω = 7.2921 × 10^{-5} rad/s).

In the climatology, the increase of easterlies from the Equator poleward up to 10°-15° drives a Sverdrup mass transport out of the Equator (Fig. 3.4b). However, the anomalous zonal wind stress pattern in Figure 3.5b shows maximum easterlies at the Equator and weaker anomalies poleward (consistent with Fig. 3.4a). Figures 3.5b and 3.5c show in grey the correlation between zonal wind stress and thermocline depth, while red (blue) means positive (negative) correlation between Sverdrup transport and thermocline depth. The associated equatorward anomalous Sverdrup is, therefore, consistent with a deeper thermocline. This suggests that models showing a weaker (stronger) latitudinal gradient of zonal wind tend to show a deeper (shallower) thermocline. The whole mechanism is visible for the thermocline depth, with grey shading over the whole index box and strong positive correlation with extraequatorial Sverdrup transport on the Southern Hemisphere (Fig. 3.5b), while for z20 (Fig. 3.5c) only the remote effects are apparent and not the zonal equatorial piling of water (lack of grey inside index box, which means that the piling of water in the index region due to easterly zonal wind does not contribute to increased values of z20).

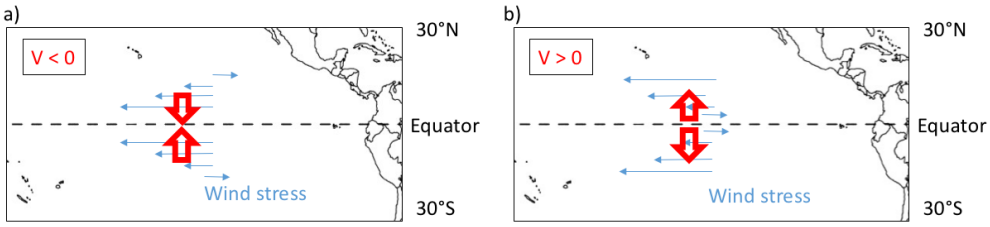

Figure 3.4: *a) Scheme of the Sverdrup transport in and out of the Equator. The climatological mechanism is that on the right: V is greater than 0, therefore the transport occurs toward the poles.*

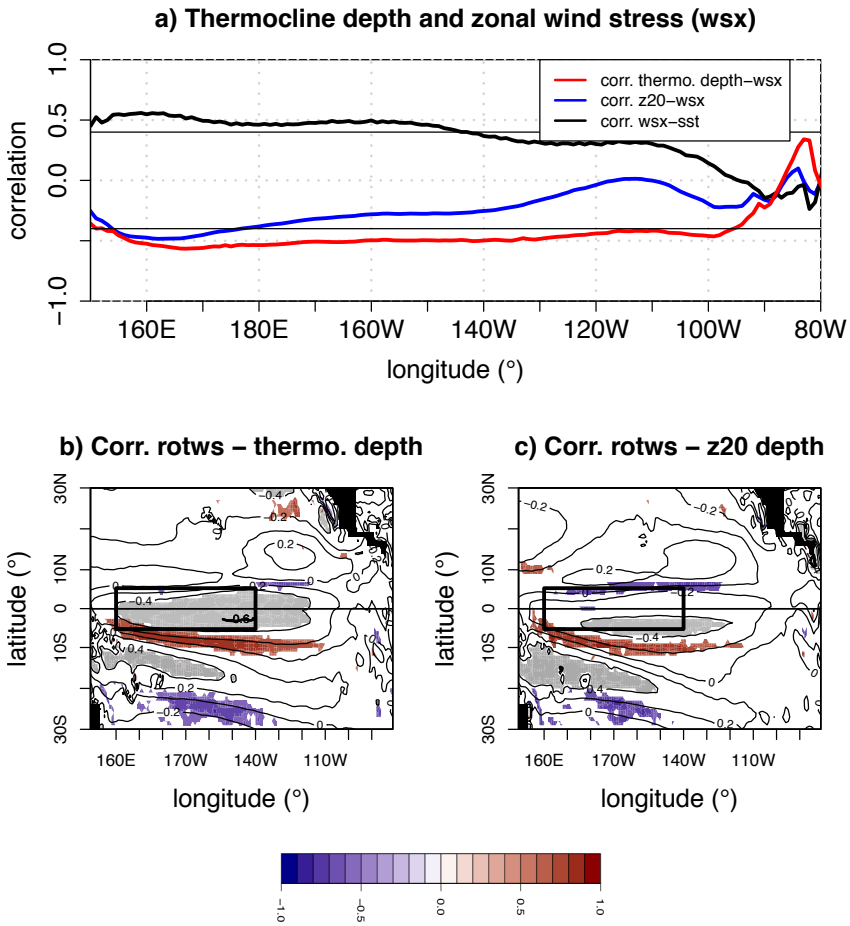

Figure 3.5: *a) Intermodel local correlation between thermocline depth-zonal wind stress (red) and between z20-zonal wind stress (blue) for CMIP5 models in the equatorial (5°S-5°N) Pacific. Black line shows correlation between zonal wind stress - SST correlation. Negative correlation means that those models with stronger easterly winds have deeper thermoclines. b) Correlation map (in contours) between zonal wind stress and thermocline depth index, calculated as the average between 5° S-5°N and 160°E-140°W. Areas of significant correlation at the 95% value are shaded. Colored shading highlight areas where correlation between the wind stress curl (Sverdrup transport) and the thermocline depth index is significant. Positive means northward Sverdrup mass transport. c) Same as Figure 3.3b but using z20 instead of the thermocline depth.*

3.2 Equatorial Atlantic thermocline

In the equatorial Atlantic, z20 is much deeper than the thermocline in the eastern part of the basin, both for CMIP5 models and reanalysis (Figure 3.6a), and its slope is much smaller than that of the thermocline. The seasonal cycle of the thermocline in CMIP5, which shows minimum depth in May and maximum depth in September, is more similar to the reanalysis (minimum in May and maximum in December) than that of z20 (Fig. 3.6b). z20 seasonal cycle is once again too weak, and almost flat in some models (Figs. 3.6b, 3.7 and 3.8), although the mean depth bias is smaller for z20 than for the thermocline depth.

While z20 is not locally significantly related to model SST in any point of the basin, the depth of the thermocline shows a moderate correlation in the east, where SST-z20 relation is the weakest (Figure 3.6c). Consistently with previous findings in the Pacific, in the equatorial Atlantic the thermocline depth shows a much stronger local correlation with zonal wind than the one shown by z20 (Figure 3.6d). We posit that these differences are due to z20 being much deeper than the thermocline, and thus less reactive to changes in surface temperatures and zonal winds in the equatorial region.

The off-equatorial anomalous wind stress pattern related to a deeper thermocline suggests an anomalous equatorward Sverdrup mass transport (Fig. 3.6e and 3.5f), consistent with the results found for the equatorial Pacific. Regarding z20, the wind stress pattern shows very strong loads in the subtropics, indicating a strong influence of the subtropical anticyclones and very little impact of local equatorial zonal wind stress. These results hold when using another isotherm, such as z23, instead of z20, suggesting that even when the isotherm bias is smaller (z23 mean position is more similar to the thermocline position), it is still not able to fully capture coupled atmosphere-ocean dynamics. The thermocline depth, however, is much more affected by local zonal winds and slightly less by the subtropical anticyclones. This result could have a strong impact when evaluating the heat budget terms and feedbacks in the tropical Atlantic, in which a discussion is still open regarding the role of Bjerkness feeddback and advective feedbacks in the tropical

Atlantic seasonal cycle and variability (Nnamchi et al., Martin-Rey 2018, Lübbecke et al., 2018).

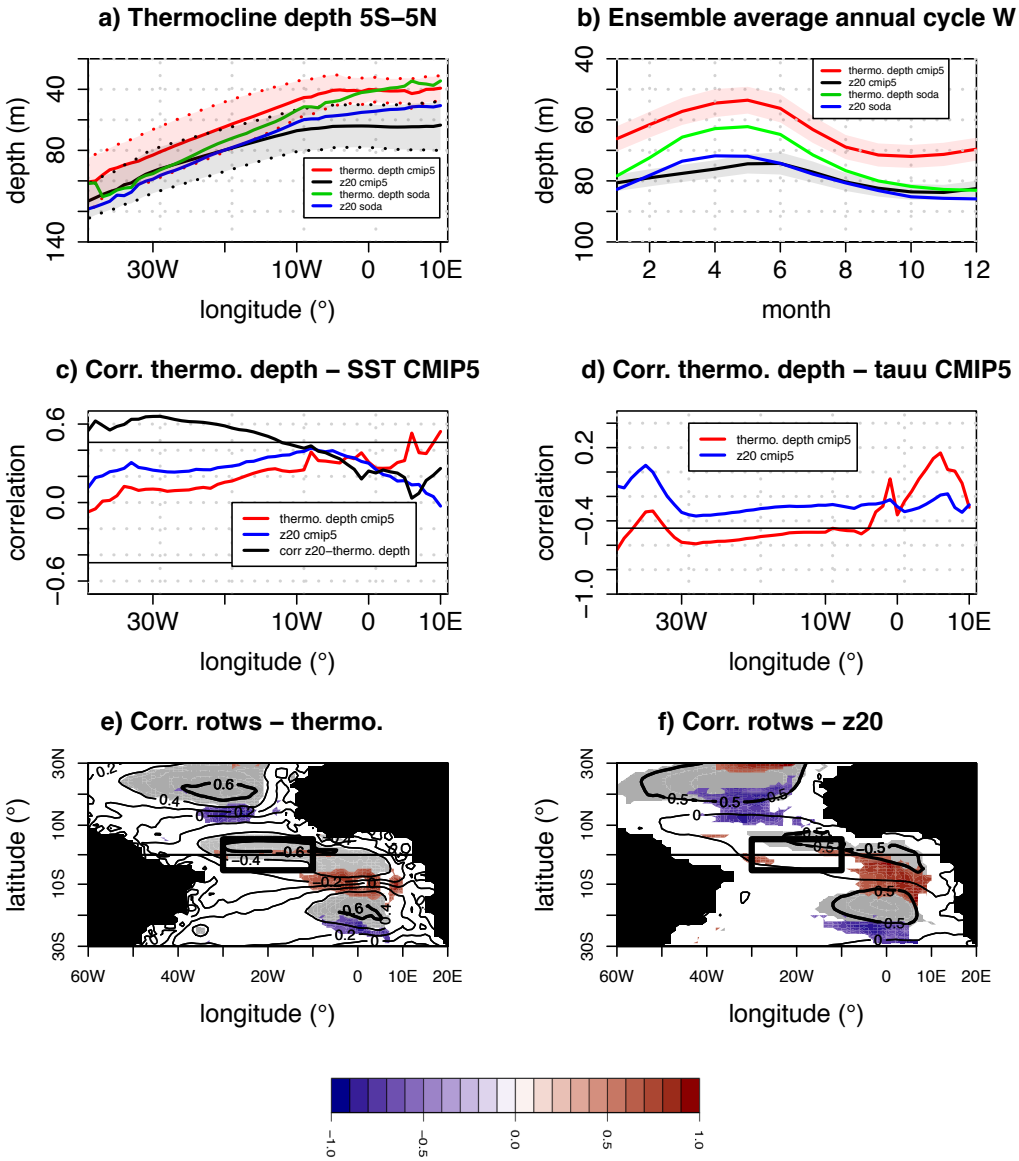

Figure 3.6: a) *Averaged (5°S-5°N) mean depth for the Atlantic basin of SODA thermocline (green), CMIP5-ensemble thermocline (red), SODA z20 (blue) and CMIP5-ensemble z20 (black). Dotted lines show intermodel spread (+/-1 SD). b) Averaged (5°S-5°N) monthly mean depth for the central Atlantic (30°W-10°W) basin of SODA thermocline (green), CMIP5 ensemble thermocline (red), SODA z20 (blue) and CMIP5 ensemble z20 (black). Colored area shows interannual variability for CMIP5 members. c) Intermodel local correlation between thermocline depth and SST (red) and z20 and SST (blue) for CMIP5 models in the equatorial (5°S-5°N) Atlantic basin. Black line shows correlation between z20 and thermocline depth. Black horizontal lines show values over/under which correlation is significant. d) Intermodel local correlation between thermocline depth and zonal wind stress (red) and z20 and zonal wind stress (blue) for CMIP5 models in the equatorial (5°S-5°N) Atlantic basin. Black horizontal lines show values over/under which correlation is significant. e) Correlation map (in contours) between zonal wind stress and thermocline depth index, calculated as the average between 5S-5°N and 30°W-10°W. Areas significant at the 95% value are shaded. Colored areas show the regions in which the correlation between the wind stress curl (Sverdrup transport) and the thermocline depth index is significant. f) Same as Fig. 3.4e but for z20-zonal wind stress correlation.*

3.3 Analysis of intra-model monthly cycle of 20°C isotherm depth (z20) and thermocline depth

In order to reinforce the robustness of the results from the multimodel study, intramodel comparisons have been performed so that the origin and consequences of the differences between z20 and thermocline depth are more clear. Climatological monthly means have been computed for each region (Western Pacific, Eastern Pacific and Atlantic indexes) and are shown in Figures 3.7, 3.8 and 3.9. These figures are computed using 200 years of monthly data for each model (except for the MIROC-ESM-CHEM model, which only had 100 years available) and computing the mean and standard deviation for each month.

As seen in Figure 3.2b, the seasonal cycle of z20 and thermocline depth in the Western Pacific are very similar, although there is a systematic bias: z20 ensemble mean is deeper than thermocline depth for all months, and most

individual models. There are some models (GFDL-ESM2G, MPI-ESM-LR, NorESM1-M and both HadGEM2) that show very little bias, and even one model (CSIRO-Mk3-6-0, which is known to be especially cold, Gordon et al., 2010; Hourdin et al., 2015) that has a deeper thermocline than its z20 counterpart. However, in four out of the 24 models (GISS-E2-R, MIROC4h, MIROC5 and MIROC-ESM-CHEM) there is a strong bias, with z20 up to 60 meters deeper than the thermocline in MIROC models (40 in GISS-E2-R). The seasonal cycle is also more pronounced in most models for the thermocline depth (Table 3.1). Most models represent correctly the seasonal cycle, although there are some (ACCESS1, BNU, MRI) which have an inverted seasonal cycle. Regarding interannual variability, it is higher for the thermocline depth than for z20 in 22 out of 24 models.

Interannual correlations between both methods, however, are generally very high and significant for almost all models and months. An exception is made for GISS-E2-H, which shows a low correlation throughout the whole year and CESM-CAM5, GFDL-ESM2G and the MIROC models, which have a dip in correlation during boreal autumn.

	Western	Pacific	Eastern	Pacific	Atlantic	
	z20 (m)	**thermo. (m)**	**z20 (m)**	**thermo. (m)**	**z20 (m)**	**thermo (m)**
ACCESS1	15.2	*21.77*	*10.04*	15.17	11.6	20.55
bcc-csm1	*22.27*	*30.57*	*7.45*	8.62	8.52	15.82
BNU-ESM	*17.16*	*20.71*	*14.78*	6.65	9.17	20.24
CanESM2	*23.66*	*32.9*	*18.16*	*20.34*	10.59	*28.67*
CCSM4	12.44	*14.43*	*14.88*	*21.07*	*15.14*	*28.4*
CESM1-CAM5	*21.56*	*26.9*	*16.33*	*23.38*	*22.67*	*37.61*
CMCC-CMS	*20.45*	*26.89*	*9.15*	14.32	13.88	*25.94*
CNRM-CM5	*20.92*	*24.8*	*7.35*	13.07	*21.45*	*29.94*
CSIRO-Mk3-6-0	9.94	13.8	*16.22*	*24.91*	7.89	18.17
FGOALS-g2	*21.14*	*23.54*	*30.94*	*37.7*	*15.63*	*23.41*
GFDL-ESM2G	*16.36*	*21.29*	*16.31*	13.09	*21.2*	*28.67*
GFDL-ESM2M	15.28	*19.07*	*6.97*	10.73	*20.77*	*27.21*
GISS-E2-H	12.57	18.9	*11.59*	10.12	5.72	10.72
GISS-E2-R	14.62	7.09	*7.79*	15.58	1.98	3.17
HadGEM2-CC	*25.31*	*29.2*	*20.78*	*27.41*	*22.64*	*31.74*
HadGEM2-ES	*23.18*	*27.31*	*21.82*	*27.66*	*20.66*	*29.72*
inmcm4	11.4	*25.75*	*13.93*	14.48	5.87	15.02
IPSL-CM5A-LR	16.1	*19.6*	*6.25*	14.66	9.27	*36.16*
MIROC-ESM-CHEM	*23.49*	*30.27*	*34.09*	15.05	9.08	*36.15*
MIROC4h	*28.69*	*48.22*	*35.14*	*20.64*	*17.44*	*44.91*
MIROC5	*21.53*	*33.75*	*32.69*	*23.37*	7.45	*21.22*
MPI-ESM-LR	*20.35*	*22.66*	*22.85*	*20.32*	13.73	14.62
MRI-CGCM3	*18.67*	*32.32*	*28.29*	*25.1*	9.14	*26.95*
NorESM1-M	16.06	18.19	*9.83*	12.2	*16.33*	*27.77*
SODA	16.63	18.37	4.66	18.75	14.1	20.85

Table 3.1: *Seasonal cycle (difference between the months with the shallowest thermocline and the deepest one, in meters) for each method and each of the models and SODA, in the three regions considered. Values in italics are those which are bigger than the corresponding SODA values.*

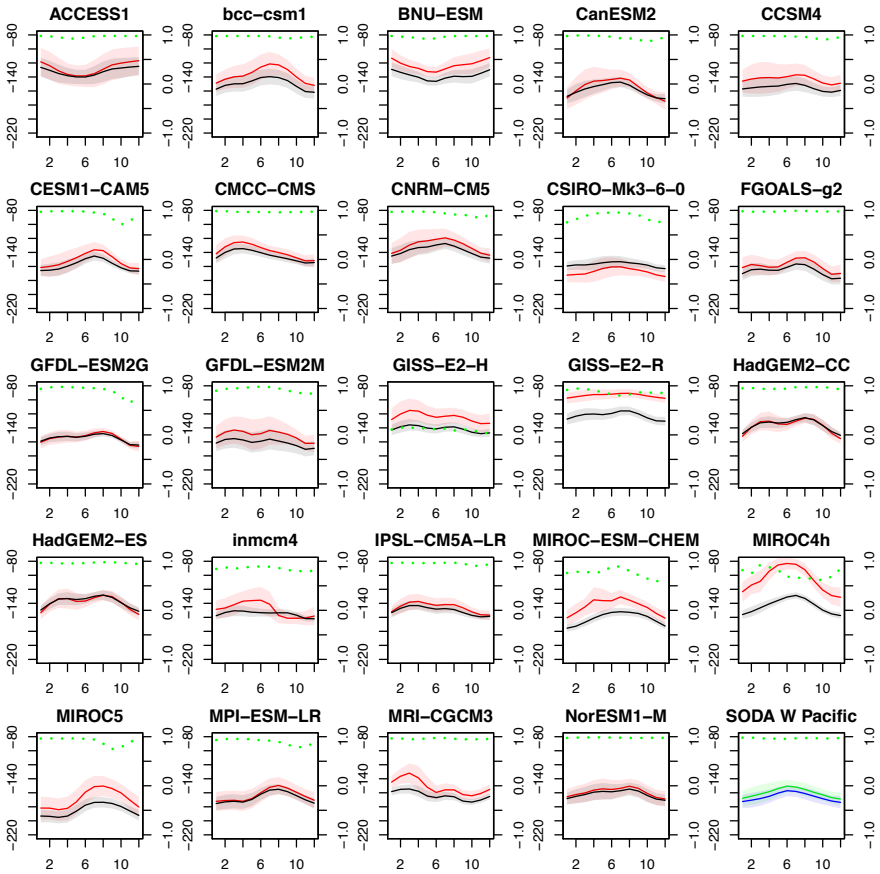

Figure 3.7: *Monthly mean values for thermocline depth (red) and z20 (black) for the 24 CMIP5 models in the western Pacific equatorial region. Green dotted line shows correlation between both methods. Right axis shows correlation values. Lower right corner panel shows seasonal cycle for SODA reanalysis (green line for thermocline depth and blue line for z20). Colored areas show interannual variability (+/- 1 SD).*

The seasonal cycle of the ensemble mean in the Eastern Pacific (Fig. 3.2c) is less marked for z20 than it is for the thermocline depth (Table 3.2). Again, the positive difference in favor of the thermocline depth (it being generally shallower than z20) is obvious in most individual models, even more strongly than it was in the Western Pacific (Fig. 3.8). In the Eastern region, interannual variability is generally more pronounced for z20 than it is for thermocline

depth. The correlations between z20 and the thermocline are, in general, lower than for the Western Pacific. In half of the models (BNU, CanESM2, CCSM4, CESM1-CAM5, CMCC, CSIRO-Mk3-6-0, FGOALS, GISS-E2-R, both HadGEMs and MRI-CGCM3) there is a drop in correlation values during boreal spring. It is worth noting that these drops put the correlation under 0.7 in some cases, which means that z20 accounts for less than 50% of thermocline year-to-year depth variability. For some models, using z20 instead of the thermocline in the Eastern Pacific seems not advisable (GISS-E2-H, MIROC-ESM-CHEM, MIROC4h and MIROC5) as they might lead to wrong conclusions when addressing air-sea interactions in this area.

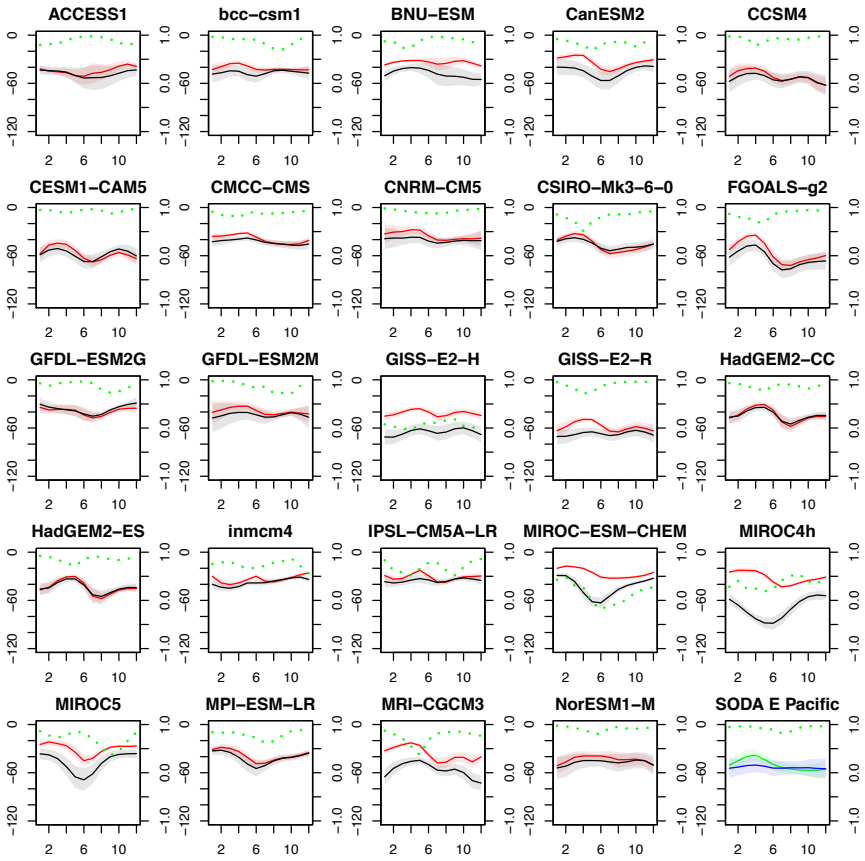

Figure 3.8: *Same as Fig. 3.7 but for the Eastern Pacific.*

Figure 3.9 shows the results for the 24 models in the Atlantic. Here, the seasonal cycle of z20 is far from being as well defined as that of the thermocline, which was very similar to SODA (Fig. 3.6b). Furthermore, the strong difference between methods leads to a lack of overlapping of the colored areas around z20 and the thermocline depth. In addition, the seasonal cycle of z20 is very weak for most models (some exceptions being CNRM-CM5 and both HadGEM2s), and the correlations between z20 and the thermocline depth are weak, especially in boreal summer. More than half the models present, in some months, relatively low correlations between z20 and the thermocline depth (under 0.5). These, although significant, explain less than 25% of the variability between both methods. Moreover, the magnitude of the interannual variability is underrepresented by z20 (shadings are generally smaller, Table 3). Such results call against the use of this estimate to evaluate the thermocline depth and its variability in the Equatorial Atlantic.

It must be concluded that the use of z20 to estimate the thermocline in CMIP5 models produces a systematic error in the climatological values, the seasonal cycle and the interannual variability, and that this error is present in all regions, although it is more relevant in the Eastern Pacific and the Atlantic Ocean.

The intramodel study also shows that the bias of the ensemble mean is smaller than that of some particular models, so that the effects of using the representative isotherm in single-model studies can be worse than expected from Figs. 3.2b, 3.2c and 3.5b. In addition, users of certain models (all three MIROCs, GISS-E2-H, CSIRO-Mk3-6-0 and MRI-CGCM3, in particular) should be exceptionally cautious when using z20, since there are seasons (for all three regions) in which it is not at all a good estimator of thermocline depth.

	Western	Pacific	Eastern	Pacific	Atlantic	
	z20 (m)	**thermo. (m)**	**z20 (m)**	**thermo. (m)**	**z20 (m)**	**thermo (m)**
ACCESS1	*25.76*	*38.44*	18.94	13.15	4.52	6
bcc-csm1	*21.15*	*29.03*	13.53	7.72	4.92	6.16
BNU-ESM	17.5	*22.59*	16.74	7.68	5.02	6.04
CanESM2	16.02	*28.41*	16.76	7.19	3.95	8.07
CCSM4	*20.86*	*32.67*	19.53	14.45	4.68	6.87
CESM1-CAM5	13.67	*21.97*	15.34	11.53	5.19	7.1
CMCC-CMS	12.54	17.91	9.32	6.37	6.57	8.85
CNRM-CM5	18.18	*26.72*	16.38	12.71	6.2	8.43
CSIRO-Mk3-6-0	13.98	*21.98*	11.45	9.25	6.46	*10.54*
FGOALS-g2	16.7	*23.01*	18.61	11.28	7.02	*9.54*
GFDL-ESM2G	10.34	13.9	11.06	11.28	5.72	7.42
GFDL-ESM2M	*25.56*	*34.13*	19.52	14.91	6.83	9.24
GISS-E2-H	13.51	*27.28*	16.51	8.33	4.6	6.47
GISS-E2-R	14.25	13.55	14.6	10.76	3.9	5.05
HadGEM2-CC	13.61	18.43	11.71	10.48	*10.5*	*14.26*
HadGEM2-ES	14.57	19.64	11.41	9.99	*9.29*	*12.52*
inmcm4	11.16	*26.8*	6.52	5.8	7.59	4.87
IPSL-CM5A-LR	11.38	18.02	9.33	6.87	3.92	6.73
MIROC-ESM-CHEM	10.83	*22.55*	8.06	3.85	4.15	6.28
MIROC4h	10.48	*22.77*	12.59	5.06	5.15	*9.81*
MIROC5	16.19	*30.59*	17.52	7.88	5.68	*9.87*
MPI-ESM-LR	16.56	*25.18*	12.19	8.08	6.64	7.41
MRI-CGCM3	11.35	20.12	14.13	9.52	5.93	*9.99*
NorESM1-M	*19.73*	*24.47*	*20.98*	*15.81*	5.4	*12.02*
SODA	17.68	20.31	20.16	15.04	8.86	9.3

Table 3.2: *year to year variability amplitude (mean value of shaded areas in Figs. 3.7b, 3.8 and 3.9) for each method and each of the models and SODA, in the three regions considered. Values in italics are those which are bigger than the corresponding SODA values.*

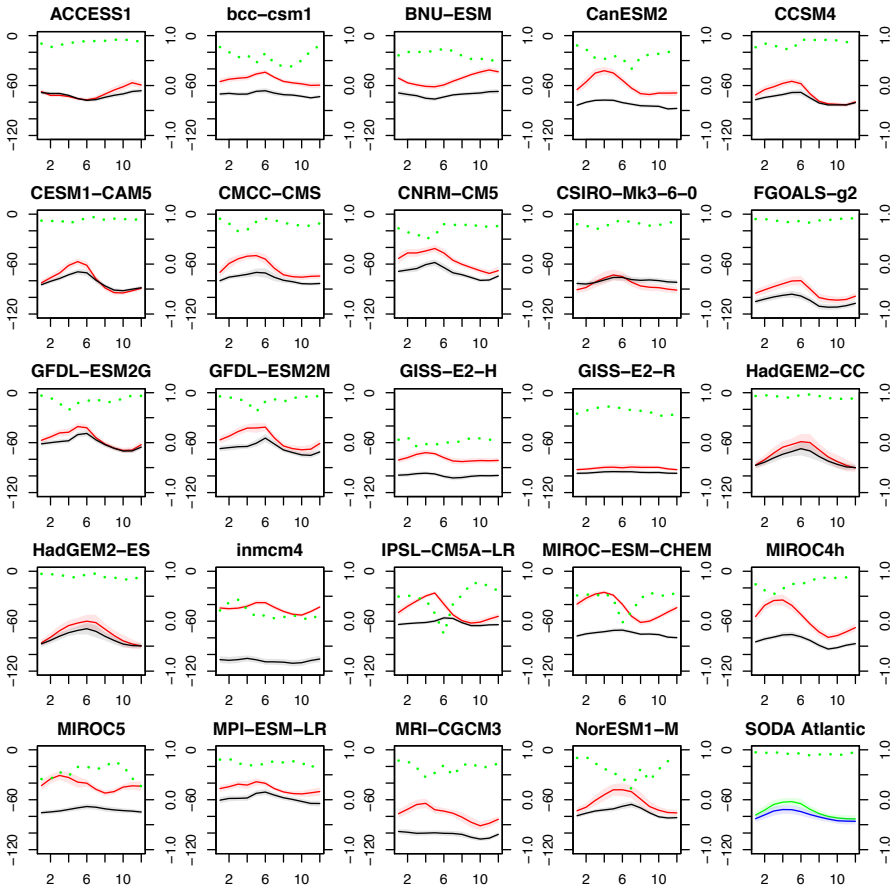

Figure 3.9: *Same as Fig. 3.7 but for the Atlantic Ocean.*

3.4 Discussion and conclusions

In the present work we address the use of z20 as an estimate of the thermocline depth in current state-of-the-art models. Although the reliability of z20 as a measure of the thermocline had been analyzed in observations (Fiedler, 2010), model reliability of this estimate had not been assessed so far, except for the work of Yang and Wang (2009) who showed that using z20 in future climate projection could lead to errors. Here we show for the first time that such an estimate is also biased when used to explain the basic dynamics of the atmosphere-ocean interactions, showing a lack of connection in the western equatorial Pacific, especially due to the part mediated by the wind stress.
It is also found that identifying z20 with SST in the eastern equatorial Pacific could lead to spurious conclusions. Regarding the eastern equatorial Pacific, our results further reinforce those from Li et al., (2015). They found that a too shallow thermocline in the eastern Pacific can be related with an excessive cold tongue in the central Pacific through ocean advection of colder waters. The even shallower thermocline in the east together with enhanced trades in the central Pacific (Li and Xie, 2014) provide a stronger upwelling and the development of a stronger cold tongue in models (Zheng et al., 2012).

In the western equatorial Pacific basin z20 is deeper than the thermocline so it is less affected by the surface winds, thus being less useful for understanding processes related to the action of the wind on the ocean surface. Our study shows that, even in the regions in which the climatology of z20 compares relatively well to the depth of the thermocline, the seasonal cycle is not well represented by this method. z20 seasonal cycle and year-to-year variability is weaker than thermocline depth's for the whole Pacific basin. This could have a great impact in variability and upwelling studies, for which a correct assessment of the depth of the thermocline is decisive (Richter, 2015). Moreover, the systematic error that z20 shows in the ensemble mean is smaller than that of some particular models. This calls for exercising great caution when using it in single model studies.

The difference in the eastern region of the Atlantic between z20 and the depth of the thermocline is even greater than in the Pacific Ocean. Moreover,

Voldoire et al., (2014) posited, for the CNRM model (included in our ensemble), that the thermocline (estimated as z20) is too shallow in the west and too deep in the east due to too weak easterlies. When considering this under the light of our results, it seems that the problem they detected is more serious than previously thought: the thermocline would be much shallower in the east and a bit deeper in the west when compared to the SODA thermocline, which makes the bias of the thermocline different from the z20 bias. This suggests that the reason for the too flat thermocline might lie in the lack of response of z20 to zonal equatorial winds. This highlights the need for using the right definition of thermocline depth, in order to further narrow the origin of model errors in this region.

Again, the seasonal cycle of z20 is too weak in the Atlantic, and some models show very little interannual variability. This effect is especially evident in the Northern Hemisphere spring months, in which the Atlantic Cold Tongue takes place, and could bear consequences on studies of that Atlantic feature. A recent paper of Cabos et al., (2017) put forward the important role of the south subtropical anticyclone and heat advection in explaining equatorial biases. They use as diagnostic z23, which our results suggest –it being a representative isotherm- is heavily influenced by both the southern and northern subtropical anticyclones and more sensitive to equatorward Sverdrup transport than the physical thermocline. Therefore, we should be cautious regarding the conclusions related to thermocline dynamics using this estimate. The present work provides evidence suggesting that the thermocline reacts more clearly to equatorial zonal winds in the center of the basin, while z20 is more affected by other factors, such as the northern anticyclone in the Atlantic.

Therefore, a correct definition of the thermocline depth is needed to avoid errors and incorrect conclusions in the assessment of model bias and variability and their ability to reproduce ocean-atmosphere interactions in the equatorial Pacific and Atlantic Oceans.

4 Representation of Northwest African upwelling in reanalysis and CMIP5 models

4 Representation of Northwest African upwelling in reanalysis and CMIP5 models

The Northwest Africa (NWA) upwelling region is located along the Senegalese and Mauritanian coast, between 10°N and 25°N and in a very narrow longitudinal band (Fig. 1.8).

In this region, most of the upwelled waters are due to Ekman pumping which, because of the strong meridional alongshore winds, can be simplified using Eq. 1.8. As a consequence, surface waters in this region are cold and rich in nutrients, becoming an area of great climatic and economic relevance (Alder and Sumaila, 2004).

The rapid increase in the upper ocean upwelling in this region along the 20th century (McGregor et al., 2007) and the contradictions found about future projections (Bakun, 1990; Barton et al., 2013; Wang et al., 2015; Sylla et al., 2019) put forward the need of better understanding model ability to simulate Ekman induced upwelling processes.

Although enhanced land–ocean differential heating due to greenhouse warming has been proposed to intensify coastal upwelling by strengthening alongshore winds, analyses of observations and previous climate models have provided little consensus on historical and projected trends in coastal upwelling (Mote and Mantua, 2002; Iles et al., 2012; Santos et al., 2012). Wang et al. (2015) have found an increase in upwelling intensity and duration at high latitudes, resulting in a substantial reduction of the existing latitudinal variation in coastal upwelling.

Even though there is a lack of reliability of simulated coastal upwelling, which can be at least in part attributed to problems in model resolutions (Small et al., 2015), large scale features associated with alongshore wind representation can provide important information.

Most of the previous CMIP5 studies regarding coastal upwelling are based in multimodel ensemble results. Nevertheless, intermodel variability should

be considered in order to better understand the causes of different responses and spread among models.

This chapter studies how reanalysis and CMIP5 models represent the seasonal cycle of Ekman-induced coastal upwelling, using wind stress data. Sea surface temperature and the thermocline calculated in the previous chapter are also used here to assess its impact on the subsurface. Also the intermodel variability of alongshore winds is analysed. To this aim, principal component analysis is performed in order to calculate the main modes of intermodel variability of climatological upwelling index, and their relations with large scale model features is discussed. A brief summary of the data and methods used in this chapter is shown in Figure 4.1, and a more complete explanation in Chapter 2.

The principal research questions addressed in this chapter are:

RQ4.1: How is NWA upwelling seasonal cycle simulated by CMIP5 models?

RQ4.2: Do models reproduce the observed local relation between upwelling, SSTs and thermocline depth and intensity?

RQ4.3: What are the large scale features controlling the different representation of NWA upwelling in climate models?

The chapter is structured as follows: first, the NWA upwelling is described both in reanalysis and in reanalysis. Then, the same analysis is performed for the CMIP5 24-model ensemble average. Empirical orthogonal functions are used to characterize the intermodel variability of the upwelling index, and the relationship of the first two variability modes with large-scale intermodel variability is studied. Results are discussed and summarized in the last two sections. The data and methods used in this chapter are summarized in Figure 4.1.

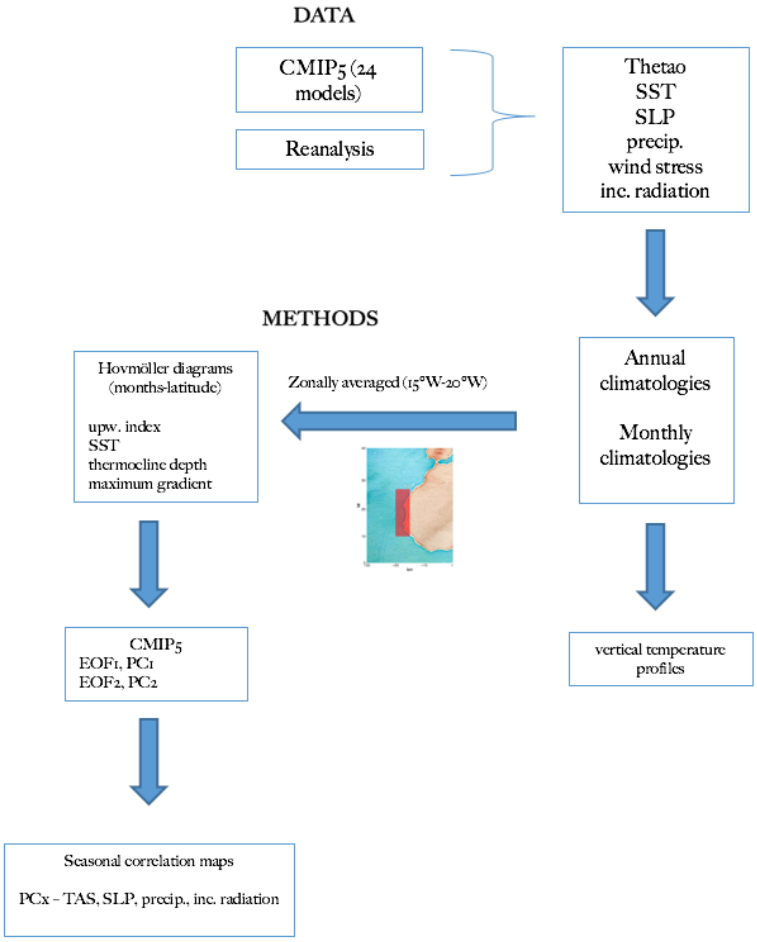

***Figure 4.1**: Summary of the data and methods used in this chapter. Monthly and annual climatologies are computed from variables obtained from CMIP5 and reanalysis datasets. Vertical temperature profiles are computed from monthly climatologies of potential temperature (thetao). Upwelling index is computed from meridional wind stress following Eq. 1.8, and thermocline depth and intensity are obtained from thetao. These three variables together with the SST are used to characterize the upwelling region, and are zonally averaged from 20°W to 15°W before being represented in a Hovmöller latitude-time diagram. From all 24 CMIP5 models Hovmöller diagrams the first EOFs are computed, and their corresponding PCs correlated with global fields of SST, SLP, precipitation and incoming solar radiation. More details on datasets and methods can be found in Chapter 2.*

4.1 Description of the NWA upwelling system in reanalysis and observations

Along this work Ekman-induced upwelling is calculated using meridional wind stress (Eq. 1.8). Nevertheless, the effectiveness of Ekman pumping in producing upwelling is closely related to the depth and strength of the thermocline, as vertical thermal stratification can prevent vertical movements bellow the thermocline

This chapter is focused on the Northwest African upwelling region, which has the particularity of being affected by the monsoon winds during boreal summer.

There are two differentiated zones within the NWA upwelling region: the seasonal upwelling region and the permanent upwelling region. The first is located in front of Cape Vert (around 15°N), and the second is at the Cape Blanc latitude, 21°N-23°N, (Mbaye et al., 2015; Benazzouz et al., 2014). Seasonal upwelling occurs during late boreal winter and early boreal spring (February to April), and moves northward along the year reaching the northern limit of the region in summer, as northerly winds strengthen in higher latitudes and weaken in lower latitudes, due to the appearance of monsoon winds (Barton 2013; Caniaux et al., 2011).

Observations present a different seasonal cycle of upwelling for the northern half (17°N to 24°N) than for the southern half of the region (10°N to 17°N) (Fig. 4.2a1). The northern half shows high upwelling index values for all seasons (although the maximum values are found during boreal spring), while the southern half shows a marked seasonal behaviour. In the latter region, during winter and spring there are high upwelling values, whilst during the monsoon season upwelling intensity decreases and even reverses its sign due to the change in wind direction during the monsoon. The West African Monsoon is characterized by a northward shift of the ITCZ north and low level southwesterly atmospheric flow between June and September, associated with heavy rains over West Africa.

Regarding sea surface temperature (SST, Fig. 4.2b1), a seasonal regime is also observed. The maximum temperatures occur in late summer for lower latitudes, while minimum SST appears, as expected, at the end of boreal winter for higher latitudes. It is important to note that, during spring, there is a minimum of temperatures that covers the whole latitude domain of the Hovmöller plot. That is, the SSTs in this region do not vary depending only on the seasonal and latitudinal variation of radiative forcing, but also on wind behaviour, as shown by the prevalence of upwelling and colder waters during the first half of the year, and weakened upwelling and warmer SST during the second half, with the upwelling maximum lading by two months the SST minimum in the region of seasonal upwelling (southern half of the domain). Thus, the impact of Ekman-induced upwelling due to alongshore meridional wind on surface temperature is direct and strong northerlies are associated with lower temperatures.

Figure 4.2: *Monthly evolution of the climatological Ekman induced upwelling and related variables along the coast. Left: Observations (upwelling and SST) and reanalysis (thermocline depth and max. grad.); center: multimodel ensemble; right: difference between multimodel ensemble and observations/reanalysis. First row: wind-based upwelling index as defined in Chapter 1 (N/m^2); second row: sea surface temperature (SST, °C); third row: thermocline depth (m); fourth row: thermal gradient at the thermocline level (K/m). Hovmöller plots are computed by zonally averaging the variables between 20°W and 15°W for each latitude, and then computing the climatological monthly means (see red box in Fig. 1.8)*

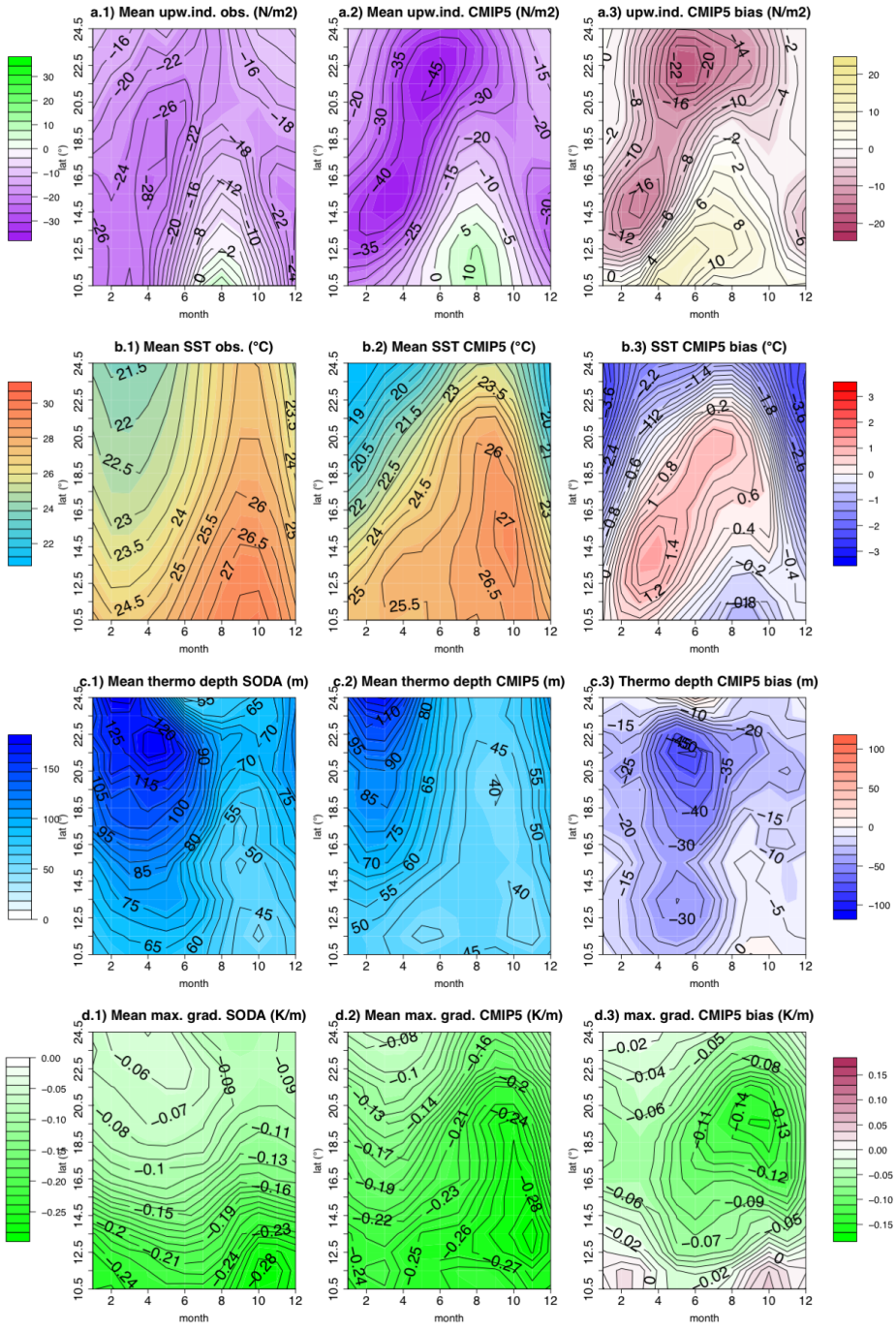
a.1) Mean upw.ind. obs. (N/m2)
a.2) Mean upw.ind. CMIP5 (N/m2)
a.3) upw.ind. CMIP5 bias (N/m2)
b.1) Mean SST obs. (°C)
b.2) Mean SST CMIP5 (°C)
b.3) SST CMIP5 bias (°C)
c.1) Mean thermo depth SODA (m)
c.2) Mean thermo depth CMIP5 (m)
c.3) Thermo depth CMIP5 bias (m)
d.1) Mean max. grad. SODA (K/m)
d.2) Mean max. grad. CMIP5 (K/m)
d.3) max. grad. CMIP5 bias (K/m)
month
lat (°)

The thermocline depth and associated intensity of the vertical gradient in SODA reanalysis (Fig. 4.2c1 and 4.2d1) also show a latitudinal and seasonal pattern, with deeper thermocline and weaker gradients during winter-spring in higher latitudes and a shallower thermocline but stronger in summer-autumn for lower latitudes. Comparing these figures with Fig. 4.2b1, it is apparent that cooler surface temperatures are related to a well-mixed water column while warmer SSTs occur when there is a thin mixed layer, well isolated from cold water from the deep ocean. This is supported by the vertical structure of the ocean, whose seasonal evolution is shown in Fig. 4.3 for the 15°N latitude. The thermocline is weaker for the months with upwelling (February to April), and stronger during summer-autumn. The temperature difference between the surface and a given depth (100 m) is also much stronger in summer than in spring (around 12°C for September vs 6°C in March). For the 23°N latitude, in the so-called permanent upwelling region, although there is still clear seasonality in the temperature profile (Figure 4.4), the values of the maximum vertical thermal gradient don't ever reach -0.1°C/m, which is considered to be the threshold for there being a well-formed thermocline (Fiedler, 2010) (Fig. 4.2d1). In this case, the mixing is so good during spring that there is a temperature difference of less than 1°C in the first 100 meters. Even during summer and autumn, when northerly winds are weaker and radiative warming of the surface more effective, the temperature change in the first 100 meters stays around 4 degrees.

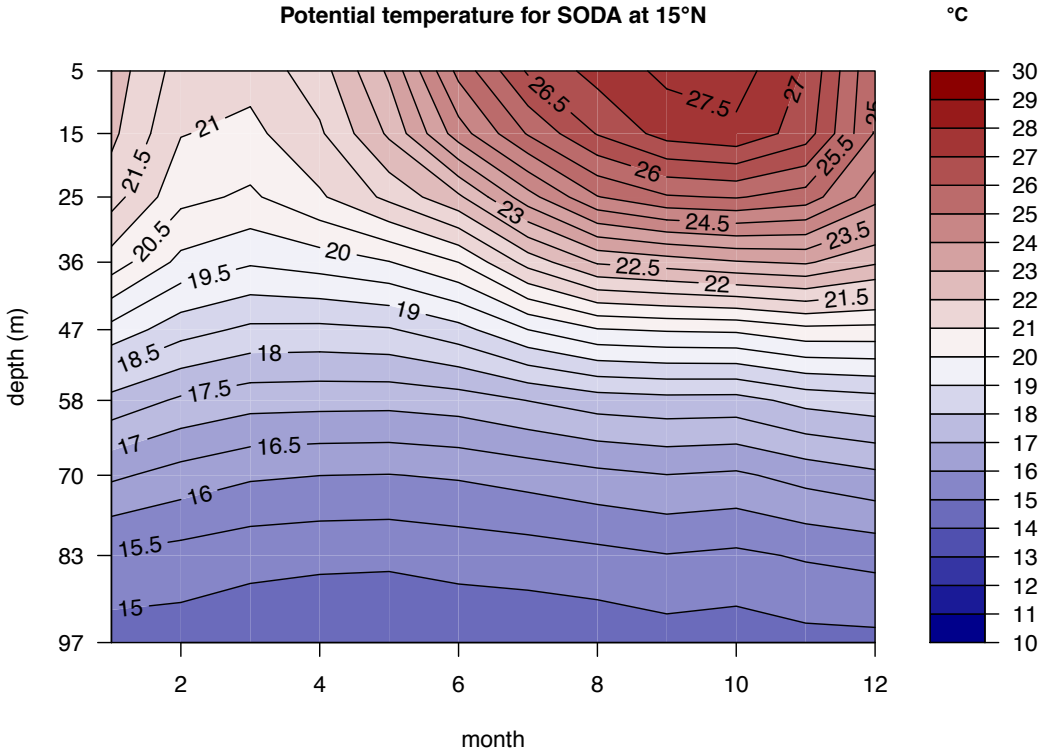

Figure 4.3: *Potential temperature (°C)* vertical *profile at 15°N for SODA (averaged from 20°W to 15°W). Only the first 97 meters are represented.*

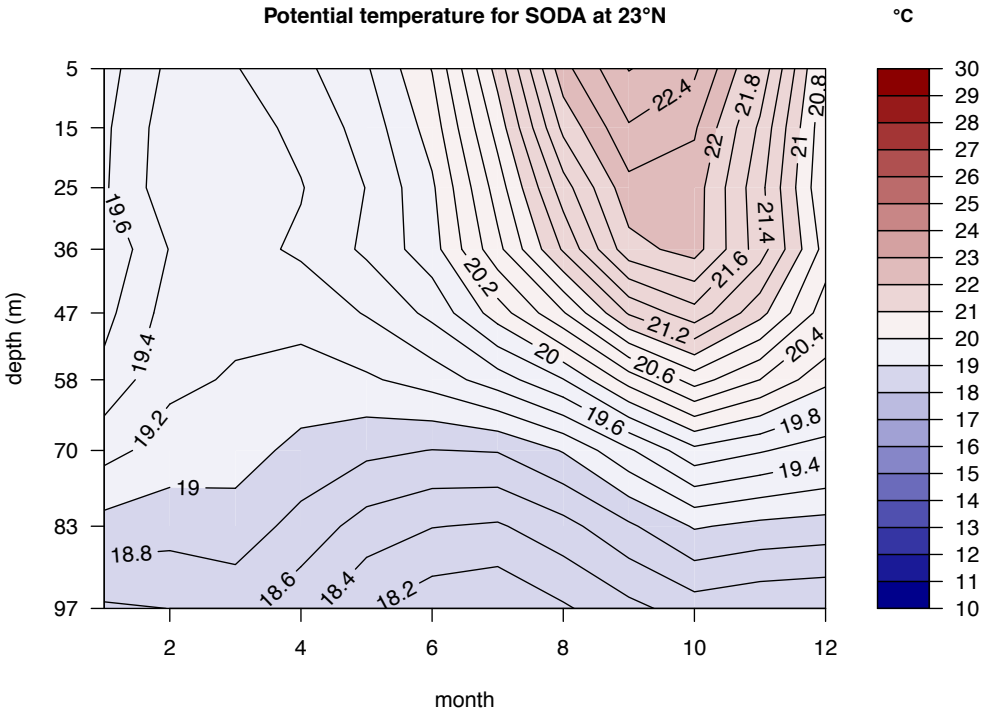

Fig. 4.4: *The same as Fig. 4.6 but for 23°N latitude.*

4.2 NWA upwelling system in CMIP5 models

4.2.1 Mean state

Regarding CMIP5 models, the upwelling index used to characterize the Ekman-induced upwelling in the region (see red box in Fig. 1.8) is correctly represented by CMIP5 models (second column, Fig. 4.2. Models present strong upwelling in winter between 18°N and 25°N, and weak upwelling in summer bellow 13°N.

Regarding the SST (Fig. 4.2b3), the impact of the strong northerly winds is not translated in colder SSTs. In this way, CMIP5 presents warmer SSTs

with stronger alongshore winds than observations, a feature that can be understood looking at the thermal stratification which is stronger in CMIP5 and prevents Ekman pumping to be effective in producing upwelling from below the thermocline. The winter cold SSTs are much less defined (and more to the north) in the ensemble mean than in observations. Models also show colder SSTs during winter in high latitudes, and a smaller but important difference during the monsoon season in lower latitudes (July to September, below 13°N).

The representation of thermocline depth (Fig. 4.2c3) and intensity (Fig. 4.2d3) is also accurate, although it is generally shallower in models, which also show a northward extension of the region of strong and shallow thermocline. It is important to note that CMIP5 maximum thermal gradient is stronger than reanalysis values (in some cases, such as summer around 19°N -see Fig. 4.2d3-, is greater than 100% of the gradient value).

From the comparison of seasonal cycles from models and observations (Fig. 4.2a3 and 4.2b3) it is apparent that there are warmer SSTs in models located in the transition between the season in which models have too much upwelling and that with too much downwelling. Models also show colder SST in winter in high latitudes (above 20.5°N). The reason of this seems to be that the SST field seasonality is not well captured in models, in which the spring minimum of SST is not well defined. Additionally, the clear link that was present in observations between upwelling and SST does not happen in the CMIP5 ensemble mean. The reason for that could be that the vertical thermal gradient is too strong in models (Fig. 4.2d2) and the wind stress is not able to upwell cold water to the surface, due to a lack of connection between the atmosphere and the ocean below the mixed layer. This explanation is reinforced by the similarity between Figs. 4.2b2, 4.2c2 and 4.2d2, which show the same general pattern (seasonal behaviour in the northern half, uniform values in the southern latitudes), and their disparity from Fig. 4.2a2: seasonal in the south, more uniform throughout the year in the north. In the first column of Fig. 4.2, instead, we find a much bigger accord between the four panels. In order to further study this, it is necessary to look at the vertical structure of the ocean.

4.2.2 Vertical structure of the ocean in CMIP5 multimodel ensemble

As seen in section 4.2.1 of this chapter, reanalysis data shows a consistency between SST and upwelling seasonal evolutions, that also match the spatio-temporal structure of the maximum vertical thermal gradient. This is not true for the CMIP5 ensemble, which have a much stronger temperature gradient (Fig. 4.2d2) leading to less consistency between SST and Ekman-induced upwelling. Figures 4.5 and 4.6 show Hovmöller plots of the annual evolution of potential temperature for the CMIP5 ensemble mean at 15°N and 23°N, representative latitudes for the seasonal and permanent upwelling, respectively. In both cases, it is apparent that the vertical gradient is stronger than in the reanalysis, producing a strong temperature difference between surface and the levels right below the thermocline. In Fig. 4.5, in March-April, the upwelling of colder water from 85m is not able to break through the thermocline, so its impact on the surface is non-existent. There is a certain amount of mixing in the upper layers (in both regions, 15°N and 23°N during summer; Figs. 4.5, 4.6), but the strong 'lid' that is the model's thermocline precludes cool water from reaching the surface. It is interesting to note that the SST biases in upwelling areas are generally warm. This too stratified thermocline might be at least partly responsible for this.

With the results from this section and the previous one, it is already possible to answer one of the posed questions: the relationship between upwelling and SST is indeed mediated by the depth and intensity of the thermocline. Therefore, the too strong vertical temperature gradient found in CMIP5 models inhibits the ability of modeled wind stress to have enough impact on surface temperatures.

Regardless of the strong vertical stratification present in the multimodel ensemble, which seems to prevent water from the bottom to reach the surface, it is important to analyze intermodel variability of the alongshore meridional winds, in order to identify causes which could potentially affect upwelling in the region.

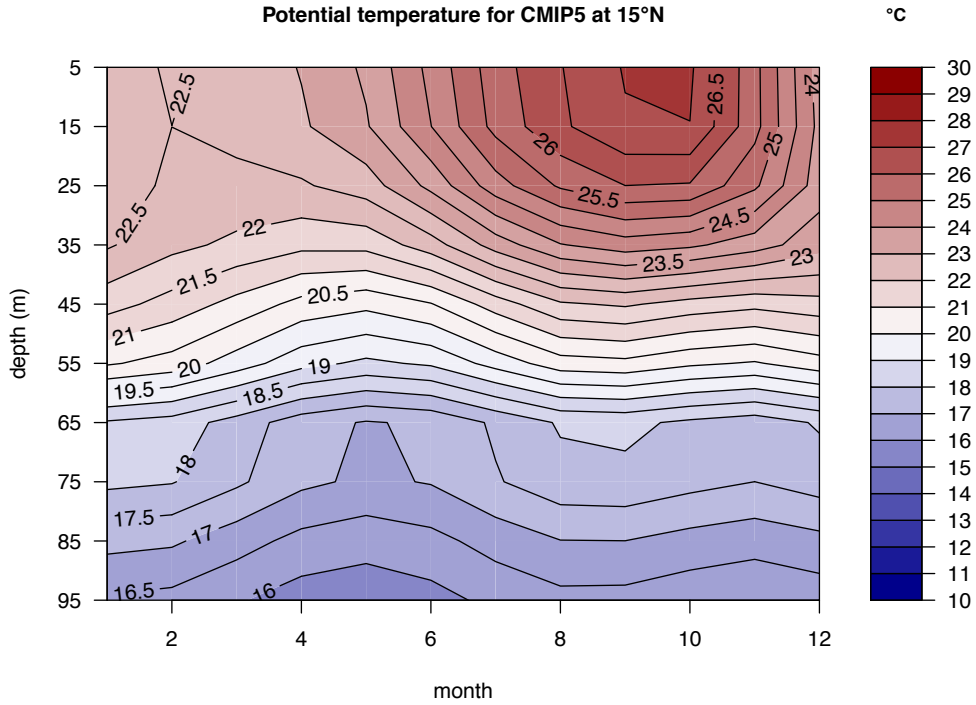

Figure 4.5: *Potential temperature (°C)* vertical *profile at 15°N for CMIP5 multimodel ensemble (averaged from 20°W to 15°W).*

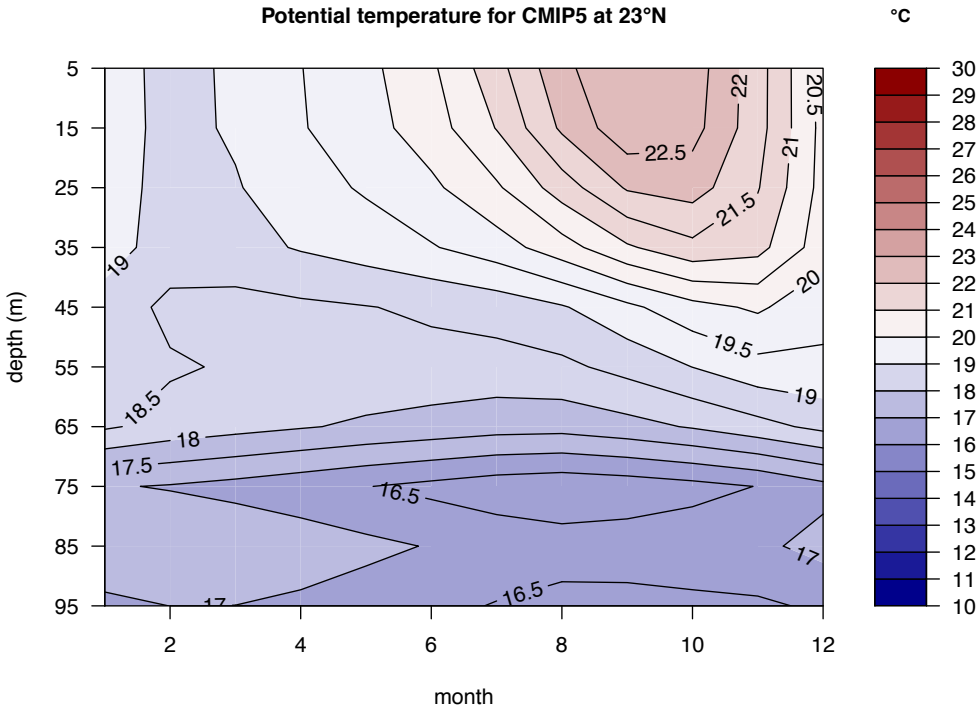

Figure 4.6: *Potential temperature (°C) profile at 23°N for CMIP5 multimodel ensemble (averaged from 20°W to 15°W).*

4.2.3 Intermodel variability of the upwelling index

In order to understand the different origins of the Ekman-induced upwelling, it is necessary to analyze the intermodel variability of the upwelling index. An overview of the 24 models (Fig. 4.7) shows that most of them have at least one of the two following features: a too intense seasonal upwelling around Cape Vert (15°N) and/or a too intense permanent upwelling around Cape Blanch (23°N). Figure 4.8 shows the spread of the upwelling index among models, in terms of standard variation calculated for the 24 models that compose the multimodel ensemble. A local maximum takes place in the permanent

upwelling region, but there is also another maximum in the seasonal upwelling area. Most of the models agree on showing a downwelling maximum in July-August around 11°N-12°N (Fig. 4.7), although there are important changes in its intensity, which is reflected on the spread (Fig. 4.8).

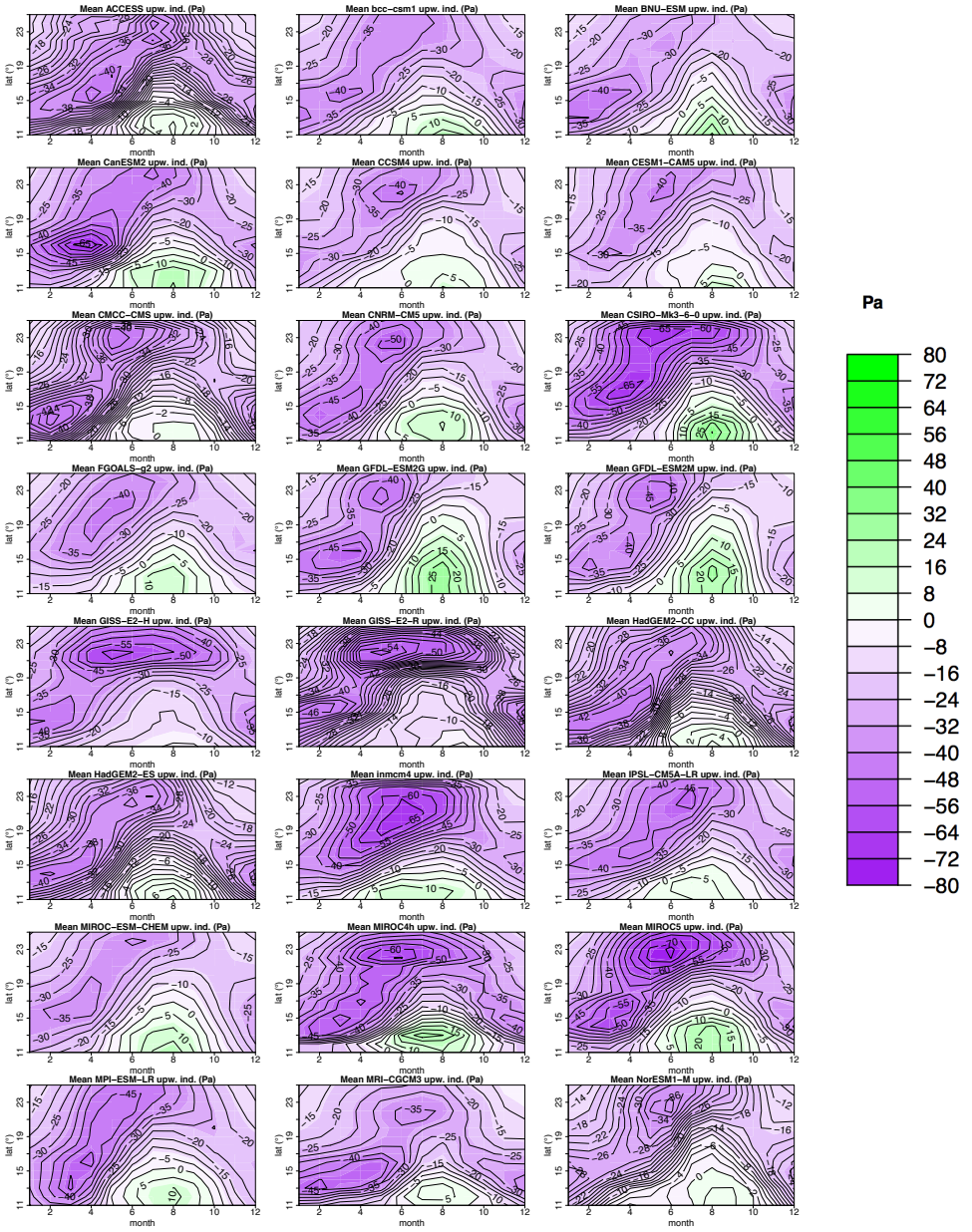

Figure 4.7: *Upwelling Hovmöller diagrams (months-latitude) for each of the 24 models considered (data averaged from 20°W to 15°W). The increment between contour lines is 5 Pa.*

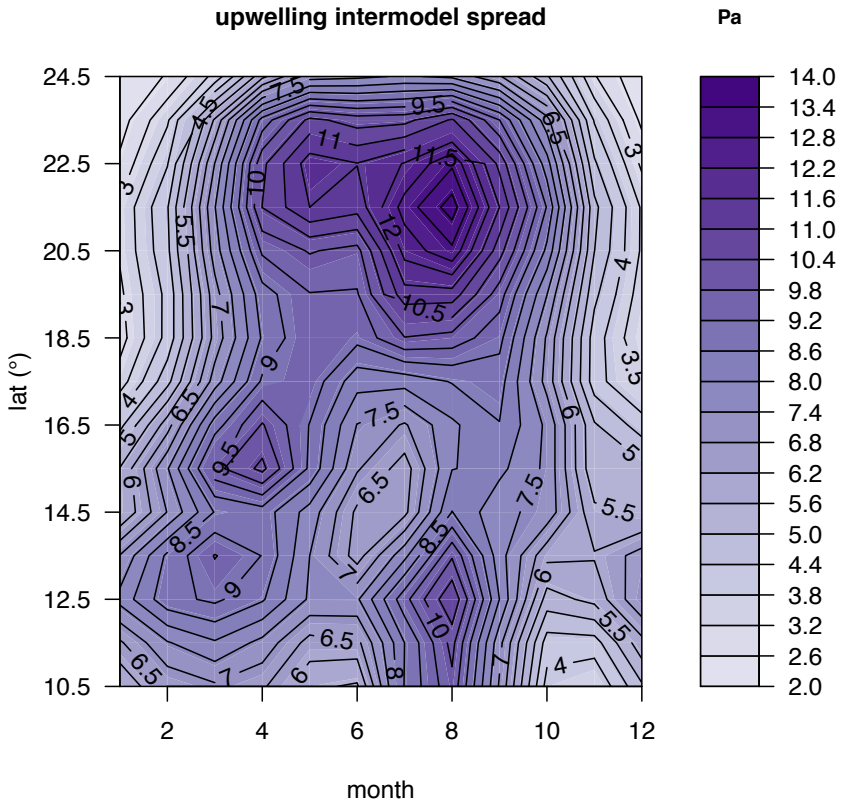

Figure 4.8: *Upwelling index (N/m²) intermodel standard deviation (averaged from 20°W to 15°W). Darker areas show higher values (bigger intermodel spread).*

The goal now is to understand what drives the different behaviour of models. Since studying all 24 models one by one would not be practical, we will use Empirical Orthogonal Functions in order to reduce the degrees of freedom and analyze the principal directions in which intermodel variability of the upwelling index is organized.

To this aim, the 24 hovmöllers in Figure 4.7 are organized in a matrix and, for each point in the hovmöller, the different behaviour of models is compared by computing a covariance matrix described (see Chapter 2).

The two first EOFs (Fig. 4.9, top row) explain almost 70% of the intermodel variability of the upwelling Hovmöller. The first mode, which explains 47% of the variability, is significant for most of the domain, mainly for latitudes north of 16°N and during summer months.

The second mode presents a dipolar structure, with different signs in the winter than in the summer months, indicating that this mode is more seasonal dependent. The stronger and significant scores are centered mainly during the West African monsoon months.

Bottom row of Figure 4.9 shows the two associated principal components of the intermodel variability for upwelling index. Positive scores of the associated PC (figures 4.9.c and 4.9-d) indicate models with an upwelling configuration similar to figure 4.9.a and 4.9.b respectively. The opposite pattern is associated with models presenting negative scores in the PCs.

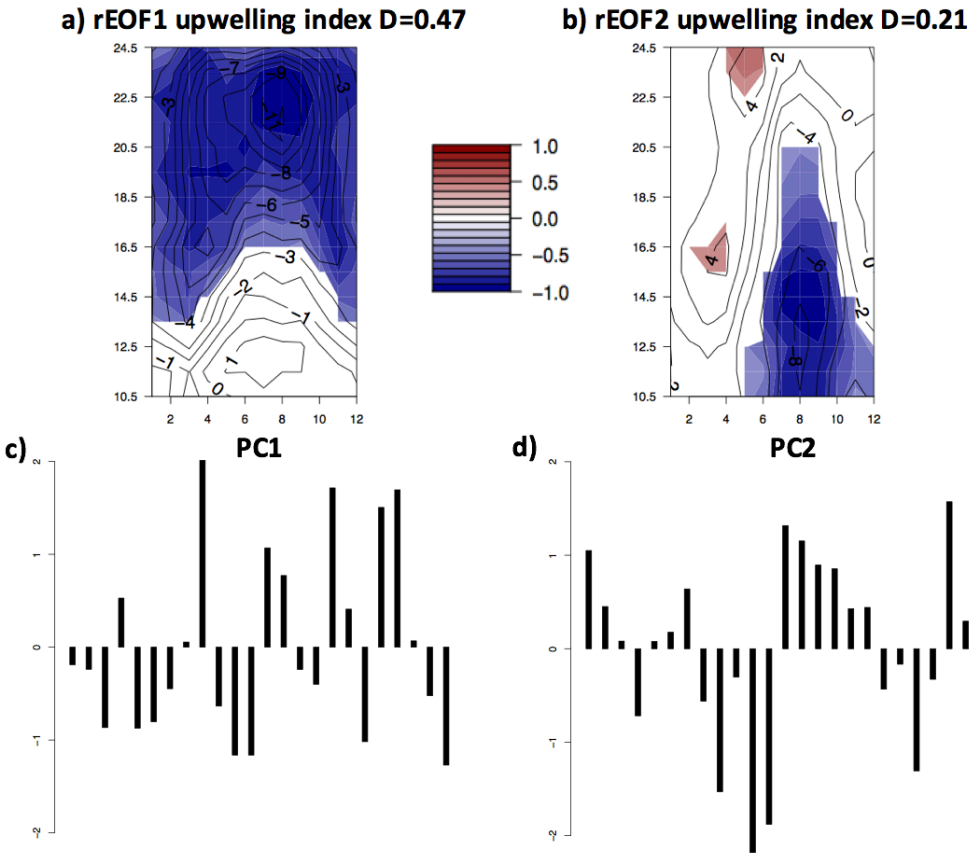

Figure 4.9: *a) EOF1 and b) EOF2 of the intermodel variability of the month-latitude Hovmöllers of the upwelling index. The EOFs are represented as the regression of the standardized PC onto the upwelling index. The correlation between the PC and the intermodel variability in each point of the Hovmöller is calculated and shading areas represent the correlation in those regions and months in which they are significant at the 90% level. The fraction of variance explained by each mode is indicated at the top of each Figure 4. (D) c) PC1 and d) PC2 standardized scores for the upwelling index.*

For positive values of PC1, EOF1 is significant and negative north of 16.5°N for all months, and above 14°N for winter and early spring. It is non-significant and positive for summer south of 13°N. Its maximum absolute values are located between 20°N and 24°N in summer. This EOF presents a structure

with significant values over the regions and months in which models present an exaggerated upwelling. That is, models with a strong positive PC1 will be likely to show exaggerated upwelling index in northern latitudes. Figure 4.9a shows that the first EOF for upwelling index presenst its maximum significant scores in the areas of greater intermodel variability, and has a dominant meridional structure. This means that, models with positive PC1 present stronger northerly winds during most of the year between 20°N and 24°N, and stronger southerly winds during summer at 12N (although this feature is not significant), which indicates an enhancement of the multimodel ensemble mean values. The Hovmöller plot of the differences between CMIP5 and SODA (Fig. 4.2a3) also shows a local maximum in that area, as well as an absolute maximum between 21°N and 23°N in early summer. By construction, models with negative PC1 values will behave all the way around. This spatial mode is robust across models for more than half of the region of study.

The second EOF explains 21% of intermodel variability and shows a much stronger seasonal behaviour than EOF1 (Fig. 4.9b). It presents a dipolar structure in which models with positive values in PC2 behave contrary to climatology: strong upwelling index in the monsoon season and weak upwelling index in the upwelling season, thus showing a weakening in the seasonal cycle. The most robust feature is the weakening of the southerly winds in relation to the concomitant West African monsoon during boreal summer. By construction, models with a strong negative PC2 are likely to show too much downwelling during summer months.

In order to understand globally the intermodel spread in the representation of the upwelling and how these patterns are related to big-scale model features, different variables have been projected on the principal components of the modes. To this aim, correlation maps have been calculated between each of the PCs and the intermodel variability for the variables in Figure 4.10 and 4.11. Positive values in Fig. 4.10 and 4.11 mean that the patterns shown in Fig. 4.9a and 4.9b respectively are linked to the represented global maps. By

construction, negative values put forward that the pattern in Fig. 4.9a and 4.9b are related to the opposite maps in Figure 4.10 and 4.11.

First mode of variability

In relation to EOF1, a positive PC1 is related to lower pressure over land and a west-east SLP pressure gradient, over West Africa and the Atlantic Ocean, at subtropical latitudes in spring (Figs 4.10a1 and 4.10b1). In terms of rainfall (Figure 4.10a2 and 10b2), a northward shift of the ITCZ is significant for positive PC1 both in spring and summer, in association with an enhancement of net radiation (which is defined as positive when incoming onto the planet) over Africa and Northern South America (Fig. 4.10a3 and Fig. 4.10b3). From the results in Figure 4.10, the mechanism proposed to explain intermodel variability of the leading mode of upwelling index Hovmöller, is as follows:

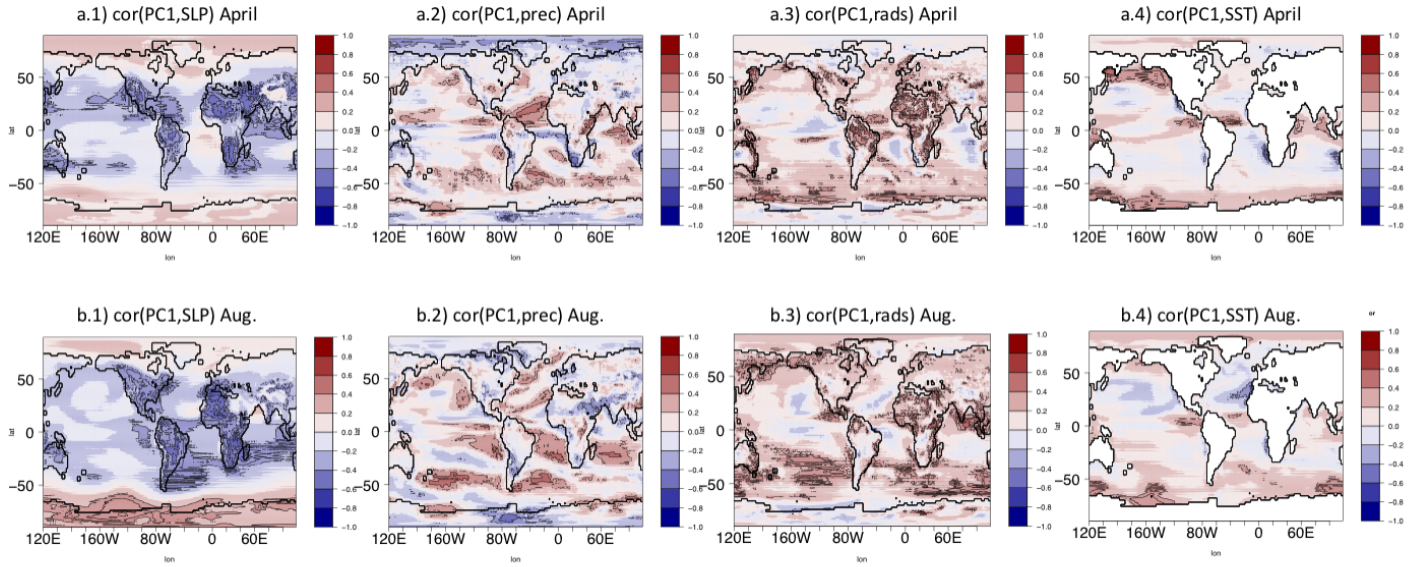

Figure 4.10: *Top row: intermodel correlation between upwelling index (PC1 and climatological mean for April of SLP (a.1), precipitation (a.2), net radiation at the surface (a.3) and SST (a.4). Bottom row: intermodel correlation between upwelling index PC1 and climatological mean for August of SLP (b.1), precipitation (b.2), net radiation at the surface (b.3) and SST (a.4). Correlations significant at the 90% level (Student t-test) are marked in contours.*

The strong zonal land-sea pressure gradient associated with a strong low pressure over the continents produces alongshore northerly winds due to the geostrophic adjustment that increase upwelling intensity in more than half the domain. These winds reach more southern areas in April than in August, due to the atmospheric seasonal cycle, which affects the location of the pressure center in the Northern Tropical Atlantic and the ITCZ position. In boreal summer, and for the lower latitudes in the box, the value of the EOF1 has the opposite sign to that of the rest of the domain, which is related to the land-sea pressure contrast being much weaker than for northern latitudes. The ultimate driver of this mechanism is the excessive incoming net radiation over land, which warms the continents during the day (not shown). Although there is no significant surface temperature signal due to the cooling over the night, the effect of this diurnal warming weakens the downward branch of the Hadley cell, lowering SLP over the continents and producing the aforementioned land-sea gradient. This mechanism is reflected in a different bhaviour for the northern half of the domain (permanent upwelling) than for the southern half (seasonal upwelling).

Second mode of variability

The global projection of mode 2 onto different atmospheric variables, by means of intermodel correlations with PC2 is represented in Fig. 4.11. In this case, the maximum correlations with SLP occurs over the ocean. For the positive phase in spring, negative correlation with SLP appears over the tropical North Atlantic, and no signal over northern Africa (Fig. 4.11a1). Thus, a weakening of subtropical anticyclones during spring is associated with models that have a weaker seasonal cycle of the upwelling. This is consistent, as a strong (weak) upwelling in the Northern Hemisphere appears in association with northerly (southerly) alongshore winds, which take place when the subtropical anticyclone is enhanced (gets weaker) over the sea.

Parallel to this, the signal in precipitation corresponds to a slight increase over the NWA upwelling region and a strong decrease over central and southern Africa in spring (Fig. 4.11a2). Incoming radiation also increases over western Sahara and the upwelling region in association with a weakening of SLP (Fig.

4.16a3). Regarding SSTs, a warming in the subtropical gyres, stronger in the Southern Hemisphere, takes place (Fig. 4.11a4).

Contrary to what happened for EOF1, there is a strong seasonal change in the relationships between the upwelling index and the atmospheric variables, and the bottom row of Fig. 4.11 shows very different results when compared with the top row. SLP in August (Fig. 4.11b1) is characterized by a high-pressure system over the upwelling region and tropical North Atlantic and no signal over Sahel, which leads to a negative land-sea gradient. Precipitation (Fig. 4.11b2) is greatly decreased over Sahel, Western Sahara and tropical North Atlantic, and increased towards the equatorial Atlantic and South America. This is consistent with a southward shift of the ITCZ, as well as with the strong positive signal in Southern Hemisphere SST (Fig. 4.11b4). There is almost no signal for incoming radiation in our region of interest (Fig. 4.11b3).

The driver of upwelling is, in both seasons, the alongshore wind, canalized by the land-sea zonal SLP gradient. Thus, upwelling is reduced in spring (positive gradient) and enhanced in summer (negative gradient). However, contrary to what happened in EOF1, in this case the mechanism is clearer for summer than for spring. We propose this: the well-known problem with excessive ocean warming that some models show (Wang et al., 2014) leads to a too much warm southern than Northern Hemisphere, especially in the Atlantic Ocean in summer, causing the ITCZ to shift southward. This prevents the climatologically southwesterly winds (monsoon winds) to reach north in boreal summer, which results in anomalous upwelling, due to the local high-pressure area in front of NWA, and a strong reduction of precipitation all over the Sahel and the adjacent Atlantic Ocean. The mechanism at work in spring is not so clear, which might be related to the EOF2 not being as significant in spring as in summer (Fig. 4.9b).

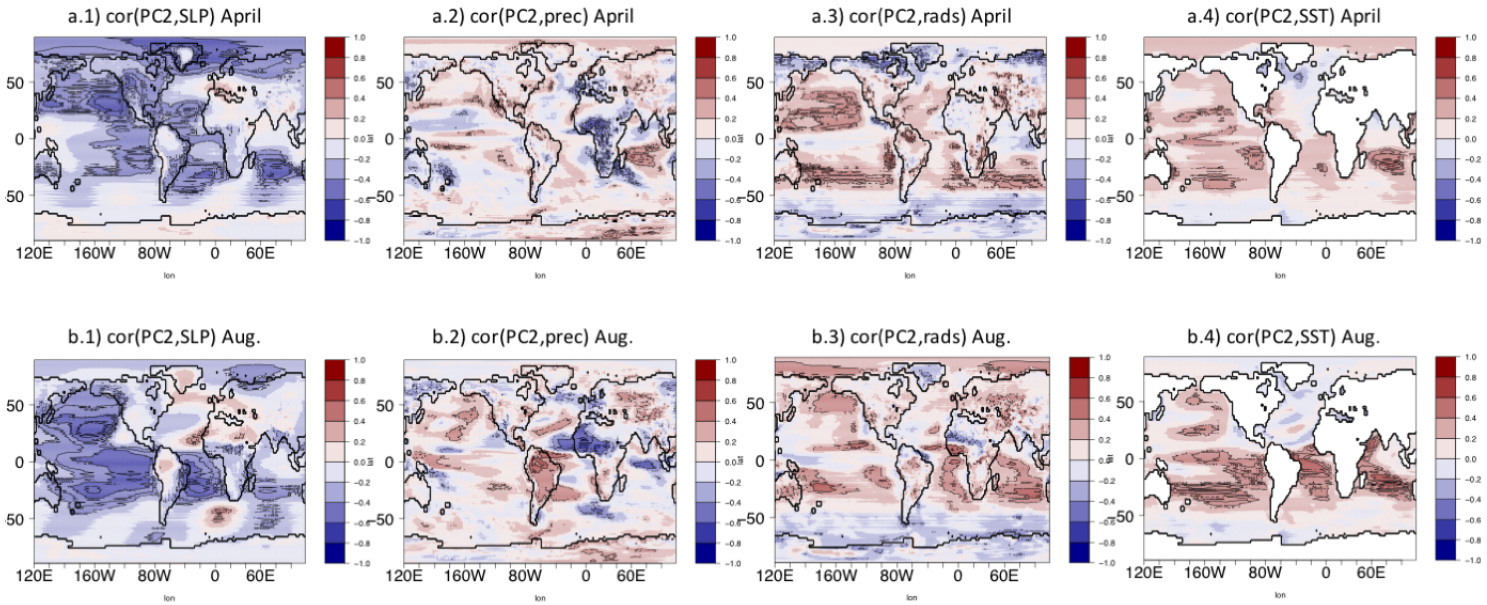

Fig.ure 4.11: *Top row: intermodel correlation between upwelling index PC2 and climatological mean for April of SLP (a.1), precipitation (a.2), net radiation at the surface (a.3) and SST (a.4). Bottom row: intermodel correlation between upwelling index PC2 and climatological mean for August of SLP (b.1), precipitation (b.2), fraction of cloud cover (b.3) and SST (a.4). Correlations significant at the 90% level (Student t-test) are marked in contours.*

4.3 Discussion and conclusions

From the results shown in this chapter, it is clear that the main driver of upwelling index in models is the zonal land-sea SLP gradient in the Northwest Africa region. For the first mode, net surface radiation over land is the cause of this gradient. That is: models which a positive PC1 have a too high net radiation over Africa show a weakened downward Hadley branch and their ITCZ shifts to the north. At the same point, the excess warming on the continent contributes to a lower SLP, and creates a land-sea gradient which increases coastal northerly winds along the Western Africa Coast, enhancing upwelling. Our results indicate how models with a low net incoming radiation (negative PC1) reduce the upwelling, while the opposite for those models with excessive net incoming radiation.

CMIP5 models present, in average, positive net radiation bias (Li et al., 2013). Therefore, the excessive upwelling bias shown in this chapter would be related, through the first mode of variability, to the net radiation bias. Furthermore, according to Xu et al., (2014), CMIP5 models show, in the tropical region, excessive downward shortwave net radiation, which in the ocean is overcompensated by excessive outward longwave fluxes, resulting in a negative net radiation bias over the tropical ocean. However, over the continent these outward fluxes are not able to compensate the excessive downward net radiation, which leads to an incoming net bias. This would be the case, in our study, for models with positive PC1. In these models, the excessive downward radiation on the Saharan region produces a weakening of the descending branch of the Northern Hadley Cell (decreased SLP) over the continent (Fig. 4.12). This creates a sea-land pressure gradient which channels alongshore winds and causes the excessive upwelling in those models. In the tropical region there is no relationship between SW radiation and SST in CMIP5 models (Xu et al., 2014), this, together to the diurnal cycle (the excessive daily heating due to excessive SW radiation is dissipated during the night), is why there is almost no signal in continental surface temperature, although the positive SST region in the warm pool in the Atlantic is consistent with a weakening of the Northern Hadley Cell (NHC). This

weakening of the NHC is also consistent with the slight northward shift of the ITCZ (Lipat et al., 2017).

The second mode is driven by differential hemispheric warming in models. In models with a positive (negative) PC2, the Southern Hemisphere warms more (less) than the northern one, which in turn shifts southward (northward) the ITCZ over the Atlantic (Fig. 4.12, right). Models which show a positive PC2 could be affected by excessive warming over the Southern Ocean, typical of coupled models (Wang et al., 2015; Mechoso et al., 2016), due to a poor representation of low-level clouds or the Meridional Overturning Cirulation, which prevents an adequate representation of radiation budget.

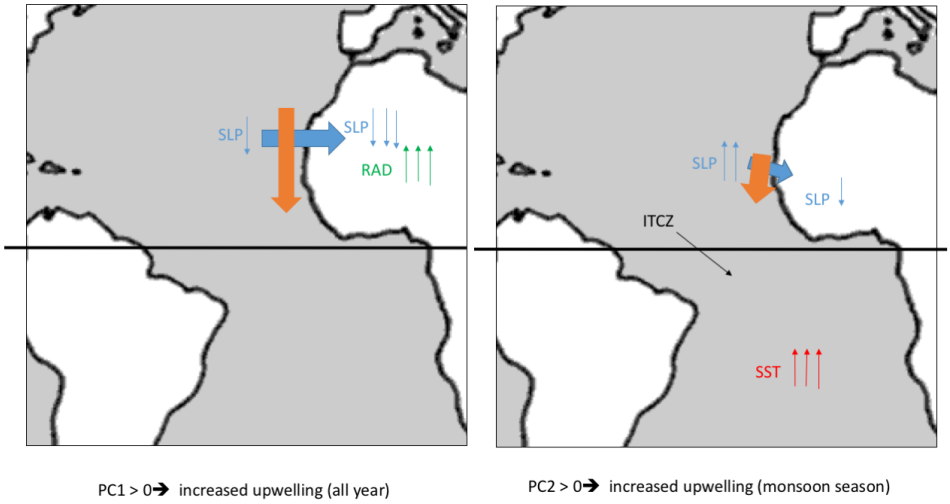

Figure 4.12: *Simplified model of drivers of increased upwelling for positive values of PC1 (left) and PC2 (right). Blue thick arrows indicate the direction of the SLP gradient (from higher relative SLP to lower relative SLP), and orange thick arrows show the direction of the anomalous surface winds.*

In this chapter we set out to answer three questions about the NWA upwelling behaviour in CMIP5 models: 1) Is NWA upwelling well captured by CMIP5 models? 2) Do the relationships found in observations between upwelling index, SST and thermocline depth and intensity hold for coupled

models? 3) Which features of local and global biases affect the representation of upwelling in the Canary Boundary Current region?

Regarding the general representation of wind-driven upwelling by CMIP5 models, it seems that the general seasonal cycle it well captured by the ensemble and almost all models, although winds are too strong in most of them. The permanent upwelling index is exaggerated by the ensemble mean, due to this feature being very prominent on a reduced number of models. Most models show a much smaller bias in this region. Most models show also an excessive seasonal upwelling in the Cape Vert region, and too much downwelling during the monsoon season.

In order to bring forward an explanation for this, it has been studied how local upwelling relates to local and global variables, and the most important local effect controlling upwelling index is the SLP gradient between land and sea, which depends mainly on the ITCZ position and the net radiation budget. This means that model radiation biases heavily affect upwelling representation.

Unfortunately, the answer to our second question tells us that even the best correction of CMIP5 wind biases on upwelling regions would not lead to a realistic representation of all variables of the upwelling phenomenon in these models due to the excessive stratification of the ocean, which prevents cold, deeper water to ascend to the surface, thus making it very difficult to link the atmospheric part of the process to its observed biogeochemical implications. Enhancement of ocean resolution can better represent ocean stratification and, thus, upwelling (Marshall et al., 2002; Small et al., 2015)

Further work on this matter must address, therefore, the role of radiation and ITCZ biases in the representation of the upwelling, as well as the importance of ocean stratification on atmosphere-ocean coupling in upwelling regions.

5 Sensitivity of Northwest African upwelling to ITCZ shifts

5 Sensitivity of Northwest African upwelling to ITCZ shifts

In the previous chapter it has been shown that around 20% of the intermodel variability of upwelling in CMIP5 depends on a seasonal mode which is related to the position of the ITCZ. Within this context, some works relate a southward shift of the ITCZ in coupled models to extratropical thermal forcing due to excessive incoming shortwave radiation in the Southern Ocean (Hwang and Frierson, 2013; Kang et al., 2008; among others). However, the extent to what extratropical forcings can produce an ITCZ shift is controversial and appears to be strongly model dependent (Kay et al., 2016; Mechoso et al., 2016). In this way, Mechoso et al. (2016), showed that the tropical SST-low level clouds feedbacks were crucial in order to achieve a response in the ITCZ to changes in the extratropical energy forcing. According to their results, UCLA model showed a particular intense response in the ITCZ position when compared with other models.

Nevertheless, and despite the significant amount of recent literature on this issue, to our knowledge no previous work has gone a step forward to study the impacts of the ITCZ latitudinal position in other aspects of climate variability.

In this way, the analysis of CMIP5 models has led to the hypothesis of a possible link between ITCZ movements and NWA upwelling. This chapter will try to address this issue with the aid of a set of experiments performed with UCLA-GCM.

Therefore, in this chapter we try to answer the last of our research questions:

Q5.1: How does ITCZ shifts due to changes in the large-scale extratropical incoming energy affect NWA upwelling representation?

To this aim, an idealized sensitivity experiment with UCLA-GCM, in which a radiative flux correction is used to cool the Southern Ocean was run and analyzed, to explore the impact of such correction in the NWA upwelling.

In this chapter, we start by describing the performance of a control run from UCLA model in comparison with the reanalysis. Then we put the model in context with the rest of CMIP5 models used in this work, both in terms of climatology and intermodel variability. We continue by describing the main characteristics of our sensitivity experiment (hereafter COSZ experiment) and how its climatology differs from UCLA control. Finally, we analyze the impact of such changes in the characterization of the NWA upwelling. The data and methods used in this chapter are summarized in Figure 5.1.

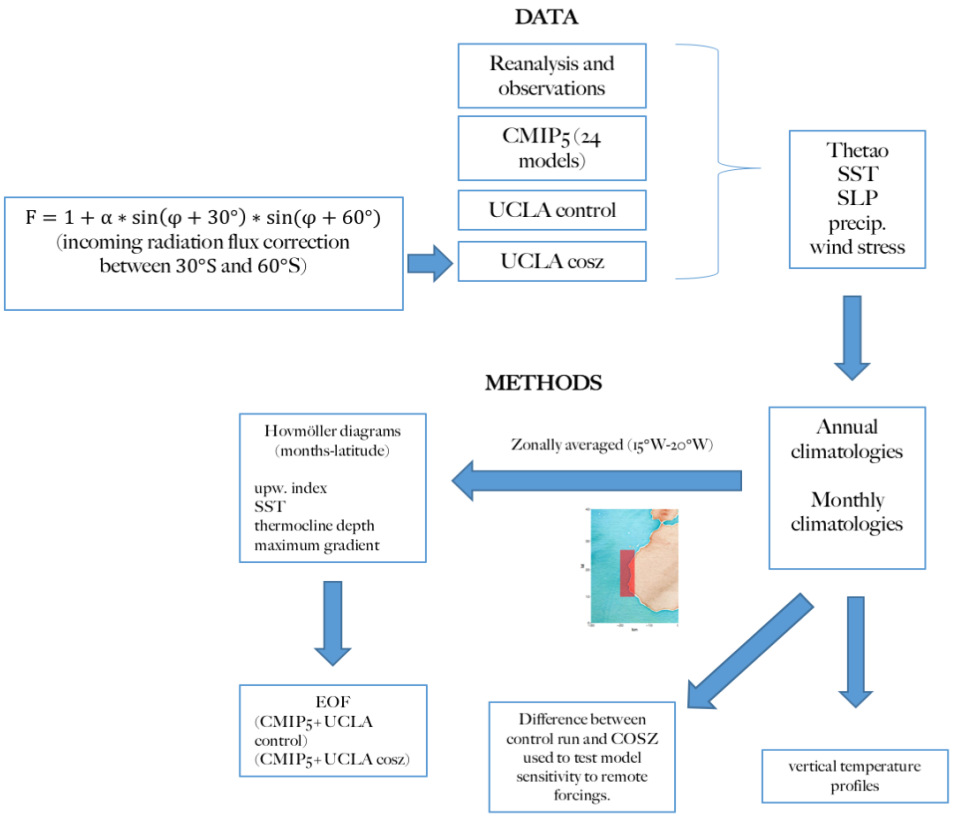

***Figure 5.1**: Summary of the data and methods used in this chapter. Monthly and annual climatalogies are computed for variables obtained from reanalysis and CMIP5 datasets (ocean temperature (thetao), SST, SLP, precipitation and wind stress). The UCLA CGCM is run to obtain a control simulation from which the same variables are selected. A sensitivity experiment in which incoming radiation is reduced over the Southern Ocean is run and its data processed in the same way. Vertical temperature profiles are computed from monthly climatologies of thetao. Upwelling index is computed from meridional wind stress, and thermocline depth and intensity are obtained from thetao. These three variables together with the SST are used to characterize the upwelling region both in reanalysis and the two UCLA simulations, and are zonally average from 20°W to 15°W before being represented in a Hovmöller diagram. From the Hovmöller diagrams of all 24 CMIP5 models together with the two UCLA simulations (one at a time), the first EOFs are computed. More details on datasets and methods can be found in Chapter 2.*

5.1 UCLA model performance and biases

The UCLA coupled general circulation model is known to have, as all coupled models do, biases (Mechoso et al., 2016). In order to identify the main characteristics of such biases, in this section, we will analyze the climatology of a control run, in which 1980 radiative forcing conditions were used. The three large-scale variables on which the analysis will focus are sea surface temperature (SST), sea level pressure (SLP) and daily precipitation (pr).

UCLA model has a generally warm SSTs bias for most of the globe (Fig. 5.1a) that is maximum in the Southern Ocean (7 °C in some regions and more than 5°C in most of the band between 50°S and 60°S). The only regions in which the bias is negative are latitudes below 70°S and over 60°N and the Peruvian upwelling, were the SST bias is very small. However, the model shows an anomalous interhemispheric temperature gradient that is clearly north-south: the Southern Ocean bias is much warmer than the rest of the globe. It is also relevant to note that, except for the already mentioned Peruvian upwelling, UCLA control upwelling regions are warmer than the adjacent regions, with the south east Atlantic upwelling (Angola-Benguela) and the California upwelling presenting especially strong biases. This is a common feature shared by almost all global coupled models.

Regarding the SLP bias (Fig. 5.1b), it is very negative in the northern jet region (40°N-60°N) and for most tropical and mid-latitudes. The only regions where there are high, although not very strong, pressure biases are located over the continents (Northern Africa, Central North America and Australia), while the subtropical anticyclones show strong negative biases. Overall, this tells us of a Hadley circulation weaker than in the reanalysis.

The UCLA control run shows excessive precipitation almost everywhere (Fig. 5.1c), which is consistent with the warm SST bias. The ITCZ in the Atlantic Ocean shows a southward shift, which seems related to the far too warm Southern Atlantic Ocean. This leads to a lack of precipitation over West Africa. Also, the UCLA model show very little precipitation bias in the

equatorial Pacific, but the precipitation is far too much around 20°S in all tropical oceans.

After providing an overview of how are the global biases of the UCLA control, next section will focus on evaluating how does the model represent the Northwest African upwelling region.

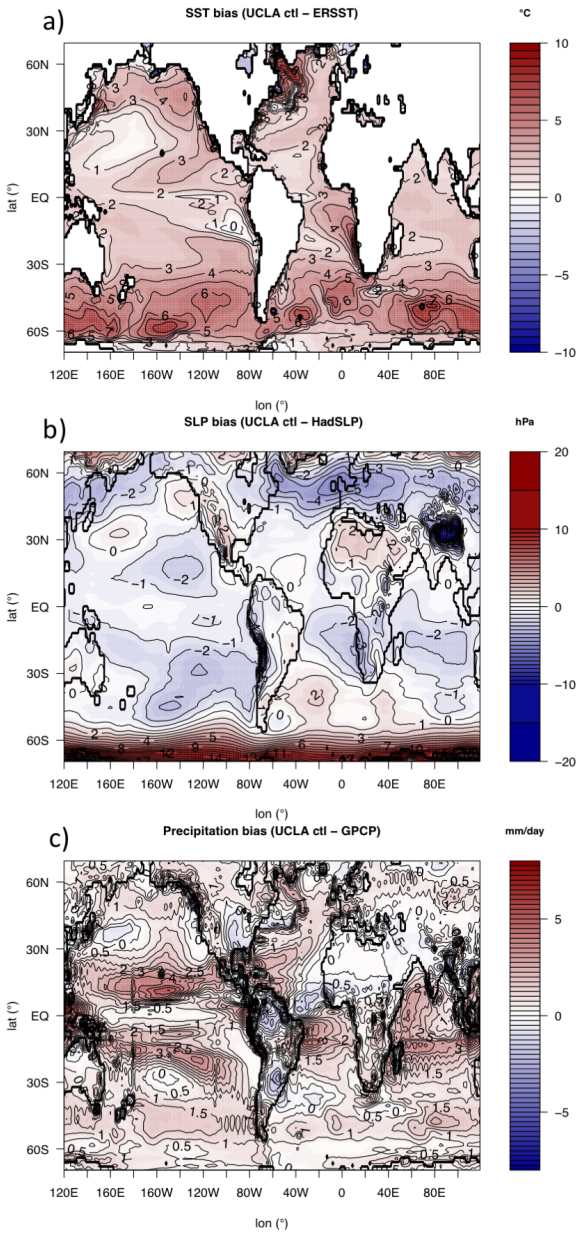

Figure 5.2: *Differences between UCLA control annual climatology (85 years) and reanalysis climatology for a) SST (ERSST, 1979-2008, °C), b) SLP (HadSLP, 1979-2008, hPa) and c) daily precipitation (GPCP, 1979-2008, mm/day).*

5.1.2 Representation of the seasonal evolution of NWA upwelling in UCLA model

Before addressing the impact of changes in the ITCZ positions in the NWA upwelling, it is mandatory to evaluate the way in which our model simulates such upwelling. To this aim, the present section is based on the analysis on Hovmöller plots of the zonal (15°W-20°W) mean of the four variables that have been considered more useful for studying upwelling: upwelling index, SST, thermocline depth and maximum vertical thermal gradient value.

The seasonal evolution of the upwelling index for each latitude of the region of study is shown in Figure 5.3a1 to 5.3a3. UCLA shows weaker upwelling than observations for all months and latitudes except for the permanent upwelling region (around 23°N) during the summer months and around 15°N during June. This maximum for the seasonal upwelling is correctly located at 15°N, although it occurs a bit later than in observations, and the effect of monsoon winds, which diminish and even reverse upwelling index below 13°N of latitude in summer months in observations, is also properly captured (the bias in that region is very low).

Contrary to what happened with CMIP5 models (see Fig. 4.6 in chapter 4), there is a good correspondence between the upwellling index and the ocean variables (Fig. 5.3, three bottom rows). The Hovmöller plot for the model SST (Fig 5.3b2) shows the same general shape as for the reanalysis (Fig. 5.3b1), with colder values during the first half of the year and a warm tongue during summer and autumn. The warm tongue is correctly located and developed, although it is far too hot, as expected given the general model biases of SST. The reason for this agreement between upwelling and SST pattern can be found in the thermocline depth and maximum gradient value (bottom two rows of Fig. 5.3). The Hovmöllers of these two variables are very similar to those from the reanalysis, except for the model having a too deep thermocline in the north and for winter-spring seasons. The explanation for this consistency between all variables is found in Fig. 5.3d2 and Fig. 5.3d3: the maximum vertical gradient in UCLA is weaker than in the reanalysis and much weaker than it was in CMIP5 models. This makes it easier for vertical

movements to occur in the ocean. Therefore, the effect of the wind stress is more easily felt by the water column and leads to a more realistic seasonal evolution of SST and thermocline depth, even if the Hovmöller of the upwelling index is in fact weaker than that from the CMIP5 ensemble.

In the light of these results, the vertical structure of the ocean in the upwelling region in UCLA merits a more in depth study, which will be carried out in the next section.

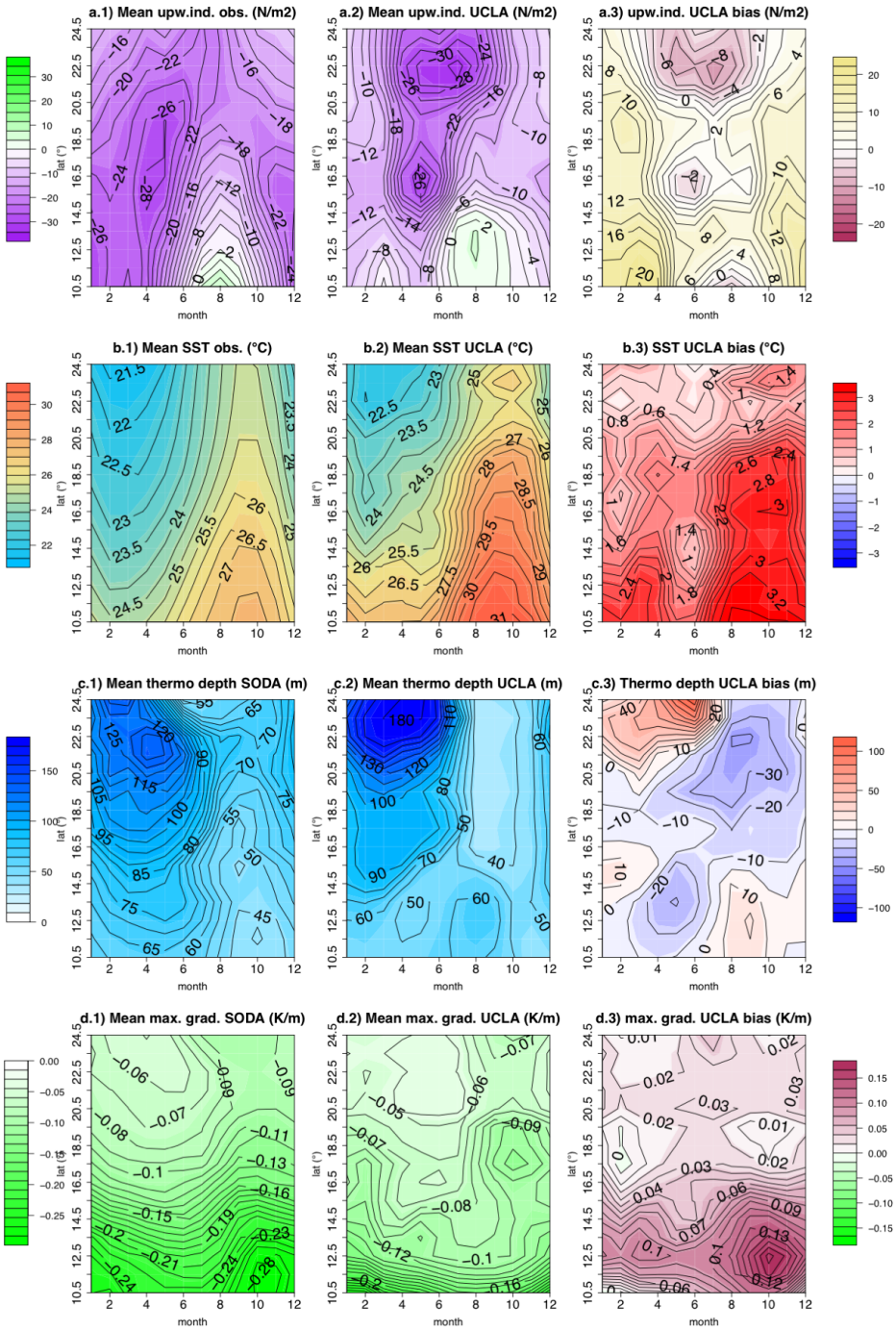
a.1) Mean upw.ind. obs. (N/m2)
a.2) Mean upw.ind. UCLA (N/m2)
a.3) upw.ind. UCLA bias (N/m2)
b.1) Mean SST obs. (°C)
b.2) Mean SST UCLA (°C)
b.3) SST UCLA bias (°C)
c.1) Mean thermo depth SODA (m)
c.2) Mean thermo depth UCLA (m)
c.3) Thermo depth UCLA bias (m)
d.1) Mean max. grad. SODA (K/m)
d.2) Mean max. grad. UCLA (K/m)
d.3) max. grad. UCLA bias (K/m)
lat (°)
month

Figure 5.3: *Hovmöller plots of monthly zonally averaged a) upwelling index (N/m²); b) sea surface temperature (SST) (degrees Celsius); c) thermocline depth (m); d) thermal gradient at the thermocline level (°C/m) for SODA (left), UCLA control (center), and UCLA control bias (right). Plots are computed by zonally averaging the climatological monthly means of the variables between 20° W and 15° W for each latitude.*

5.1.3 Vertical structure of the ocean in UCLA model

The way in which a model represents the vertical structure of the ocean is fundamental for the upwelling to be able to bring upwards deep water that can impact the sea surface temperature. As it was highlighted in Chapter 4, CMIP5 models analysed in this thesis show a too strong stratification can prevent vertical movements to reach the ocean surface, even when simulated winds are exaggerated when compared to observations. Conversely, results from the previous section highlight a quite different behaviour in UCLA model, which shows a much weaker maximum gradient than CMIP5 models over the NWA upwelling region. To further analyse this issue, we compare the vertical profiles of UCLA and SODA ocean temperature in two latitudes representative of the seasonal and permanent upwelling regions of NWA upwelling: 15N and 23N respectively. The vertical structure in the first 250 metres of ocean in SODA is shown in Figure 5.4a (15°N) and Figure 5.4b (23°N). For 15°N, the thermocline is less well defined in spring than in summer and autumn. In spring there is a clear upwelling effect which makes water from depths of 40-50 meters reach the surface, while in summer and autumn there is no upwelling and the temperature difference between the surface and the water below the thermocline is smaller than 2°C. It must be noted that subsurface biases are even stronger than in the surface, which could lead to surface temperature biases even in presence of effective upwelling.

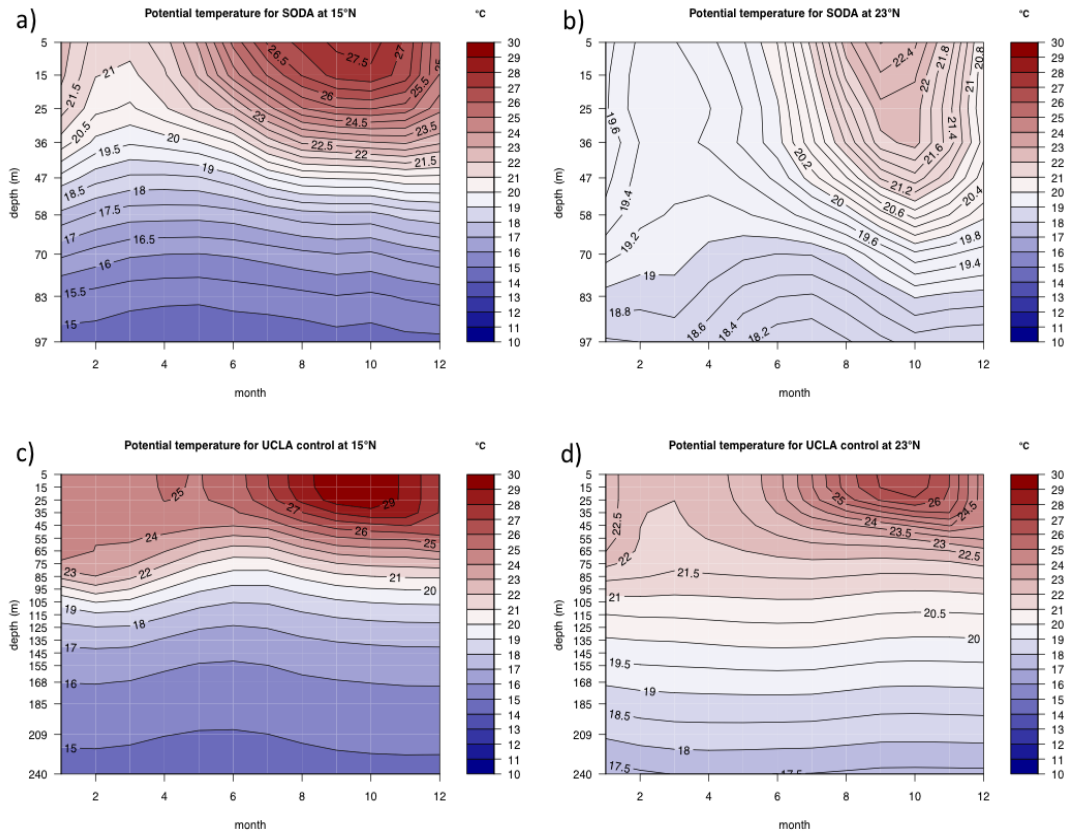

Figure 5.4: *Ocean potential temperature Hovmöller diagram for SODA reanalysis (top row) at 15°N (left) and 23°N (right) and UCLA control run (bottom row) at 15°N (left) and 23°N (right). Hovmöller plots were obtained by firstly zonally averaging the variables between 20°W and 15°W for each latitude and depth, and secondly computing the climatological monthly means.*

5.1.4 UCLA model performance in the context of CMIP5 models

In the previous sections of this chapter, an analysis of the ability of UCLA model to simulate the main characteristics of the seasonal evolution of NWA upwelling and related variables has been made. Here, before analysing the

sensitivity of the NWA upwelling to ITCZ shifts in the model, a comparison between the results from UCLA and CMIP5 models is made.

In this section we start by comparing the annual mean of the control run with the ensemble mean of the 24 CMIP5 models used along this thesis. Diagnostic variables analysed in the control simulation are sea surface temperature (SST), sea level pressure (SLP) and daily precipitation (pr) (Figure 5. 5).

UCLA model has much warmer SSTs than the CMIP5 ensemble mean (Fig. 5.5a). This excessive warming can be in part, attributable to the UCLA control run using 1980-era radiative forcing (which means that part of the effect of climate change is being considered) and the CMIP5 ensemble using 1850 preindustrial radiative forcings. The difference reaches 8°C in the Southern Ocean and the northern Atlantic, and is mimimum in the upwelling region off the Peruvian coast (Eastern Pacific), where it is smaller than 2°C. Its general hemispheric pattern, however, is similar to the bias pattern shown by CMIP5 models (Fig. 1.9, chapter 1): the Southern Ocean shows much bigger differences than the rest of the globe except for the Western North Atlantic.

The SLP difference with the CMIP5 ensemble (Fig. 5.5b) is negative for most of the globe. In fact, the only regions where UCLA control shows higher SLP than the CMIP5 ensemble are the west coasts of the continents (North America, South America and Africa, although barely) and the belt below 40°S. The subtropical gyres show smaller pressure values than the CMIP5 ensemble, as well as the northern jet.

As for daily precipitation (Fig. 5.5c), UCLA model shows more precipitation than the ensemble mean, especially in the tropics and subtropics, together with a dry bias in the equatorial region; the Pacific double ITCZ problem is not as important as it is for CMIP5 model. It has, as was in Fig 5.3c, a weak West African Monsoon, as well as an especially strong Indian monsoon.

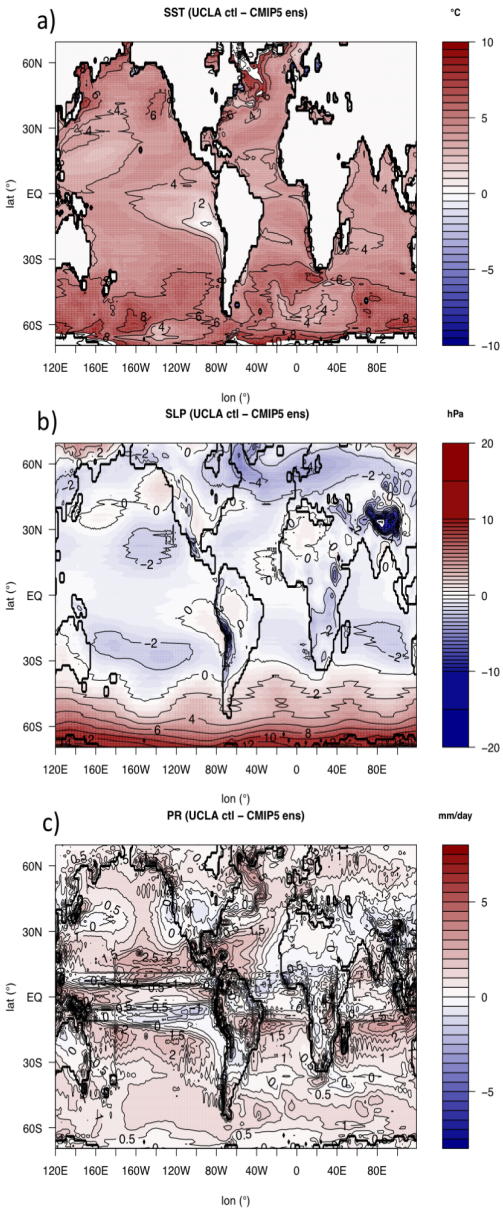

Figure 5.5: *Differences (UCLA control –CMIP5 mean) between UCLA control annual climatology (85 years) and CMIP5 ensemble mean annual climatology (100 years); for a) SST (°C), b) SLP (hPa) and c) pr (mm/day).*

5.1.4.1 NWA upwelling in UCLA with relation to CMIP5 intermodel variability

In order to characterize the representation of upwelling in the Northwest Africa (NWA) region in the UCLA control run when compared to the other 24 CMIP5 models, we repeat the EOF calculation as in Chapter 4, but including UCLA control in the models' dataset. The two first EOFs of the 25 models (CMIP5 24-model ensemble plus UCLA control) have been analyzed. The resulting patterns (Fig. 5.6) are very similar to those seen in Chapter 4: the first mode (EOF1), which explains 48% of intermodel variability, shows negative and significant loads for the northern half of the domain. Negative loads spread through all latitudes during winter and spring and are statistically significant north of 12.5°N. The second mode (EOF2) explains 19% of intermodel variability, is strongly seasonal and shows significantly negative values for summer in all the domain except the northernmost latitudes. What is important for this study is that values of PC1 and PC2 for the UCLA model help us characterize the performance of this model with respect to the other 24 CMIP5 one.

In PC1 UCLA shows the most negative value in the whole ensemble, which means that the Hovmöller of the deviation from the multimodel mean of the upwelling index is the opposite to the one shown in Fig. 5.6a, with approximately twice its magnitude. That is, the UCLA model shows a much weaker upwelling index than the mean of the ensemble, which explains why its bias is smaller than that of CMIP5. For PC2, however, UCLA's value is positive and not too strong, which means that the upwelling is weakened during the first half of the year, and reinforced during the second half, particularly in the south. According to the results from Chapter 4, this is consistent with a weakened monsoon, which in turn corresponds to an ITCZ located too far south.

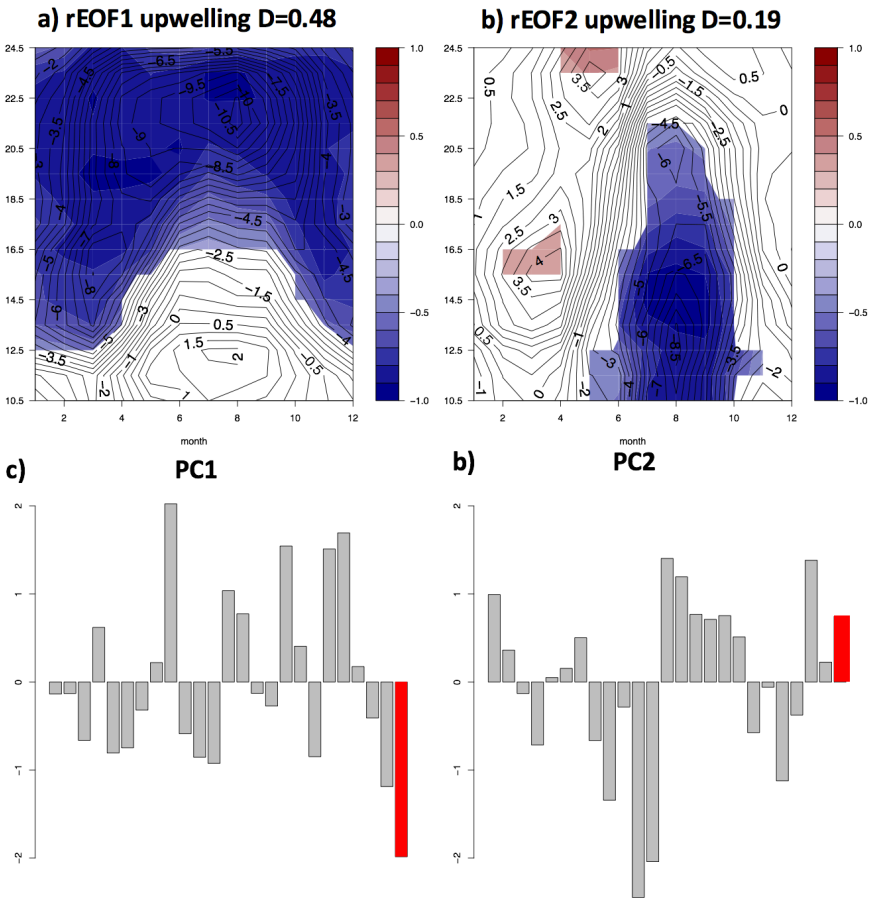

***Figure 5.6**: Study of the intermodel variability of the upwelling index for the CMIP5 24-model ensemble and the UCLA control run. a) First EOF of the upwelling index, with the region in which it is significant at the 90% value coloured (blue (red) means upwelling (downwelling) for models with positive (negative) PC1. b) Second EOF of the upwelling index. c) First Principal Component for each of the 24 CMIP5 ensemble models and UCLA control (in red). d) Second Principal Component for each of the 24 CMIP5 ensemble models and UCLA control (in red).*

To analyse the impact of ITCZ shifts in the NWA upwelling, in the following sections we will now focus on the COSZ sensitivity experiment used in Mechoso et al., (2016), which, as explained in the Data and Methodology

chapter, is an idealized experiment in which part of the incoming radiation in the Southern Ocean is removed.

5.2 Results of sensitivity experiment

The reduction of the SO incoming radiation in COSZ does not only lead to a diminished SST in that region, but also has remote consequences that were thoroughly described in Mechoso et al., 2016. In order to make this volume self-explained, we reproduce here some of the results shown there, regarding the changes in the general circulation observed in COSZ when compared to UCLA control (Fig. 5.7).

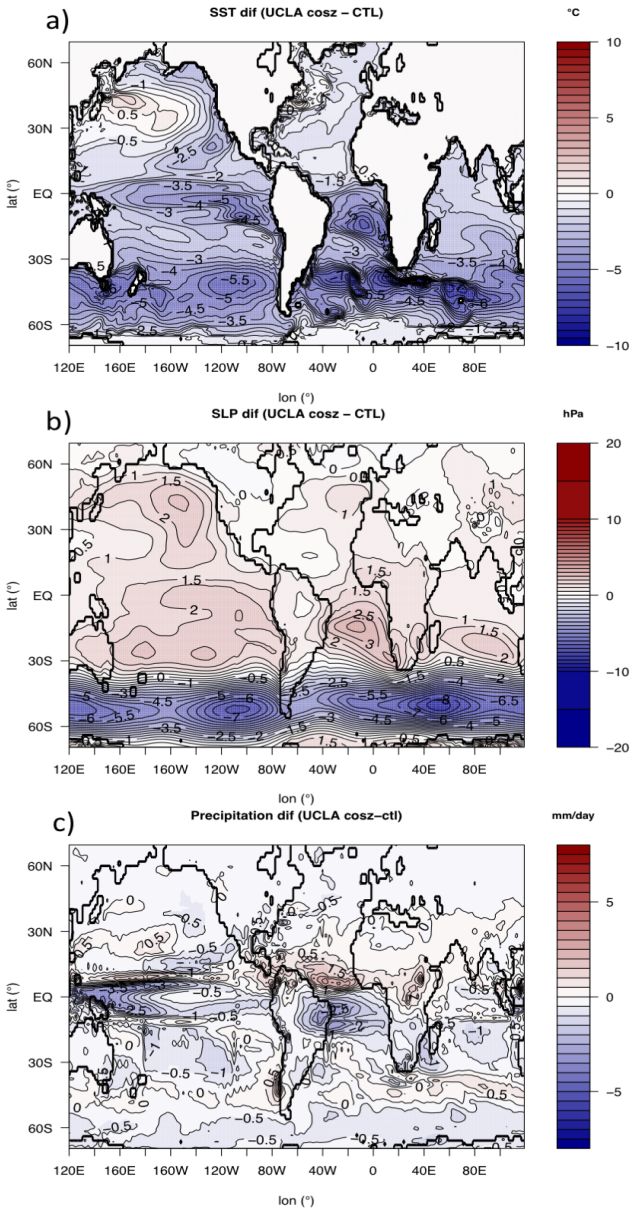

Figure 5.7: *Differences between UCLA COSZ annual climatology and UCLA control annual climatology for a) SST (°C), b) SLP (hPa) and c) precipitation (mm/day).*

The excessively high SST from control is greatly reduced in most of the globe, exceptions made for high latitudes in both hemispheres (Fig. 5.7a). The Southern Hemisphere cools more than the northern one, thus reducing the north-south SST gradient of the control. The COSZ run is still warmer than the CMIP5 average, but now the differences are not so big, and reach negative values in the upwelling regions of the Southern Hemisphere (not shown).

Regarding SLP (Fig. 5.7b), the subtropical highs are greatly reinforced in the Pacific and Southern Tropical Atlantic in comparison with the control experiment, pointing to a reinforcement of the Hadley circulation. Also, the pressure diminishes for the region in which the radiation correction has been applied.

One of the most interesting effects of the idealized experiment is observed in precipitation (Fig. 5.7c): The reduction of the incoming shortwave radiation in the Southern Ocean produces northward shift of the Atlantic ITCZ and a reduction of the Pacific double ITCZ (Fig 5.7c). This is consistent with the interhemispheric change in the SST (Fig. 5.7a).

Such changes are also consistent with a northward shift of the ascending branch of the Hadley cell, which can be interpreted as an adjustment of the Hadley circulation to transport less energy from the Southern Hemisphere to the northern one.

To sum up, in the COSZ experiment the difference in SST between both hemispheres is reduced, leading to a smaller northward energy transport in the atmosphere and therefore a northward shift of the ITCZ.

5.2.1 Representation of seasonal evolution of upwelling

In order to study the effects of the COSZ sensitivity experiment on the four variables chosen to characterise upwelling (upwelling index, SST, thermocline depth and maximum vertical gradient value), the COSZ Hovmöller plots have been represented for each of them (Fig. 5.8a), together

with their bias (Fig. 5.8b) and their difference with the UCLA control results (Fig. 5.8c).

The general structure of the upwelling Hovmöller is similar to that from UCLA control, although the maximum of upwelling between April and September above 20°N has intensified (Fig. 5.8a1 and 5.8a3), and now the bias in that region is even more negative (Fig. 5.8a2). For the rest of the domain, the upwelling index has been reduced, specially below 13°N, and in the monsoon season (June to October below 13°N) there is even more downwelling in COSZ than in UCLA control. This is consistent with the northward shift of the ITCZ in COSZ and with the strong cooling in the southeastern tropical Atlantic.

The SST field, however, has changed notably: the warm temperatures to the end of the year do not reach as far north as they did for the control run, and they occur later in the year (Fig. 5.8b1). In general, the whole field is much colder for all the domain, specially between July and October (Fig. 5.8b3). Together, the general cooling and the displacement of the warm temperatures towards the end of the year lead to the appearance of a cold bias north of 19°N from March to November, while the bias is still warm between December and February (Fig. 5.8b2).

The changes in SST are mimicked by changes in the thermocline depth: it is shallower in the northernmost region for the first months of the year (Fig. 5.8c3). However, and given that the value of the maximum gradient in that region has increased but is still much smaller than -0.1°C/m (Fig. 5.8d1), this only means that the water column is slightly more stratified, but still not as much as the reanalysis. It is also worth mentioning that in the region in which the SST has cooled more, the thermocline is slightly deeper (Fig. 5.8c3, August-September above 18°N), although again the value of the maximum gradient is too small for drawing conclusions from this.

As was shown in Section 5.1.2, for the UCLA model there is a correspondence between the upwelling index and the SST, contrary to what happened in the CMIP5 ensemble. Now this is even more evident: there is a very good

agreement between the regions in which there is a strong upwelling bias and those where there is a cold bias, and also where the upwelling bias is positive (too little upwelling), which leads to a too high SST (Fig. 5.8a2 and 5.8b2). This is possible due to the maximum gradient value being more realistic than it was in the CMIP5 ensemble.

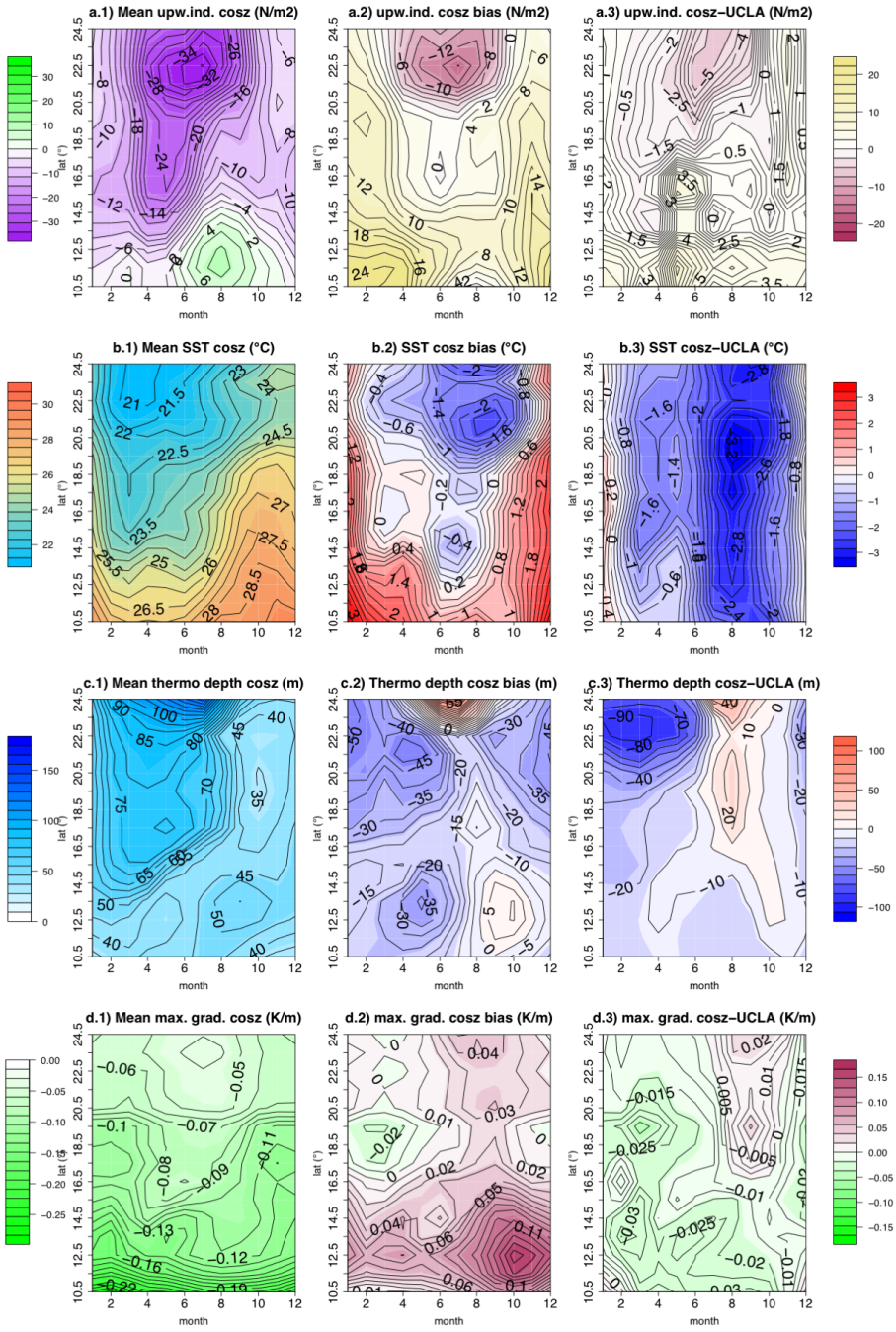
a.1) Mean upw.ind. cosz (N/m2)
a.2) upw.ind. cosz bias (N/m2)
a.3) upw.ind. cosz–UCLA (N/m2)
b.1) Mean SST cosz (°C)
b.2) SST cosz bias (°C)
b.3) SST cosz–UCLA (°C)
c.1) Mean thermo depth cosz (m)
c.2) Thermo depth cosz bias (m)
c.3) Thermo depth cosz–UCLA (m)
d.1) Mean max. grad. cosz (K/m)
d.2) max. grad. cosz bias (K/m)
d.3) max. grad. cosz–UCLA (K/m)
lat (°)
month

Figure 5.8: *Multimodel monthly climatology of upwelling variables (columns from left to right: UCLA COSZ experiment, UCLA COSZ bias, UCLA COSZ –UCLA control). a) upwelling index (N/m2); b) sea surface temperature (SST) (degrees Celsius); c) thermocline depth (m); d) thermal gradient at the thermocline level (K/m). Hovmöller plots computed from zonally averaging the variables between 20° W and 15° W for each latitude, and then computing the climatological monthly means.*

5.2.2 Vertical structure of ocean

As it has been shown in the previous sections, the reduction of radiation in the Southern Ocean affects the whole globe, and reduces SST for the whole region of study. Due to the relatively weak thermocline of the UCLA model, this has consequences in the vertical distribution of temperature (Fig. 5.9).

The difference between the COSZ profile and the control run at 15°N shows that the sub-surface temperature differences are even greater than those on the surface (Fig. 5.9a). There are, therefore, two main differences, apart from the overall cooling 1) the slightly retarded seasonal cycle of the upwelling and 2) the thinner mixed layer (Fig. 5.9c). There is still a seasonal upwelling between March and June, also delayed if we compare it with UCLA control or the CMIP5 mean behaviour.

Regarding the 23°N vertical profile, there is also a change in the seasonality of the upwelling, but in this case the maximum difference between COSZ and control are found in the deeper layers (Fig. 5.9b): The temperature bias of COSZ changes from slightly positive in the surface to negative below 140 meters of depth (not shown). This makes UCLA COSZ colder than SODA for depths below 200 metres, and has implications for any studies that would consider the heat content of the whole water column (if the temperature bias changes sign with depth, the bias at the surface might not be representative of the whole ocean extent).

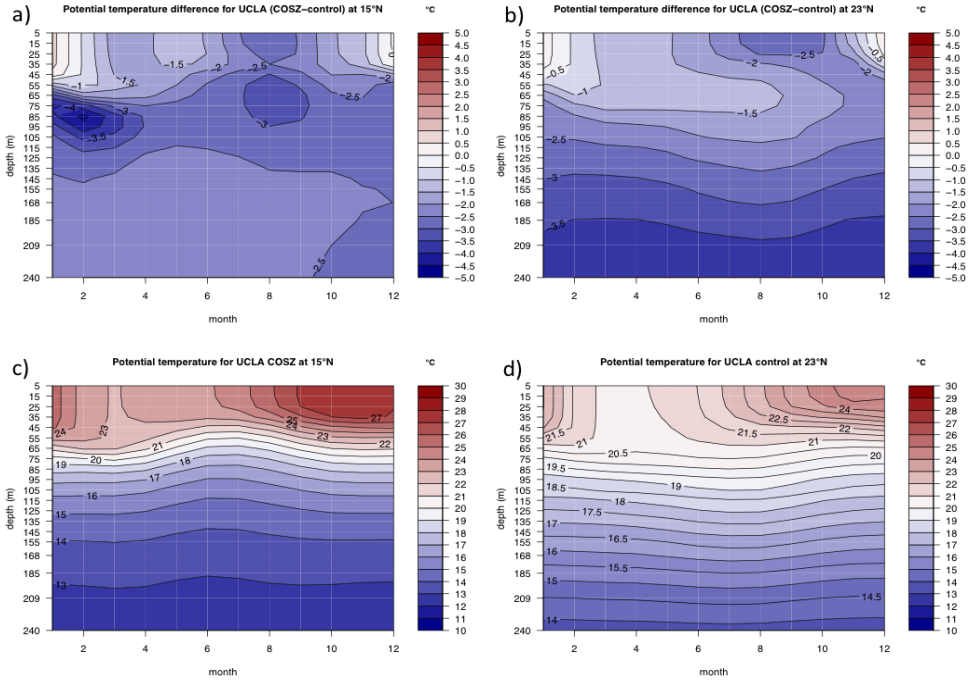

***Figure 5.9**: Ocean potential temperature Hovmöller diagram for UCLA COSZ - UCLA control differences (top row) at 15° N (a) and 2° 3N (b) and UCLA COSZ run (bottom row) at 15° N (c) and 23° N (d). Hovmöller plots computed from zonally averaging the variables between 20° W and 15° W for each latitude and depth, and then computing the climatological monthly means.*

5.2.3 NWA upwelling in relation to CMIP5 intermodel variability

The same EOF calculation as for the control run has been performed, but this time using the 24-model CMIP5 ensemble and the UCLA COSZ (Fig. 5.10). The results are very similar to what was shown in Fig. 5.4. The patterns of EOF1 (Fig. 5.10a) and EOF2 (Fig. 5.10b) change very little when using UCLA COSZ instead of UCLA control, and they explain the same fraction of intermodel variance (48% for EOF1 and 19% for EOF2). The main changes are a slight intensification of the first mode around the maximum at 22°N in

August and, for the second mode, also an intensification of the positive local maximum at 23°N in June. The value of the PC1 for UCLA COSZ is almost the same as it was for UCLA control (Fig. 5.10c). However, there is a more appreciable change in the value of PC2 for UCLA COSZ (Fig. 5.10d). Its value is half what it was for UCLA control, explaining why the upwelling is weaker during summer and early autumn in the southern half of the region, and a bit stronger in the northern latitudes (22.5°N-24°N) in around June, as shown in section 5.2.1.

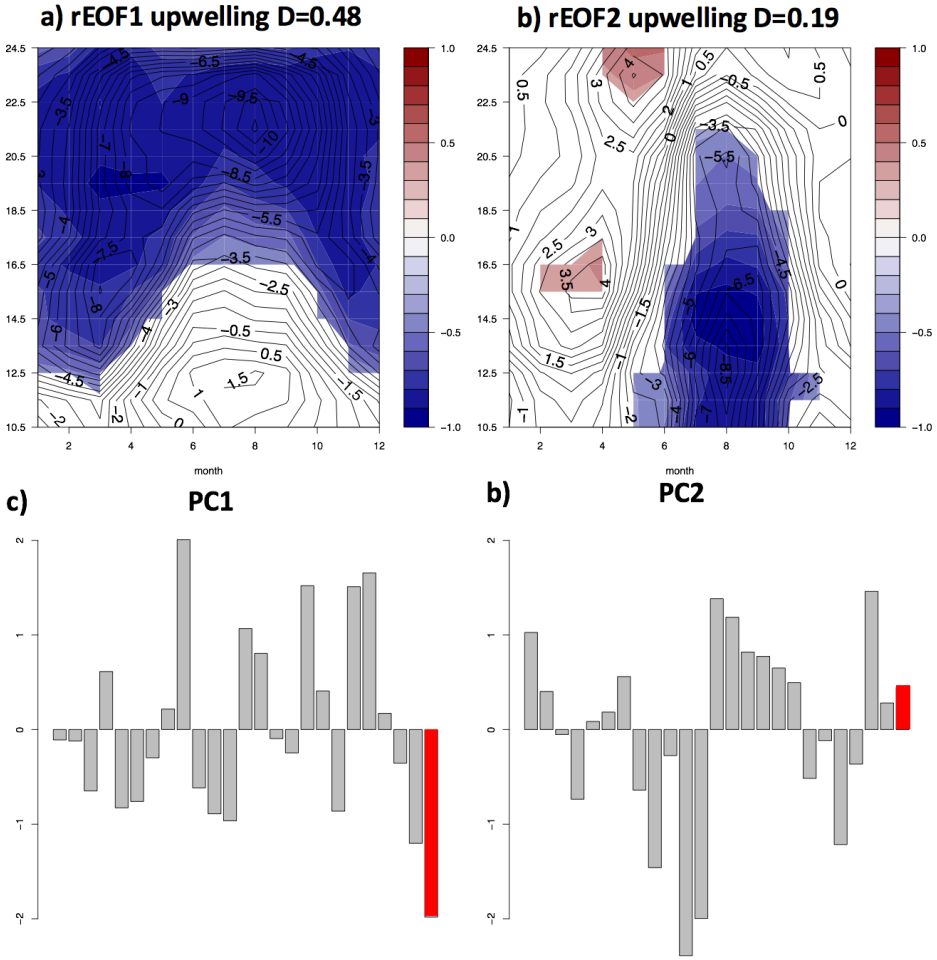

Figure 5.10: *Study of the intermodel variability of the upwelling index for the CMIP5 24-model ensemble and the UCLA COSZ sensitivity experiment: a) First EOF of the upwelling index, with the region in which it is significant at the 90% value coloured (blue (red) means upwelling (downwelling) for models with positive (negative) PC1. b) Second EOF of the upwelling index. c) First Principal Component for each of the 24 CMIP5 ensemble models and UCLA control (in red). d) Second Principal Component for each of the 24 CMIP5 ensemble models and UCLA control (in red).*

Results from this section indicate that the reduction of the incoming shortwave raditation over the Southern Ocean has an impact in the NWA Atlantic region that translates into a stronger upwelling index in spring and a reduction of it in summer. Analysis of CMIP5 simulations in Chapter 4 lead to the hypothesis that changes in the ITCZ position in COSZ are responsible for this result, through changes in the SLP gradients.

The effects of this ITCZ shift in the atmospheric circulation are better explored through seasonal plots, parallel to what was done in Fig. 4.11a1 and 4.11b1 in Chapter 4. The SLP variation induced in the North Atlantic when applying the radiation reduction changes from April (Fig. 5.11a) to August (Fig. 5.11b). In spring, the SLP rises over the whole upwelling region, while it diminishes slightly over the centre of the Northern Atlantic Subtropical gyre. This results in a reduction of northerly winds and therefore an inhibition of upwelling.

During summer, however, the effects are not the same for all the domain. In the northern part, there is a reinforcement of the Azores anticyclone, while there is only a slight change in the pressure over Africa. This leads to a land-sea pressure gradient which channels northerly winds along the coast, thus increasing upwelling. In the south, the land-sea SLP contrast has the opposite sign, inhibiting northerly winds and, again, reducing the upwelling.

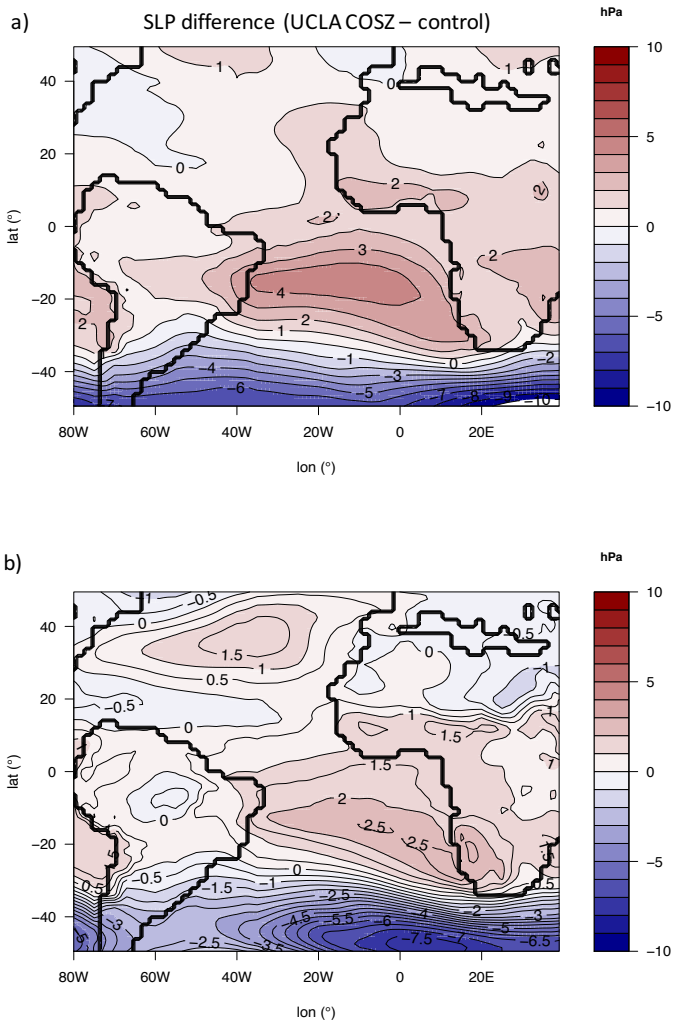

***Figure 5.11**: Differences between UCLA COSZ SLP (hPa) climatology and UCLA control SLP climatology for April-May (top) and July-August (bottom).*

5.3 Discussion and conclusions

Using the UCLA coupled general circulation model has allowed to delve into some of the questions posed in Chapter 4 of this thesis, and also to solve one of the research questions that remained open at the end of that chapter. First of all, it has been shown that representing the ocean stratification and the thermocline strength correctly is fundamental for the surface winds stress (upwelling index) to affect the subsurface dynamics and thus the SST climatology. This has been shown both for the control run and the COSZ experiment. Comparing the results of this chapter to those obtained previously for the CMIP5 ensemble, it seems clear that, as posited by Guilyardi (2009) and Richter (2015), it is very difficult for a model to correctly represent atmosphere-ocean coupled processes if its thermocline depth and strength is not realistic. Furthermore, a badly simulated thermocline can lead to errors in bias assessment: assumptions such as that models with a warm SST bias must have warm ocean biases are not necessarily true if the thermocline is too strong. Conversely, it seems within reason that models with weak thermoclines will be overly sensitive to thermodynamic processes in detriment of dynamical ones, as they would allow atmosphere influence to reach deeper in the ocean (Wang and Wang 2013).

Second, the correction introduced via the reduced radiation in the Southern Ocean has important consequences in upwelling representation. Firstly, by reducing the very strong warm model SST bias (Mechoso et al., 2016). This reduction does not only affect the surface, but propagates downward, cooling the whole water column and making for a much more realistic ocean temperature representation. Secondly, the cooling of the Southern Ocean leads to a reduced interhemispheric temperature gradient, and therefore to a northward shift of the ITCZ (Mechoso et al., 2016; Hwang and Frierson, 2013). In chapter 4, a correlation was found between high SSTs in the Southern Hemisphere (although not in the exact same region of the COSZ experiment) and models with increased upwelling in the southern half of the NWA domain, due to changes in the alongshore winds driven by changes in the ITCZ position. Such mechanisms appear at work in the COSZ

experiment, in which the reduction of upwelling for the southern half of NWA is consistent with the findings of chapter 4.

The mechanisms that dominate NWA upwelling are, therefore, those proposed by Bakun (1990) and mentioned in the Introduction to this thesis: 1) subtropical anticyclones, and their intensification/weakening and 2) land-sea temperature contrasts (which drive SLP contrasts and therefore winds). His study focused on how the upwelling system would react to a global warming that would intensify anticyclones and land-sea temperature contrasts. In this work the land-sea temperature contrast has not been intensified, but the northward shift of the ITCZ due to a cooling of the Southern Hemisphere could be compared, at least in its effects on the energy balance, to a warming on the Northern Hemisphere, which is already underway (IPCC, 2014). Therefore, studying the reaction of the upwelling index to a simple idealized model could give us clues about what future climate change could entail for the NWA upwelling system.

6 Conclusions and outlook

The goal of this thesis was to contribute to the knowledge of the atmosphere-ocean coupling in the tropics, with a focus on wind-forced ocean processes. In particular, the present work has shed light on the behaviour of the equatorial thermocline and the Northwest African coastal upwelling. The results concern both reanalysis and coupled model data, and are of special interest for the community of coupled-model users.

Properly assessing the location and seasonal cycle of the equatorial thermocline, whose position controls the amount of heat content stored in the upper layer of the ocean, is of the utmost importance for the correct representation of tropical variability phenomena. Among these, El Niño-Southern Oscillation is the most remarkable one. Multiple studies have put forward that the configuration of the thermocline conditions the flavour of El Niño that can develops, and thus its global impacts (Xu et al., 2017). Nevertheless, the thermocline depth has long been estimated as the depth of the 20°C isotherm (z20), which was chosen for observations rather than for coupled models (Lengaigne et al., 2012; Li and Xie, 2014). In the first part of this thesis the validity of the z20 estimate is in SODA reanalysis and 24 CMIP5 models has been put to the test and its climatology and seasonal cycle compared to that of the thermocline depth. The results are as follows:

- z20 is systematically deeper than the thermocline in reanalysis and models both in the Atlantic and Pacific equatorial basins. Even in the regions in which the climatology of z20 compares relatively well to the depth of the thermocline, the seasonal cycle is not well represented by this estimate.

- A link is found between z20 and SST in the eastern equatorial Pacific, which is not true for the thermocline depth and SST. This casts doubts on studies that establish a relation between the depth of the thermocline and model thermal bias, in particular with relation to the double ITCZ problem.

- There is a disconnection between the ocean model and the atmosphere model. The behaviour of the subsurface of the ocean,

where the thermocline lays, depends on internal ocean dynamics, and not on SST. The greater intensity of vertical thermal gradient in models than in reanalysis supports this hypothesis.

- z20 is biased when used to explain the atmosphere-ocean interactions. It shows a lack of connection with the atmosphere in the western equatorial Pacific, especially regarding the part of dynamics mediated by zonal wind stress, which has very little effect on z20. Also, this estimate is more dependent on extratropical equatorward Sverdrup transport than the thermocline depth.

- In the Atlantic Ocean, the seasonal cycle of z20 shows smaller amplitude than the thermocline's one (and is much weaker in some particular models such as CanESM2 and GISS-E2-H). This seems linked to the lack of response of z20 to zonal equatorial winds. The results are valid for other representative isotherms, such as z23, which points to the general problems inherent to using isotherms as estimate of the thermocline in coupled models.

To sum up, the results reached in this first part of the thesis point to the need of revising the conclusions of studies that use z20 as an estimate for the thermocline depth, in particular those that draw conclusions from the relation between thermocline depth and sea surface temperature in the eastern Pacific basin and from extratropical forcings in the Atlantic Ocean.

Another relevant feature of tropical wind-driven circulation are the four eastern boundary upwelling regions: Angola-Benguela, California, Canary and Peru. In these regions, the prevailing meridional wind push surface water out of the coast, causing it to be replaced for colder, nutrient-rich water from the deeps. Studying these regions with coupled models allows to explore their possible future behaviour, but also to discern which large scale features of models influence coastal upwelling. The second part of this thesis has focused on studying, in both reanalysis and coupled models, the seasonal cycle of the Northwest African upwelling, a subregion of the Canary Upwelling Region located between 10°N and 25°N. It must be made a note that the estimate of upwelling used in this thesis is only dependent on the surface wind (Ekman

transport). There are other magnitudes that impact upwelling (vertical entrainment, coastal morphology, non-meridional wind stress), but the wind regime along the NWA coast is the most relevant.

The main results are:

- The seasonal cycle of NWA upwelling is qualitatively well simulated by CMIP5 models although models tend to show strong biases for the permanent upwelling latitudes (north of 20°N) and the seasonal upwelling area (around 15°N in boreal spring). There is also a strong bias below 15°N between June and September, when the climatological winds change sign due to West African monsoon.

- The maximum vertical temperature gradient shown by CMIP5 models is higher than that of SODA reanalysis and prevents cold water from deeper layers to reach the surface, thus making coastal upwelling less effective in affecting sea surface temperatures.

- The upwelling seasonal cycle shows the highest intermodel spread over the permanent upwelling region. It also shows two secondary maxima in the southern part of the domain, one in spring and the other at the monsoon season. Most of this intermodel variance is explained by the two first EOF modes of intermodel variability (68%). The first mode (47% of variance explained) shows a latitudinal structure (is significant and negative –stronger upwelling- for positive PC1 values above 15°N), with a maximum in the permanent upwelling season. The second mode explains 21% of variance and is more seasonal. It is significant and negative (for positive PC2 values) in the second half of the year and below 20°N, and positive but little significant in the first half of the year.

- Both modes are very related to changes in the North-West Africa land-sea surface pressure gradient, which drive changes in alongshore winds which, in turn, force upwelling variability.

- In the case of the leading mode, incoming solar radiation differences between the North African desert and the ocean are the cause of the

pressure gradients, via a weakening of the downward branch of the Hadley cell over North Africa, which does not happen over the Atlantic Ocean.

- The second mode shows more seasonality, and pressure changes in the Atlantic Ocean are driven by ITCZ shifts which responds to interhemispheric differential warming. Models with a too warm Southern Hemisphere show a southward-shifted ITCZ, which leads to excessive uwelling during boreal summer.

The results obtained in the intercomparison study of CMIP5 models allow us to conclude that coupled models are able to reproduce the NWA upwelling seasonal cycle, although they show strong biases. Also that there are large-scale features in coupled models that affect their ability to correctly simulate upwelling in the subtropical North Atlantic. In particular, it is known that CMIP5 models suffer from a warm bias in the Southern Ocean, which has been the subject of much interest in recent years, due to its possible influence on the whole globe, in particular to ITCZ shifts (Mechoso et al., 2016; Kang et al. 2009). The results for the second mode suggest such shifts would impact NWA upwelling representation.

To test this hypothesis , the UCLA CGCM model has been used. to perform a sensitivity experiment in which the Southern Ocean is artificially cooled via a reduction in the incoming shortwave radiation at the top of the atmosphere, resulting in a northward shift of the ITCZ. The results from the evaluation of this experiment in comparison with a control run are as follows:

- The UCLA control simulation shows smaller bias in the upwelling than the CMIP5 ensemble, with generally weaker northerly winds, but also with more downwelling bias during the West African monsoon season.

- The seasonal cycle of SST follows better that of the upwelling in UCLA model than in the CMIP5 models. This seems to be related to the thermocline being weaker than in other coupled models and more similar to the reanalysis.

- The results of the idealized sensitivity experiment show a northward shift of the ITCZ that leads to stronger upwelling in the north of the NWA region, and stronger downwelling in the south, via changes in the intensity and location of the subtropical high pressure systems.

Overall, results from the two chapters concerned with the NWA upwelling point to the ability of coupled models to capture the overall behaviour of coastal upwelling. However, some considerations must be highlighted: 1) intermodel variability depends not only on local features, but also on remote influences which condition the ability of coupled models to accurately represent upwelling; 2) ocean stratification is fundamental for the upwelling to effectively draw cold water towards the ocean surface.

FUTURE WORK

This thesis has contributed to advance in the understanding of some of the processes that drive atmosphere-ocean coupling. Its results open lines of research regarding tropical atmosphere-ocean coupling and upwelling representation such as:

- More thorough studies of the variability of the thermocline depth at various timescales could be conducted. A distinct possibility is to explore the impact of teleconnections between tropical basins, such as the ENSO-Tropical Atlantic teleconnection, using the definition of the physical thermocline instead of z20.

- The work carried out in Chapter 4 could be extended to the other three big eastern boundary systems: Angola-Benguela, California and Peru, in order to explore common features of remote bias influence on all or part of them.

- Lastly, the results from Chapter 5 regarding the importance of thermocline strength in terms of the value of the vertical gradient, for vertical entrainment in upwelling systems call for a more detailed study of what features of ocean models are responsible for vertical stratification below the mixed layer. This, in turn, could be followed by an analysis of how do models with a weaker thermocline represent dynamic processes such as Bjerknes feedback.

References

Adler, R. F., Huffman, G. J., Chang, A., Ferraro, R., Xie, P. P., Janowiak, J., ... & Gruber, A. (2003). The version-2 global precipitation climatology project (GPCP) monthly precipitation analysis (1979–present). *Journal of hydrometeorology*, *4*(6), 1147-1167.

Alder, J., & Sumaila, U. R. (2004). Western Africa: a fish basket of Europe past and present. *The Journal of Environment & Development*, *13*(2), 156-178.

Alexander, M. A., Bladé, I., Newman, M., Lanzante, J. R., Lau, N. C., & Scott, J. D. (2002). The atmospheric bridge: The influence of ENSO teleconnections on air–sea interaction over the global oceans. *Journal of Climate*, *15*(16), 2205-2231.

Allan, R., & Ansell, T. (2006). A new globally complete monthly historical gridded mean sea level pressure dataset (HadSLP2): 1850–2004. *Journal of Climate*, *19*(22), 5816-5842.

Bakun, A. (1990). Global climate change and intensification of coastal ocean upwelling. *Science*, *247*(4939), 198-201.

Bakun, A., (1973). Coastal upwelling indices, west coast of North America, 1946-71. U.S.Dep. Commer., NOAA Tech. Rep., NMFS SSRF-671, 103 p.

Barton, E. D., Field, D. B., & Roy, C. (2013). Canary current upwelling: More or less?. *Progress in Oceanography*, *116*, 167-178.

Basnett, T. and Parker, D. (1997) 'Development of the Global Mean Sea Level Pressure Data Set GMSLP2', Climate Research Technical Note, 79, Hadley Centre, Met Office, FitzRoy Rd, Exeter, Devon, EX1 3PB, UK

Bellucci, A., Gualdi, S., & Navarra, A. (2010). The double-ITCZ syndrome in coupled general circulation models: the role of large-scale vertical circulation regimes. *Journal of Climate*, *23*(5), 1127-1145.

Benazzouz, A., Mordane, S., Orbi, A., Chagdali, M., Hilmi, K., Atillah, A., ... & Hervé, D. (2014). An improved coastal upwelling index from sea surface temperature using satellite-based approach–The case of the Canary Current upwelling system. *Continental Shelf Research*, *81*, 38-54.

Bjerknes, J. (1969). Atmospheric teleconnections from the equatorial Pacific. *Monthly weather review*, *97*(3), 163-172.

Breugem, W. P., Chang, P., Jang, C. J., Mignot, J., & Hazeleger, W. (2008). Barrier layers and tropical Atlantic SST biases in coupled GCMs. *Tellus A: Dynamic Meteorology and Oceanography*, *60*(5), 885-897.

Cabos, W., Sein, D. V., Pinto, J. G., Fink, A. H., Koldunov, N. V., Alvarez, F., ... & Jacob, D. (2017). The South Atlantic Anticyclone as a key player for the representation of the tropical Atlantic climate in coupled climate models. *Climate Dynamics*, *48*(11-12), 4051-4069.

Cai, W., McPhaden, M. J., & Collier, M. A. (2004). Multidecadal fluctuations in the relationship between equatorial Pacific heat content anomalies and ENSO amplitude. *Geophysical research letters*, *31*(1).

Caniaux, G., Giordani, H., Redelsperger, J. L., Guichard, F., Key, E., & Wade, M. (2011). Coupling between the Atlantic cold tongue and the West African monsoon in boreal spring and summer. *Journal of Geophysical Research: Oceans*, *116*(C4).

Carton, J. A., Giese, B. S., & Grodsky, S. A. (2005). Sea level rise and the warming of the oceans in the Simple Ocean Data Assimilation (SODA) ocean reanalysis. *Journal of Geophysical Research: Oceans*, *110*(C9).

Castaño-Tierno, A., Mohino, E., Rodríguez-Fonseca, B., & Losada, T. (2018). Revisiting the CMIP5 Thermocline in the Equatorial Pacific and Atlantic Oceans. *Geophysical Research Letters*, *45*(23), 12-963.

Deppenmeier, A. L., Haarsma, R. J., & Hazeleger, W. (2016). The Bjerknes feedback in the tropical Atlantic in CMIP5 models. *Climate Dynamics*, *47*(7-8), 2691-2707.

Ding, H., Greatbatch, R. J., Latif, M., & Park, W. (2015). The impact of sea surface temperature bias on equatorial Atlantic interannual variability in partially coupled model experiments. *Geophysical Research Letters*, *42*(13), 5540-5546.

Dippe, T., Greatbatch, R. J., & Ding, H. (2018). On the relationship between Atlantic Niño variability and ocean dynamics. *Climate dynamics*, 1-16.

Dommenget, D. and Vijayeta, A. (2019). Simulated future changes in ENSO dynamics in the framework of the linear recharge oscillator model. *Climate Dynamics*, 1432-0894.

Dugdale, R. C. (1972). Chemical oceanography and primary productivity in upwelling regions. *Geoforum*, *3*(3), 47-61.

Ekman, V. W. (1905). On the influence of the earth's rotation on ocean-currents.

Estrade, P., Marchesiello, P., Verdière, D., Colin, A., & Roy, C. (2008). Cross-shelf structure of coastal upwelling: A two—dimensional extension of Ekman's theory and a mechanism for inner shelf upwelling shut down. *Journal of marine research*, *66*(5), 589-616.

Fiedler, P. C. (2010). Comparison of objective descriptions of the thermocline. *Limnology and Oceanography: Methods*, *8*(6), 313-325.

Field, J. G., Griffiths, C. L., Linley, E. A., Carter, R. A., & Zoutendyk, P. (1980). Upwelling in a nearshore marine ecosystem and its biological implications. *Estuarine and Coastal Marine Science*, *11*(2), 133-150.

Flato, G., Marotzke, J., Abiodun, B., Braconnot, P., Chou, S. C., Collins, W., ... & Forest, C. (2014). Evaluation of climate models. In *Climate change 2013: the physical science basis. Contribution of Working Group I to the Fifth Assessment Report of the Intergovernmental Panel on Climate Change* (pp. 741-866). Cambridge University Press.

Gonzalez-Nuevo, G., Gago, J., & Cabanas, J. M. (2014). Upwelling index: a powerful tool for marine research in the NW Iberian upwelling system. *Journal of Operational Oceanography*, *7*(1), 47-57.

Gordon, H. B., O'Farrell, S., Collier, M., Dix, M., Rotstayn, L., Kowalczyk, E., ... & Watterson, I. (2010). *The CSIRO Mk3. 5 climate model* (p. 74). CSIRO and Bureau of Meteorology.

Gu, D., & Philander, S. G. (1997). Interdecadal climate fluctuations that depend on exchanges between the tropics and extratropics. *Science*, *275*(5301), 805-807.

Guilyardi, E., Wittenberg, A., Fedorov, A., Collins, M., Wang, C., Capotondi, A., ... & Stockdale, T. (2009). Understanding El Niño in ocean–atmosphere general circulation models: Progress and challenges. *Bulletin of the American Meteorological Society*, *90*(3), 325-340.

Hadley, G. (1735). VI. Concerning the cause of the general trade-winds. *Philosophical Transactions of the Royal Society of London*, *39*(437), 58-62.

Hartmann, D. L. (2015). *Global physical climatology* (Vol. 103). Newnes.

Holton, J. R. (1973). An introduction to dynamic meteorology. *American Journal of Physics*, *41*(5), 752-754.

Hotelling, H. (1992). Relations between two sets of variates. In *Breakthroughs in statistics* (pp. 162-190). Springer, New York, NY.

Hourdin, F., Găinusă-Bogdan, A., Braconnot, P., Dufresne, J. L., Traore, A. K., & Rio, C. (2015). Air moisture control on ocean surface temperature, hidden key to the warm bias enigma. *Geophysical Research Letters*, *42*(24), 10-885.

Hwang, Y. T., & Frierson, D. M. (2013). Link between the double-Intertropical Convergence Zone problem and cloud biases over the Southern Ocean. *Proceedings of the National Academy of Sciences*, *110*(13), 4935-4940.

Iles, A. C., Gouhier, T. C., Menge, B. A., Stewart, J. S., Haupt, A. J., & Lynch, M. C. (2012). Climate-driven trends and ecological implications of event-scale upwelling in the California Current S ystem. *Global Change Biology*, *18*(2), 783-796.

Jin, F. F. (1997). An equatorial ocean recharge paradigm for ENSO. Part I: Conceptual model. *Journal of the atmospheric sciences*, *54*(7), 811-829.

Kang, S. M., Frierson, D. M., & Held, I. M. (2009). The tropical response to extratropical thermal forcing in an idealized GCM: The importance of radiative feedbacks and convective parameterization. *Journal of the atmospheric sciences*, *66*(9), 2812-2827.

Kang, S. M., Held, I. M., Frierson, D. M., & Zhao, M. (2008). The response of the ITCZ to extratropical thermal forcing: Idealized slab-ocean experiments with a GCM. *Journal of Climate*, *21*(14), 3521-3532.

Kao, H. Y., & Yu, J. Y. (2009). Contrasting eastern-Pacific and central-Pacific types of ENSO. *Journal of Climate*, *22*(3), 615-632.

Kay, J. E., Wall, C., Yettella, V., Medeiros, B., Hannay, C., Caldwell, P., & Bitz, C. (2016). Global climate impacts of fixing the Southern Ocean shortwave radiation bias in the Community Earth System Model (CESM). *Journal of Climate*, *29*(12), 4617-4636.

Kessler, W. S. (1990). Observations of long Rossby waves in the northern tropical Pacific. *Journal of Geophysical Research: Oceans*, *95*(C4), 5183-5217.

Kug, J. S., Jin, F. F., & An, S. I. (2009). Two types of El Niño events: cold tongue El Niño and warm pool El Niño. *Journal of Climate*, *22*(6), 1499-1515.

Lengaigne, M., Hausmann, U., Madec, G., Menkès, C., Vialard, J., & Molines, J. M. (2012). Mechanisms controlling warm water volume interannual variations in the equatorial Pacific: diabatic versus adiabatic processes. *Climate Dynamics*, *38*(5-6), 1031-1046.

Levitus, S. (1982). Climatological atlas of the world ocean. *NOAA Profess. Pap.*, *13*, 1-173.

Li, G., & Xie, S. P. (2012). Origins of tropical-wide SST biases in CMIP multi-model ensembles. *Geophysical Research Letters*, *39*(22).

Li, G., & Xie, S. P. (2014). Tropical biases in CMIP5 multimodel ensemble: The excessive equatorial Pacific cold tongue and double ITCZ problems. *Journal of Climate*, *27*(4), 1765-1780.

Li, G., Du, Y., Xu, H., & Ren, B. (2015). An intermodel approach to identify the source of excessive equatorial Pacific cold tongue in CMIP5 models and uncertainty in observational datasets. *Journal of Climate*, *28*(19), 7630-7640.

Li, G., Xie, S. P., Du, Y., & Luo, Y. (2016). Effects of excessive equatorial cold tongue bias on the projections of tropical Pacific climate change. Part I: The warming pattern in CMIP5 multi-model ensemble. *Climate dynamics*, *47*(12), 3817-3831.

Lipat, B. R., Tselioudis, G., Grise, K. M., & Polvani, L. M. (2017). CMIP5 models' shortwave cloud radiative response and climate sensitivity linked to the climatological Hadley cell extent. *Geophysical Research Letters*, *44*(11), 5739-5748.

Lorenz, E. N. (1956). Empirical orthogonal functions and statistical weather prediction. Massachusetts Institute of Technology.

Lübbecke, J. F., & McPhaden, M. J. (2017). Symmetry of the Atlantic Niño mode. *Geophysical Research Letters*, *44*(2), 965-973.

Ma, H. Y., Xiao, H., Mechoso, C. R., & Xue, Y. (2013). Sensitivity of global tropical climate to land surface processes: Mean state and interannual variability. *Journal of Climate*, *26*(5), 1818-1837.

Marshall, J., Adcroft, A., Hill, C., Perelman, L., & Heisey, C. (1997). A finite-volume, incompressible Navier Stokes model for studies of the ocean on parallel computers. *Journal of Geophysical Research: Oceans*, *102*(C3), 5753-5766.

Marshall, J., Jones, H., Karsten, R., & Wardle, R. (2002). Can eddies set ocean stratification?. *Journal of physical oceanography*, *32*(1), 26-38.

Martín-Rey, M., Rodríguez-Fonseca, B., Polo, I., & Kucharski, F. (2014). On the Atlantic–Pacific Niños connection: a multidecadal modulated mode. *Climate dynamics*, *43*(11), 3163-3178.

Mbaye, B. C., Brochier, T., Echevin, V., Lazar, A., Lévy, M., Mason, E., ... & Machu, E. (2015). Do Sardinella aurita spawning seasons

match local retention patterns in the Senegalese–Mauritanian upwelling region?. *Fisheries Oceanography*, *24*(1), 69-89.

McGregor, H. V., Dima, M., Fischer, H. W., & Mulitza, S. (2007). Rapid 20th-century increase in coastal upwelling off northwest Africa. *science*, *315*(5812), 637-639.

McPhaden, M. J., Zebiak, S. E., & Glantz, M. H. (2006). ENSO as an integrating concept in earth science. *science*, *314*(5806), 1740-1745.

Mechoso, C. R. (2000). A coupled GCM pilgrimage: From climate catastrophe to ENSO simulations. In *General Circulation Model Development: Past, present and future. Proceedings of a Symposium in Honor of Professor Akio Arakawa, 2000*. Academic Press.

Mechoso, C. R., Losada, T., Koseki, S., Mohino-Harris, E., Keenlyside, N., Castaño-Tierno, A., ... & Toniazzo, T. (2016). Can reducing the incoming energy flux over the Southern Ocean in a CGCM improve its simulation of tropical climate?. *Geophysical Research Letters*, *43*(20), 11-057.

Mignot, J., Lazar, A., & Lacarra, M. (2012). On the formation of barrier layers and associated vertical temperature inversions: A focus on the northwestern tropical Atlantic. *Journal of Geophysical Research: Oceans*, *117*(C2).

Mohino, E., Rodríguez-Fonseca, B., Mechoso, C. R., Losada, T., & Polo, I. (2019). Relationships among Intermodel Spread and Biases in Tropical Atlantic Sea Surface Temperatures. *Journal of Climate*, *32*(12), 3615-3635.

Mote, P. W., & Mantua, N. J. (2002). Coastal upwelling in a warmer future. *Geophysical research letters*, *29*(23), 53-1.

Narayan, N., Paul, A., Mulitza, S., & Schulz, M. (2010). Trends in coastal upwelling intensity during the late 20th century. *Ocean Science*, *6*(3), 815-823.

Nnamchi, H. C., Li, J., Kucharski, F., Kang, I. S., Keenlyside, N. S., Chang, P., & Farneti, R. (2015). Thermodynamic controls of the Atlantic Niño. *Nature communications*, *6*, 8895.

Orr, J. C., Fabry, V. J., Aumont, O., Bopp, L., Doney, S. C., Feely, R. A., ... & Key, R. M. (2005). Anthropogenic ocean acidification over the twenty-first century and its impact on calcifying organisms. *Nature*, *437*(7059), 681.

Oueslati, B., & Bellon, G. (2015). The double ITCZ bias in CMIP5 models: interaction between SST, large-scale circulation and precipitation. *Climate dynamics*, *44*(3-4), 585-607.

Pauly, D., & Christensen, V. (1995). Primary production required to sustain global fisheries. *Nature*, *374*(6519), 255.

Pedlosky, J. (1987). Thermocline theories. In *General Circulation of the Ocean* (pp. 55-101). Springer, New York, NY.

Peter, A. C., Le Hénaff, M., Du Penhoat, Y., Menkes, C. E., Marin, F., Vialard, J., ... & Lazar, A. (2006). A model study of the seasonal mixed layer heat budget in the equatorial Atlantic. *Journal of Geophysical Research: Oceans*, *111*(C6).

Polo, I., Lazar, A., Rodriguez-Fonseca, B., & Mignot, J. (2015). Growth and decay of the equatorial Atlantic SST mode by means of closed heat budget in a coupled general circulation model. *Frontiers in Earth Science*, *3*, 37.

Ren, H. L., & Jin, F. F. (2013). Recharge oscillator mechanisms in two types of ENSO. *Journal of Climate*, *26*(17), 6506-6523.

Richter, I. (2015). Climate model biases in the eastern tropical oceans: Causes, impacts and ways forward. *Wiley Interdisciplinary Reviews: Climate Change*, *6*(3), 345-358.

Richter, I., Xie, S. P., Behera, S. K., Doi, T., & Masumoto, Y. (2014). Equatorial Atlantic variability and its relation to mean state biases in CMIP5. *Climate dynamics*, *42*(1-2), 171-188.

Rodríguez-Fonseca, B. (2001). *Relacion entre el regimen anomalo de precipitacion en la peninsula iberica y la variabilidad de baja frecuencia del sistema climatico en el atlantico norte* (Doctoral dissertation, Universidad Complutense de Madrid).

Santos, A. M. P., Kazmin, A. S., & Peliz, A. (2005). Decadal changes in the Canary upwelling system as revealed by satellite observations:

Their impact on productivity. *Journal of Marine Research*, *63*(2), 359-379.

Santos, F., Gomez-Gesteira, M., Decastro, M., & Alvarez, I. (2012). Differences in coastal and oceanic SST trends due to the strengthening of coastal upwelling along the Benguela current system. *Continental Shelf Research*, *34*, 79-86.

Schneider, T., Bischoff, T., & Haug, G. H. (2014). Migrations and dynamics of the intertropical convergence zone. *Nature*, *513*(7516), 45.

Small, R. J., Curchitser, E., Hedstrom, K., Kauffman, B., & Large, W. G. (2015). The Benguela upwelling system: Quantifying the sensitivity to resolution and coastal wind representation in a global climate model. *Journal of Climate*, *28*(23), 9409-9432.

Smith, T. M., Reynolds, R. W., Peterson, T. C., & Lawrimore, J. (2008). Improvements to NOAA's historical merged land–ocean surface temperature analysis (1880–2006). *Journal of Climate*, *21*(10), 2283-2296.

Soares, P. M., Lima, D. C., Semedo, A., Cardoso, R. M., Cabos, W., & Sein, D. V. (2019). Assessing the climate change impact on the North African offshore surface wind and coastal low-level jet using coupled and uncoupled regional climate simulations. *Climate Dynamics*, *52*(11), 7111-7132.

Song, Y., Yu, Y., & Lin, P. (2014). The hiatus and accelerated warming decades in CMIP5 simulations. *Advances in Atmospheric Sciences*, *31*(6), 1316-1330.

Stanfield, R. E., Dong, X., Xi, B., Del Genio, A. D., Minnis, P., Doelling, D., & Loeb, N. (2015). Assessment of NASA GISS CMIP5 and post-CMIP5 simulated clouds and TOA radiation budgets using satellite observations. Part II: TOA radiation budget and CREs. *Journal of Climate*, *28*(5), 1842-1864.

Stewart, R. H. (2008). *Introduction to physical oceanography* (pp. 133-147). College Station: Texas A & M University.

Sverdrup, H. V., Johnson, M. W., & Fleming, R. H. (1942). The Oceans. Old Tappan, NJ: Prentice-Hall.

Sydeman, W. J., García-Reyes, M., Schoeman, D. S., Rykaczewski, R. R., Thompson, S. A., Black, B. A., & Bograd, S. J. (2014). Climate change and wind intensification in coastal upwelling ecosystems. *Science*, *345*(6192), 77-8

Sylla, A., Mignot, J., Capet, X., & Gaye, A. T. (2019). Weakening of the Senegalo–Mauritanian upwelling system under climate change. *Climate Dynamics*, 1-27.

Taylor, K. E., Stouffer, R. J., & Meehl, G. A. (2012). An overview of CMIP5 and the experiment design. *Bulletin of the American Meteorological Society*, *93*(4), 485-498.

Tokinaga, H., & Xie, S. P. (2011). Wave-and anemometer-based sea surface wind (WASWind) for climate change analysis. *Journal of Climate*, *24*(1), 267-285.

Tomczak, M., & Godfrey, J. S. (2013). *Regional oceanography: an introduction*. Elsevier.

Trenberth, K. E. (1997). The definition of el nino. *Bulletin of the American Meteorological Society*, *78*(12), 2771-2778.

Trenberth, K. E., Branstator, G. W., Karoly, D., Kumar, A., Lau, N. C., & Ropelewski, C. (1998). Progress during TOGA in understanding and modeling global teleconnections associated with tropical sea surface temperatures. *Journal of Geophysical Research: Oceans*, *103*(C7), 14291-14324.

Vallis, G. K. (2012). *Climate and the Oceans*. Princeton University Press.

Voldoire, A., Claudon, M., Caniaux, G., Giordani, H., & Roehrig, R. (2014). Are atmospheric biases responsible for the tropical Atlantic SST biases in the CNRM-CM5 coupled model?. *Climate dynamics*, *43*(11), 2963-2984.

Wang, C. (2002). Atlantic climate variability and its associated atmospheric circulation cells. *Journal of climate*, *15*(13), 1516-1536.

Wang, C., & Wang, X. (2013). Classifying El Niño Modoki I and II by different impacts on rainfall in southern China and typhoon tracks. *Journal of Climate*, *26*(4), 1322-1338.

Wang, C., Zhang, L., Lee, S. K., Wu, L., & Mechoso, C. R. (2014). A global perspective on CMIP5 climate model biases. *Nature Climate Change*, *4*(3), 201.

Wang, D., Gouhier, T. C., Menge, B. A., & Ganguly, A. R. (2015). Intensification and spatial homogenization of coastal upwelling under climate change. *Nature*, *518*(7539), 390.

Xiang, B., Zhao, M., Held, I. M., & Golaz, J. C. (2017). Predicting the severity of spurious "double ITCZ" problem in CMIP5 coupled models from AMIP simulations. *Geophysical Research Letters*, *44*(3), 1520-1527.

Xiu, P., Chai, F., Curchitser, E. N., & Castruccio, F. S. (2018). Future changes in coastal upwelling ecosystems with global warming: The case of the California Current System. *Scientific reports*, *8*(1), 2866.

Xu, K., Huang, R. X., Wang, W., Zhu, C., & Lu, R. (2017). Thermocline fluctuations in the equatorial Pacific related to the two types of El Niño events. *Journal of Climate*, *30*(17), 6611-6627.

Xu, Z., Chang, P., Richter, I., & Tang, G. (2014). Diagnosing southeast tropical Atlantic SST and ocean circulation biases in the CMIP5 ensemble. *Climate dynamics*, *43*(11), 3123-3145.

Xue, Y., Sellers, P. J., Kinter, J. L., & Shukla, J. (1991). A simplified biosphere model for global climate studies. *Journal of Climate*, *4*(3), 345-364.

Yang, H., & Wang, F. (2009). Revisiting the thermocline depth in the equatorial Pacific. *Journal of Climate*, *22*(13), 3856-3863.Yang, H., & Wang, F. (2009). Revisiting the thermocline depth in the equatorial Pacific. *Journal of Climate*, *22*(13), 3856-3863.

Zebiak, S. E. (1993). Air–sea interaction in the equatorial Atlantic region. *Journal of Climate*, *6*(8), 1567-1586.

Zelle, H., Appeldoorn, G., Burgers, G., & van Oldenborgh, G. J. (2004). The relationship between sea surface temperature and thermocline depth in the eastern equatorial Pacific. *Journal of physical oceanography*, *34*(3), 643-655.

Zheng, Y., Lin, J. L., & Shinoda, T. (2012). The equatorial Pacific cold tongue simulated by IPCC AR4 coupled GCMs: Upper ocean

heat budget and feedback analysis. *Journal of Geophysical Research: Oceans*, *117*(C5).

Zuidema, P., Chang, P., Medeiros, B., Kirtman, B. P., Mechoso, R., Schneider, E. K., ... & Brandt, P. (2016). Challenges and prospects for reducing coupled climate model SST biases in the eastern tropical Atlantic and Pacific oceans: The US CLIVAR Eastern Tropical Oceans Synthesis Working Group. *Bulletin of the American Meteorological Society*, *97*(12), 2305-2328.

List of acronyms

AGCM– Atmosphere General Circulation Model

CGCM – Coupled General Circulation Model

CMIP5–Climate Model Intercomparison Project

ENSO–El Niño-Southern Oscillation

EOF–Empirical Orthogonal Function

ERSSTv3– Extended Reconstructed Sea Surface Temperature

GPCP–Global Precipitation Climatology Project

HadSLP–Hadley Centre Sea Level Pressure dataset

IPCC–International Panel on Climate Change

ITCZ–Intertropical Convergence Zone

NWA–Northwest Africa

OGCM–Ocean General Circulation Model

PC–Principal Component

SODA–Simple Ocean Data Assimilation

TOA-Top Of the Atmosphere

UCLA control–University of California-Los Angeles Coupled General Circulation Model control run

UCLA COSZ– University of California-Los Angeles Coupled General Circulation Model sensitivity experiment run

WASWind–Wind and Anemometer-based Sea Surface Wind

z20–depth of the 20°C isotherm

Work leading to this thesis

AS FIRST AUTHOR

- **Castaño-Tierno, A.**, Mohino, E., Rodríguez-Fonseca, B., & Losada, T. (2018). Revisiting the CMIP5 Thermocline in the Equatorial Pacific and Atlantic Oceans. *Geophysical Research Letters*, *45*(23), 12-963.
- **Castaño-Tierno, A.**, Rodríguez-Fonseca, B., Losada, T. & Mohino, E. (2019). Large-scale CMIP5 bias influence on NWA upwelling representation. (To be submitted).
- **Castaño-Tierno, A.**, Losada, T., Rodríguez-Fonseca, B., & Mohino, E. (2019). Influence of vertical stratification and thermocline location on tropical atmosphere-ocean dynamics. (To be submitted).

OTHER WORK:

- Mechoso, C. R., Losada, T., Koseki, S., Mohino-Harris, E., Keenlyside, N., **Castaño-Tierno, A.**, ... & Toniazzo, T. (2016). Can reducing the incoming energy flux over the Southern Ocean in a CGCM improve its simulation of tropical climate?. *Geophysical Research Letters*, *43*(20), 11-057.
- Rodríguez-Fonseca, B., Suárez-Moreno, R., Ayarzagüena, B., López-Parages, J., Gó- mara, I., Villamayor, J., ... & **Castaño-Tierno, A.** (2016): A Review of ENSO Influence on the North Atlantic. A Non-Stationary Signal. *Atmosphere*, **7**, 87. http://www.mdpi.com/2073-4433/7/7/87/htm https://doi.org/10.1007/s00382-017-3941-1

FINANCIAL SUPPORT

This PhD has been made possible by sucessive contracts funded by the following national and international projects: MULCLIVAR (CGL2012-38923-C02-01-MINECO), PREFACE (EUFP7/2007-2013 Grant Agreement 603521), PRE^{4}CAST (CGL2017- 86415-R, Spanish Ministry of Science) and UPNAO (CGL2015-72164-EXP/AEI, Spanish Ministry of Science)..